

박 사 학 위 논 문  
Ph.D. Dissertation

시간-주파수 복합적인 펄스 재단을 이용한 저온  
알칼리 원자의 양자 제어

Quantum control of cold alkali atoms by using hybrid  
temporal-spectral pulse shaping

2017

이 한 결 (李 한 결 Lee, Han-gyeol)

한 국 과 학 기 술 원

Korea Advanced Institute of Science and Technology

박 사 학 위 논 문

시간-주파수 복합적인 펄스 재단을 이용한 저온  
알칼리 원자의 양자 제어

2017

이 한 결

한 국 과 학 기 술 원

물리학과

# 시간-주파수 복합적인 펄스 재단을 이용한 저온 알칼리 원자의 양자 제어

이 한 결

위 논문은 한국과학기술원 박사학위논문으로  
학위논문 심사위원회의 심사를 통과하였음

2016년 11월 29일

심사위원장 안 재 욱

심 사 위 원 심 홍 선

심 사 위 원 유 대 혁

심 사 위 원 이 상 민

심 사 위 원 이 진 형

# Quantum control of cold alkali atoms by using hybrid temporal-spectral pulse shaping

Han-gyeol Lee

Advisor: Jaewook Ahn

A dissertation submitted to the faculty of  
Korea Advanced Institute of Science and Technology in  
partial fulfillment of the requirements for the degree of  
Doctor of Philosophy in Physics

Daejeon, Korea  
November 29, 2016

Approved by

---

Jaewook Ahn  
Professor of Physics

The study was conducted in accordance with Code of Research Ethics<sup>1</sup>.

---

<sup>1</sup> Declaration of Ethical Conduct in Research: I, as a graduate student of Korea Advanced Institute of Science and Technology, hereby declare that I have not committed any act that may damage the credibility of my research. This includes, but is not limited to, falsification, thesis written by someone else, distortion of research findings, and plagiarism. I confirm that my thesis contains honest conclusions based on my own careful research under the guidance of my thesis advisor.

DPH  
20098082

이한결. 시간-주파수 복합적인 펄스 재단을 이용한 저온 알칼리 원자의 양자 제어. 물리학과 . 2017년. 75+v 쪽. 지도교수: 안재욱. (영문 논문)

Han-gyeol Lee. Quantum control of cold alkali atoms by using hybrid temporal-spectral pulse shaping. Department of Physics . 2017. 75+v pages. Advisor: Jaewook Ahn. (Text in English)

### 초 록

본 연구는 시간 및 주파수 공간 상에서 재단된 펄스 레이저 펄스, 즉 빛을 이용하여 이와 상호작용하는 원자의 양자 상태의 시간 변화를 원하는 방향으로 이끌어 가는데 대한 내용을 다루고 있다. 본 연구에서와 같이 빛과의 상호작용을 이용하여 양자 시스템의 상태 변화를 제어하는 방법을 양자 제어 ("quantum control" 혹은 "coherent control")라고 하며 그 상호작용의 세기에 따라 적용가능한 제어 원리에 다소 차이가 있다. 레이저 펄스의 세기가 약하여 원자와의 상호작용이 약한 경우 그 상호작용은 양자섭동이론으로 설명이 가능하며 레이저 펄스에 의한 양자 상태 사이의 전이 확률은 1% 이하이다. 이 경우 양자 제어의 기본적인 목표는 주어진 레이저 펄스를 재단하여 원하는 전이의 확률을 최대화하는 것이며 이를 위해서는 레이저 펄스를 이루는 주파수 요소들의 위상을 재단하여 각각의 주파수 요소에 대응되는 여러 전이 경로 사이의 간섭을 보강간섭이 되도록 만들어 주어야 한다. 이러한 양자 제어의 경우 일반적으로, 주어진 펄스와 같은 혹은 더 적은 에너지를 갖는 재단된 레이저 펄스로 수배 수십배의 전이 확률을 얻는 것이 가능하다. 본 연구에서는 이와 같은 양자 제어의 원리를 루비듐 다이아몬드 시스템에 적용하여 바닥 상태에서 가장 높은 들뜬 상태로의 전이를 최대화 시키는 방법을 찾고자 하였다. 가능한 전이 경로들을 그 위상에 따라 분류하면 총 8개의 블록으로 나눌 수 있다는 것을 확인하였으며 각각의 블록에 해당하는 레이저 펄스 스펙트럼에 적절한 위상을 가해줌으로써 전이 확률을 극대화 하는 실험을 수행하였다. 이러한 원리는 분자의 광결합/광해리와 같이 빛이 개입하는 상태변화 확률의 극대화나 분광학을 이용한 물질간의 구별 등에 적용될 수 있다.

레이저 펄스의 세기가 강한 경우 원자내의 2준위 양자 시스템에서 각 상태의 확률이 펄스의 세기에 따라 0과 1사이를 오가는 완전한 확률의 전이가 일어날 수 있으며 이를 일으키는 대표적인 현상이 라비 진동이다. 이때 수많은 원자로 이루어진 원자 구름에서 라비 진동이 일어나는 경우 레이저 펄스의 공간적인 분포가 일정하지 않기 때문에 구름 속 각 원자들의 라비 진동이 서로 다른 주기로 일어나게 된다. 따라서 구름 전체의 라비 진동은 주기가 다른 여러 사인파를 합쳐놓은 모양이 되며 라비 진동을 확인할 수 없게 된다. 이러한 공간적으로 진동이 평균화 되는 문제를 원자 구름과 레이저 빔을 가우시안 함수로 가정하고 원자 구름과 레이저 빔의 지름 사이 비를 변수  $n$ 으로 삼아 연구하였다. 수치 계산으로 얻은 구름 전체의 라비 진동 곡선의 형태는 변수  $n$ 과 일대일 대응됨을 확인하였으며 자기광포확장치에 잡힌 원자 구름을 가우시안 분포로 만들고 수행한 실험 결과 가우시안 함수를 사용한 모델이 실제 원자 구름에서 일어나는 공간 평균 효과를 잘 설명하고 있음을 확인할 수 있었다.

공간 평균 효과를 설명할 수 있는 가우시안 함수 모델을 사용하면 2준위 시스템에서 확률의 완전한 진동을 보이는 현상들을 실험적으로 분석할 수 있다. 이를 토대로 확률의 완전한 진동을 일으키는 또 다른 물리적인 현상인 주파수영역상 혹은 시간영역상에서 구멍이 뚫린 칩펄스에 대해 연구하였다. 칩(chirp)펄스란 펄스의 순간주파수가 시간에 따라 선형으로 변화하는 펄스를 말하며 순간주파수가 천천히 변화하는 칩펄스는 2준위 양자시스템을 바닥상태에서 천천히 끌어올려 들뜬상태로 완전히 전이시키는 단일 과정을 일으킨다. 칩펄스에 주파수영역상 혹은 시간영역상에서 구멍을 뚫음으로써 원래의 칩펄스가 일으키는 단일과정 중간에 개입하여 라비 진동을 일으킬 수 있으며 이러한 경우 라비 진동과 단일과정의 상호관계가 레이저 펄스의 세기에 의해 달라지게 되어 양자시스템에 펄스 세기에 따른 확률의 진동이 일어난다. 주파수영역상 구멍이 뚫린 칩펄스의 경우 2준위 시스템의 전체 시간변화는 블록 구(Bloch sphere)상의 세 회전인  $R_x(\Theta_1)R_z(\Theta_2)R_x(\Theta_1)$ 의 형태로 정리되었으며 시간영역상 구멍이 뚫린

칩펄스는  $R_z(\Theta_2)R_y(\Theta_1)R_z(\Theta_2)$ 의 형태로 정리되었다. 두 경우 모두 레이저 펄스의 세기에 따라  $\Theta_1$ 과  $\Theta_2$ 가 달라지게 되어 일어나는 확률의 진동을 실험적으로 확인할 수 있었다. 이러한 방법을 다준위 시스템에 적용할 경우 칩펄스에서 다준위 시스템의 각 전이에 대응되는 주파수공간상 혹은 시간공간상의 위치에 구멍을 뚫음으로써 다준위 시스템에서 일어나고 있는 단일 과정에 개입할 수 있다. 이러한 구멍들은 펄스의 세기변화에 따라 켜지고 꺼지는 스위치와 같은 역할을 할 수 있으며 따라서 전이 경로를 원하는 방향으로 이끌어가는 것이 가능하다.

**핵심 낱말** 펄스 재단, 양자 제어, 결맞음 제어

## **Abstract**

Quantum control of alkali atoms in ensemble is studied by using broadband pulse shaping schemes in both spectral and time domain. In the weak field regime, interference between two two-photon excitation passages of a four-level system of the rubidium atom in a diamond configuration was considered. Eight spectrum blocks were classified by inherent phase jumps of transition probability amplitude components and a condition for maximal constructive interference was predicted by second order time dependent perturbation theory. Experiments carried out with spectrally phase-coded laser pulses show good agreement with the theoretical prediction.

In the strong field regime, quantitative analysis on ensemble averaged Rabi oscillation was conducted to investigate spatial inhomogeneity of interaction. By using the ultrafast laser interaction with the cold atomic rubidium vapor spatially confined in a magneto-optical trap, the oscillatory behavior of the atom excitation is probed as a function of the laser pulse power. Theoretical model calculation predicts that the oscillation peaks of the ensemble averaged Rabi flopping fall on the simple Rabi oscillation curve of a single atom and the experimental result shows good agreement with the prediction. We also test the three-pulse composite interaction  $R_x(\pi/2)R_y(\pi)R_x(\pi/2)$  to develop a robust method to achieve a higher fidelity population inversion of the atom ensemble.

Based on quantitative analysis of inhomogeneity of interaction, dynamics of a two-level system induced by a chirped pulse with a spectral hole and a temporal hole were respectively explored in both theoretically and experimentally. When a spectral hole is made, the pulse is called a chirped zero-area pulse. By a chirped zero-area pulse, CPR and CPI of a two-level system takes place even there is no resonant spectrum. Theoretical investigation showed that the dynamics can be modeled by a three-step evolution,  $R_{-\varphi}(\Theta_2)R_z(\Theta_1)R_{\pi+\varphi}(\Theta_2)$ , where the first and the third are by Rabi oscillation and the second is an adiabatic evolution. The CPR and CPI dynamics is turned out to be a result of interplay between adiabatic evolution and Rabi rotations: CPI and CPR occur when adiabatic evolution makes two rabi rotations completely constructive or destructive. On the other hand, when a temporal hole is made on a chirped pulse, the system only begin with a superposition state shows probability oscillation, even to 0 or 1. The probability oscillation for this case is also by interplay between adiabatic evolution and Rabi rotation: the adiabatic evolution applies phase on a superposition state and the Rabi rotation mixes it. The probabilities of 0 or 1 occur when the interference is maximized. The studies on a chirped pulse with a temporal hole and a spectral hole showed that the hole can be a new control method of quantum control in strong field regime.

**Keywords** pulse shaping, quantum control, coherent control

# Contents

Contents . . . . .	i
List of Tables . . . . .	iv
List of Figures . . . . .	v
<b>Chapter 1. Introduction</b>	<b>1</b>
<b>Chapter 2. Review of quantum control</b>	<b>3</b>
2.1 Pulse shaping apparatus . . . . .	3
2.1.1 Apparatus utilizing spatially mapped spectral component: SLM . . . . .	3
2.1.2 Acousto-optic pulse shaper . . . . .	4
2.2 Quantum control in weak field regime . . . . .	5
2.3 Quantum control in strong field regime . . . . .	8
2.3.1 CPI and CPT in two-level system . . . . .	8
2.3.2 Spatially averaged interaction . . . . .	11
<b>Chapter 3. Theoretical backgrounds</b>	<b>13</b>
3.1 Electric field notation . . . . .	13
3.2 Femtosecond Rabi oscillation . . . . .	14
3.3 Multiphoton absorption in weak field regime . . . . .	16
3.4 Population inversion by linearly chirped electric field . . . . .	18
3.4.1 Interaction Hamiltonian of a linearly chirped pulse . . .	18
3.4.2 Adiabatic population inversion by a linearly chirped pulse	18
<b>Chapter 4. Magneto optical trap</b>	<b>21</b>
4.1 Vacuum chamber assembly . . . . .	21
4.2 Cooling and trapping . . . . .	21
4.3 MOT transitions of a $^{85}\text{Rb}$ atom . . . . .	22
4.4 Magnetic field characteristics . . . . .	23
4.5 Process for High-vacuum . . . . .	23
4.6 Diode laser system . . . . .	25
4.7 Characterization of the MOT . . . . .	25
<b>Chapter 5. Interference control of a four level diamond system</b>	<b>30</b>
5.1 Theoretical consideration of interference control . . . . .	30

5.2	Four level approximation of hyperfine states . . . . .	32
5.3	Experimental details . . . . .	33
5.3.1	SLM calibration . . . . .	35
5.4	Experimental result . . . . .	35
5.4.1	$A+C$ phase rotation . . . . .	35
5.4.2	$B+C$ phase rotation . . . . .	36
5.4.3	$AC+BD$ phase rotation . . . . .	36
<b>Chapter 6.</b>	<b>Spatially averaged Rabi oscillation</b>	<b>39</b>
6.1	Spatial averaging effect . . . . .	39
6.2	Experimental details . . . . .	41
6.3	Experimental result . . . . .	41
6.3.1	Spatially averaged oscillation . . . . .	41
6.3.2	$R_x(\Theta_o/2)R_y(\Theta_o)R_x(\Theta_o/2)$ composite-pulse operation . . . .	44
<b>Chapter 7.</b>	<b>Quantum dynamics of a two-state system induced by a chirped zero-area pulse</b>	<b>46</b>
7.1	Theoretical consideration . . . . .	46
7.1.1	A chirped zero-area pulse . . . . .	46
7.1.2	Schrödinger equation described in the interaction picture of the main pulse . . . . .	47
7.1.3	Dynamics described in the adiabatic basis of the main pulse . . . . .	48
7.1.4	Ramsey-type three pulsed interactions . . . . .	49
7.2	Calculation results . . . . .	52
7.3	Experimental setup . . . . .	54
7.4	Experimental Results and discussion . . . . .	56
<b>Chapter 8.</b>	<b>Dynamics of a two-state system induced by a temporal hole on a chirped pulse</b>	<b>59</b>
8.1	Theoretical model . . . . .	59
8.2	Experimental Setup . . . . .	65
8.3	Results and Discussion . . . . .	65
<b>Chapter 9.</b>	<b>Conclusion</b>	<b>68</b>
	<b>Bibliography</b>	<b>69</b>
	<b>Acknowledgments in Korean</b>	<b>73</b>





## List of Tables

5.1	Phase function solution of the four-level diamond-configuration system . . . . .	36
-----	--	----

## List of Figures

2.1	Schematic of the 4f system setup. 4f system formed by a pair of gratings and a pair of cylindrical mirrors makes frequency components of the pulse spatially mapped Fourier plane. Gray dashed line indicates Fourier plane. . . . .	4
2.2	Schematic and working principle of the AOPDF. The incident optical pulse polarized along ordinary axis is diffracted by acousto-optic interaction when the phase-matching condition is satisfied. Diffracted shaped output pulse is polarized along extraordinary axis. Figure from [12] ( <a href="https://doi.org/10.1364/OL.25.000575">https://doi.org/10.1364/OL.25.000575</a> ). . . . .	5
2.3	Quantum interference control in a three level ladder system via phase window. (a) Description of $\pi/2$ phase window. The window was scanned through spectral range of the laser pulse. (b) Experimental result. Fluorescence from 5D state population was measured as a function of the phase window position. About 600% of enhancement was obtained at maximum. (c) Comparison of temporal electric field between transform limited case (dotted line) and optimal pulse (solid line). Figure from [6] ( <a href="https://doi.org/10.1103/PhysRevLett.86.47">https://doi.org/10.1103/PhysRevLett.86.47</a> ). . . . .	6
2.4	Quantum interference control in a three level ladder system via spectral blocking. (a) Description of variable slit located at the Fourier plane of pulse shaping apparatus. Blocked spectral region was varied by adjusting slit width. (b) Experimental result. Fluorescence from 5D state population was measured as a function of the cutoff frequency. About 100% of enhancement was obtained at maximum. (c) Comparison of temporal electric field between transform limited case (dotted line) and optimal pulse (solid line). Peak electric field of the pulse was reduced by a factor of 38. Figure from [6] ( <a href="https://doi.org/10.1103/PhysRevLett.86.47">https://doi.org/10.1103/PhysRevLett.86.47</a> ). . . . .	7
2.5	Quantum interference control of inter-excited state two-photon transition in a three level V-type system via phase window. (a) Measured inter-excited state transition probability as a function of phase applied on the phase window. Phase of the windowed region (shown in inset) was varied from 0 to $2\pi$ . (b-d) Phasor diagram corresponds to each marked point of (a). Maximal transition probability occurred when all transition probability amplitude terms, A, B and C, are inphase, as shown in (c). Figure from [13]. . . . .	8
2.6	(a) Comparison between experimental results of Rabi oscillation (black circle) and rapid adiabatic passge (red square) of single quantum dot. RAP shows robustness of CPI after threshold pulse area $\Theta > \pi$ . (b) Calculation result of transition probability of a quantum dot as functions of pulse area $\Theta$ and linear frequency chirp. (c) Experimental result of transition probability as a function of chirp with fixed pulse area $\Theta = 2\pi$ . CPI is shown when $ \phi''  > 30 \text{ ps}^2$ . Figure from [29] ( <a href="https://doi.org/10.1103/PhysRevLett.106.166801">https://doi.org/10.1103/PhysRevLett.106.166801</a> ). . . . .	9

2.7	Comparison between the excitation dynamics by a single pulse (left) and 7 pulse train (right). For (a) and (b), blue solid line and dots are calculation and experimental results of Rabi oscillation, respectively. Red dashed line and dots are calculation and experimental results of adiabatic process, respectively. The adiabatic process in (a) is RAP by a single chirped pulse and in (b) is PAP (piecewise adiabatic passage) by piecewisely chirped 7 pulse train. Figure from [31] ( <a href="https://doi.org/10.1103/PhysRevLett.100.103004">https://doi.org/10.1103/PhysRevLett.100.103004</a> ) . . . . .	11
2.8	Diagram of a setup designed to reduce spatial averaging by limiting detection region. Excited state populations from only small central volume of interaction can be ionized and detected by a tightly focussed probe beam. Figure from [31] ( <a href="https://doi.org/10.1103/PhysRevLett.100.103004">https://doi.org/10.1103/PhysRevLett.100.103004</a> ) . . . . .	12
3.1	Time evolution of eigenstate represented by time dependent change of eigenenergy. A $50000\text{fs}^2$ linearly chirped pulse with spectral FWHM of $\sim 7\text{nm}$ and pulse area $2\pi$ was used for calculation. Blue line represents $\lambda_+(t)$ , red line represents $\lambda_-(t)$ , and dotted cyan line is temporal width $\tau$ of the pulse. Starting from initial state $ g\rangle$ , an adiabatic time evolution occurs through red line, $\lambda_-(t)$ , and the corresponding state evolution is $ g\rangle \rightarrow  e\rangle$ . . . . .	20
3.2	State representation of time evolution given in 3.1. Blue line represents $ \psi_+(t)\rangle$ , red line represents $ \psi_-(t)\rangle$ , and dotted cyan line shows temporal width $\tau$ of the pulse. From an initial state $ g\rangle$ , time evolution of the state is described by the red line, $ \psi_-(t)\rangle$ , which shows the complete population inversion of atomic states. . . . .	20
4.1	Schematic diagram of the chamber assembly. . . . .	22
4.2	Doppler cooling inside a MOT. If an atom is moving toward the laser beam, light seen by the atom is blue shifted. Also, if an atom is moving along with the laser beam, the light is red shifted for the atom. Thus, if the beam is red detuned initially, the atoms moving toward the laser beam feels the light with smaller detuning, which results higher transition probability of the atoms moving toward the beam. Since absorbed photons transfer momentum $\hbar\vec{k}$ to the atom, deceleration occurs when atom and photon moving in opposite direction have higher probability of absorption. . . . .	22
4.3	Trapping process inside a MOT. To make position dependence of the transition probability, circularly polarized beams and magnetic field are used. Since magnetic field linearly depends on position, Zeeman energy shift induced by the magnetic field is also linear to the position. The $\sigma^\pm$ circularly polarized beams only induces $\Delta m = \pm 1$ transition due to the angular momentum conservation. Therefore, as shown in the diagram, transitions giving momentum kicks toward the point of zero magnetic field become more probable, which gather atoms to near zero magnetic field region. . . . .	23
4.4	Energy level diagram and MOT transitions. . . . .	24
4.5	SAS signal corresponds to the hyperfine transition of $F=3 \rightarrow F'$ of $^{85}\text{Rb}$ atoms. The position indicated by an arrow indicates lock point for MOT cooling and trapping beam, which is 12 MHz ( $\simeq$ natural linewidth) red detuned from $F=3 \rightarrow F'=4$ transition. . . . .	25

4.6	SAS signal corresponds to the hyperfine transition of $F=2 \rightarrow F'$ of $^{85}\text{Rb}$ atoms. The position indicated by an arrow indicates lock point for MOT repump beam which corresponds to $F=2 \rightarrow F'=2$ transition peak. Easily resolvable $F=2 \rightarrow F'=2$ transition was used for repump instead of $F=2 \rightarrow F'=3$ transition, which gives no difference for cooling and trapping when repump laser power is enough. . . . .	26
4.7	Radial magnetic field produced by the anti-Helmholtz coil, theoretical calculation(blue) and measured data(red dots) at 1A of current. Data shows the linearity of the magnetic field at the center of the chamber. . . . .	27
4.8	Axial magnetic field produced by the anti-Helmholtz coil, theoretical calculation(blue) and measured data(red dots) at 1A of current. Data shows the linearity of the magnetic field at the center of the chamber. . . . .	28
4.9	Schematic diagram of a grating feedback diode laser. . . . .	28
4.10	Loading curve(red) of the MOT. The ground line(blue) was recorded when all lasers were blocked. Estimated loading time from fitted equation is 2.35(s). . . . .	29
5.1	(a) Rubidium energy level configuration [44]. Four states, $5S_{1/2}$ , $5P_{1/2}$ , $5P_{3/2}$ , and $5D_{3/2}$ , form a diamond system, while the two-photon transition to $5D_{5/2}$ (gray) via $5P_{3/2}$ forms a ladder system. (b) The spectrum blocks and the schematic shape of $f(\omega)$ , the integrand of $c_{fg}^{nr}$ . (c) Schematic experimental setup. . . . .	31
5.2	Phase-step scanning experiment: (a) Laser spectrum after the SLM (solid line) and phase-step function (dashed line), where the spectral tails were cut for better spectral resolution. (b) The fluorescence signal (solid line) obtained by sweeping the spectral $\pi$ -phase step, overlapped with the numerical calculation (dashed line). Each peak is labeled with the corresponding resonant frequency. . . . .	34
5.3	(a) Vector diagram for the resonant ( $C''$ ) and non-resonant ( $A + C$ , $B + D$ ) transitions. (b) $A + C$ phase rotation. (c) $B + C$ phase rotation. (d) Experimental result for (b), where the phases $\phi_A$ and $\phi_C$ are independently varied from $-\pi/2$ to $2\pi$ . (e) Experimental result for (c), where $\phi_B$ and $\phi_C$ are independently varied from $-\pi/2$ to $2\pi$ . . . . .	37
5.4	Interference control of all non-resonant components with respect to the resonant component. The phases of $A$ and $C$ vary from 0 to $2\pi$ while the phases of $B$ and $D$ vary simultaneously from 0 to $-2\pi$ . The vector diagrams in the bottom right corner show the orientation of each transition probability amplitude component corresponding to the numbered points in the main plot. . . . .	38
6.1	(a) Ensemble-atom Rabi oscillation in Eq. (6.3) for various size ratios $w_o/w_a = \sqrt{n}$ for $n = 0.1, 0.2, \dots, 0.9$ and $1, 2, \dots, 10$ (from the bottom to the top). Dotted line represents the single-atom Rabi oscillation in Eq. (6.1). (b,c) Atom probability distributions, at the marked points from the EARO curve for $w_o/w_a = \sqrt{6}$ in (a), plotted as a function of (b) $\Theta(r, z; \Theta_o)$ , the pulse area, and (c) $\theta$ , the polar angle of Bloch vector. . . . .	40

6.2	(a) Schematic diagram of the experimental setup. Ultrafast laser pulses were split into two pulses, one for Rabi oscillation and the other frequency-doubled for atom ionization. Both pulses were independently focused and delivered to the MOT by a dichroic mirror (DM). (b) Schematic diagram of the $^{85}\text{Rb}$ MOT chamber. The trapping and re-pumping laser beams were adjusted to vary the atom cloud size from 250 to 500 $\mu\text{m}$ [51]. (c) Energy level diagram of the Rb atom and the laser spectrum. Atoms in the excited $5P_{1/2}$ state were photo-ionized and $\text{Rb}^+$ ions were transferred by bias electric plates and measured by a micro-channel plate detector (MCP). . . . .	42
6.3	Experimental result of ensemble-atom Rabi oscillations: (a) Laser beam width ( $w_o$ ) was 2.5 times of the atom cloud size ( $w_a$ ) or $w_o = 2.5w_a$ , (b) $w_o = 1.7w_a$ , and (c) $w_o = w_a$ . The highlighted line in each figure illustrates the calculation for the closest integer $(w_o/w_a)^2$ that corresponds to (a) $(w_o/w_a)^2 = 6$ , (b) 3, and (c) 1, respectively. . . . .	43
6.4	Composite-pulse experiment of ensemble-atom Rabi oscillation. For an atom ensemble of the size 1.7 times smaller than a laser beam ( <i>i.e.</i> , $w_o = 1.7w_a$ ), the excited-state population for the composite-pulse operation $R_x(\Theta_o/2)R_y(\Theta_o)R_x(\Theta_o/2)$ was measured and plotted in black circles. In comparison, the single pulse experiment $R_x(\Theta_o)$ was plotted in red boxes. The solid lines represent the corresponding numerical calculations, when the spatial inhomogeneity of the ensemble-atom experiment is taken into account. The dotted lines are for the spatially homogeneous case ( <i>i.e.</i> , $w_o \gg w_a$ ), when the theoretical formulas are given by $1 - \cos^4(\Theta_o/2)$ (black) for the composite pulse and $\sin^2(\Theta_o/2)$ (red) for single pulses, respectively. . . . .	44
7.1	(a) The Rabi frequencies $\Omega_1(t)$ (dotted line) for the main pulse, $ \Omega_2(t) $ (dashed line) for the hole, and $ \Omega(t) $ (solid line) for the total electric field. (b) The time evolution of the transition probabilities in bare atom and adiabatic bases. (c) The transience of the polar angle $\theta_{\text{rot}}(t)$ (solid line) for the rotational axis of the Bloch vector in the adiabatic basis compared with $ \Delta_F(t) $ (dotted line) and $ \Omega_F(t) $ (dashed line). The calculation parameters chosen at a CPR are given in the text. . . . .	51
7.2	(a) Numerical calculation of the transition probability in the atomic basis is plotted as a function of $\Theta_{\text{Rabi}}$ , the unshaped-pulse Rabi phase, and $c_2$ , the frequency chirp. Localized CPR regions appear as spots around $\textcircled{A}$ , $\textcircled{B}$ , $\dots$ , $\textcircled{E}$ ; and CPI regions as strips, e.g., along $\textcircled{1}$ - $\textcircled{6}$ . The dotted lines indicate contours for the estimated rotation angles $\Theta_1$ and $\Theta_2$ defined by Eqs. (7.32) and (7.34). (b) and (c) Trajectories of CPR and CPI represented in the adiabatic basis for chosen points in (a), respectively. . . . .	53
7.3	Schematics of the experimental setup. Femto-second laser pulses were shaped by an acousto-optic programmable dispersive filter (AOPDF) and a 4f-geometry zero-dispersion stretcher; and as-produced chirped zero-area pulses interacted with cold rubidium atoms ( $^{85}\text{Rb}$ ) in a magneto-optical trap. After 3 ns, frequency-doubled laser pulses ionized the excited atoms. . . . .	55

7.4	(a) Experimental result and (b) numerical simulation of the chirped zero-area pulse excitation of a cold rubidium atom ensemble. The transition probabilities were plotted as a function of $c_2$ (linear chirp) and $\Theta_{\text{Rabi}}^{\text{max}}$ . Interaction inhomogeneity due to the Gaussian spatial profile of the atom ensemble was taken into account for the calculation of (b). (c) Experimental result of spectral hole-width scan. Measured pulse energies for the first CPI (e.g., the stars marked in (a) and (b)) are plotted for various spectral hole widths (red squares), in comparison with the calculation result (black dots). . . . .	57
8.1	a-c) Time dependences of Normalized electric field envelope and mixing angle $2\vartheta$ are plotted for a) a chirped pulse, b) a chirped pulse with a temporal hole of width $\tau_h = 0.1\tau$ and depth $k = 0.9$ , c) a chirped pulse with a temporal hole of width $\tau_h = 0.1\tau$ and depth $k = 1$ . d-f) Evolution on Bloch sphere in adiabatic basis corresponding to a), b) and c) are respectively plotted and the arrows indicates direction of evolution. x-axis is azimuthal angle on the Bloch sphere and y-axis is polar angle on the Bloch sphere. For b), c), e) and f), red line indicated $-\tau_h < t < \tau_h$ region, and For c) and f), black line indicates changes at $t = 0$ . . . . .	62
8.2	a) Schematics of the experimental setup and level diagram of $^{85}\text{Rb}$ atom. Our two-level system consists of $5S_{\frac{1}{2}}$ , $5P_{\frac{1}{2}}$ states of $^{85}\text{Rb}$ . To measure $ \psi_{-}\rangle$ probability after the interaction, applied ionization pulse ionize $5P_{\frac{1}{2}}$ state atoms only and $\text{Rb}^{+}$ ions counted via microchannel plate(MCP). b) Electric field envelope used for experiment, which is calculated from measured intensity profile. Due to the limited spectral resolution of pulse shaping, the temporal hole removed about 60% of electric field at $t = 0$ . Inset shows measured intensity profile via cross-correlation. The assymetry of the pulse comes from spectral assymetry, however, gives no significant effect on dynamics. . . . .	64
8.3	a) Starts from a initial state of $( \psi_{-}\rangle +  \psi_{+}\rangle e^{i\varphi})/\sqrt{2}$ , calculated probability of $ \psi_{-}\rangle$ state after interacting with a chirped pulse with a hole is plotted as a function of calibrated peak pulse area and initial state relative phase $\varphi$ . Spatial inhomogeneity of the interaction is also included in calculation. b) Measured probability of $ \psi_{-}\rangle$ (or $ 1\rangle$ ) state after interacting with a chirped pulse with a hole is plotted as a function of calibrated peak pulse area and initial state relative phase $\varphi$ . c) Calculation and experimental results along three dashed lines in a) and b) are simultaneously plotted. . . . .	67

# Chapter 1. Introduction

The term “quantum control”, controlling an interaction between light and a quantum system and steering the evolution of the system toward an aimed direction, have been a desire of my whole research. From the very beginning of quantum mechanics, light has been a powerful tool and provided many important clues for exploring quantum nature. In early studies of light-matter interaction, measurement and observation of phenomena were crucial, and hence, excitation and evolution of a system were separately treated. However, as our understanding becomes deeper, a brilliant idea, photo-assisted manipulation of chemical reaction appeared. This idea, which utilized excitation by light to manipulate evolution of a system, was the beginning of quantum control [1].

The first subject of quantum control was selective photo-assisted dissociation of molecules. Suggested scheme used two colors of narrow band laser pulses or continuous wave lasers to induce excitation from two different vibrational state. It was shown that dissociation yield can be changed by adjusting relative phase between two laser light, which alters interference between two vibrational states [2]. However, this scheme turned out to be imperfect since molecular vibrational dynamics can be occurred in sub-pico second regime. In these circumstances, adopting femtosecond laser was a matter of course to maintain coherence all along the interaction. Introducing femtosecond laser brought great advantages to quantum control schemes. Decoherence of a quantum system is prevented during interaction, and moreover, wide bandwidth of several THz can cover multiple transitions of the system in the same time. Advances of pulse shaping techniques realized manipulation of phase and amplitude of the broadband spectrum [3, 4] and interference among multiple transition passages was controlled by shaped femtosecond pulses. These control schemes are usually studied in perturbative regime and focussed on enhancement of a target multiphoton transition probability [5, 6]. By using such control schemes, different substances can be clearly distinguished. Due to the difference on energy level structure, an optimal pulse for a specific substance is not optimal or worse for others, which gives better contrast of transition probability than unshaped pulse case. In that regard, spectroscopic and microscopic application to distinguish materials was suggested and successfully demonstrated in [7, 8].

After studies on the quantum computation using states of atoms, ions and artificial atoms as qubits emerged, control in strong field regime became an important issue. In this regime, complete probability inversion (CPI) and complete probability return (CPR) can occur. Although most of phenomena inducing CPI and CPR, such as Rabi oscillation, composite pulse excitation and adiabatic passage techniques [9], have been studied for several decades, improved schemes for fast, precise and specialized manipulation of qubit states still have great possibility [10].

In this dissertation, we study control of quantum state evolution of alkali atoms in ensemble by using the laser pulses shaped in both frequency and time domain. Previous related works, from interference control in weak field regime to CPI dynamics in high field regime, will be reviewed in chapter 2. In chapter 3, we consider theoretical foundations of atom-pulse interaction. In weak field regime, interaction between a femtosecond pulse and an atom can be treated with time dependent perturbation theory. Transition of lowest possible order becomes dominant and analytic discussion is possible. When the lowest possible order transition involves multiple photons, interference among transition probability amplitude components sensitively react to spectral phase of the pulse. Thus, by shaping spectral phase of the pulse via pulse shaper, we can control the transition probability in such case. However, if pulse



energy is large enough, approximation using first few terms of perturbation series is no longer valid. CPI dynamic such as Rabi oscillation or adiabatic passage technique can be obtained from full solution of time dependent Schrödinger equation. For experimental observation of CPI and CPR dynamics, a cold, dense and spatially confined atomic ensemble trapped in magneto optical trap (MOT) was used. In chapter 4, properties of our MOT is discussed.

My studies of quantum control starts from dynamics in weak field regime, which can be simply treated by perturbation theory. In chapter 5, manipulation of two-photon transition probability by controlling interference between two two-photon excitation passages is experimentally demonstrated in diamond shaped energy level configuration of a rubidium atom. In addition, reduction of hyperfine states into fine structure states is also discussed.

Since both laser beam and an atomic ensemble have spatial distribution, spatially averaged CPI and CPR dynamics of an ensemble is quite different from single particle case. For quantitative analysis of this problem, model calculation and experimental results of spatially averaged Rabi oscillation is considered in chapter 6. Also, enhancement of robustness on ensemble averaged oscillation via a designed train of pulses is demonstrated. In chapter 7, CPI and CPR dynamic by a new type of pulse, chirped zero-area pulse, is considered. A zero-area pulse, a resonant pulse with zero temporal pulse area, induces CPR, or no excitation. In our study, a zero-area pulse was produced by making a resonant spectral hole at a resonant pulse. Even though it has no resonant frequency component, numerical calculation result showed that a chirped zero-area pulse can induce both CPI and CPR. Theoretical analysis conducted in adiabatic basis showed that CPI and CPR dynamic caused by interplay between adiabatic evolution and Rabi oscillation, which can be used as a new quantum control scheme. From the dynamics induced by chirped zero-area pulse, great possibilities of quantum control under adiabatic basis is revealed. In adiabatic basis, the base vector itself is time varying and its time-dependent change gives nonadiabatic coupling between two adiabatic states. And by making a temporal hole at the moment of zero instantaneous detuning, rapid change of the base vector, which leads Rabi rotation of the system, can be achieved. In chapter 8, nonadiabatic coupling introduced by a temporal hole on a chirped pulse and probability oscillation of a two-state by it are considered.

## Chapter 2. Review of quantum control

The term “quantum control” or “coherent control” refers certain schemes which aim to control a quantum evolution to a desired direction, mainly using programmed broadband laser pulses. Generally, as well as the fundamental parameters of the pulse such as electric field amplitude and central frequency of the pulse, phase and amplitude of each spectral component of broadband pulses also can be shaped to manipulate transitions. Note that defined by Fourier transform relation, any arbitrary pulse shape in time domain can be made by manipulation of phase and amplitude in spectral domain. And for such shaping in spectral domain, pulse shaping apparatus such as spatial light modulators and acousto optic devices are used. In this chapter, we briefly review several previous works of quantum control. We shall start from the review of pulse shaping schemes for experimental realization of quantum control. Then, we first see the control schemes of multi photon transition in weak field regime, which can be described by the lowest order term of time-dependent perturbation theory, or Dyson series expansion. And finally, the dynamics which involving complete solution of time dependent Schrödinger equation, such as Rabi oscillation and adiabatic probability transfer, will be considered.

### 2.1 Pulse shaping apparatus

For the sort of experiments utilizes CW laser or RF pulses, the modulation in  $\mu\text{s}$  to ns regime is required to control the electric field in time-domain. The modulation using AOM (acousto-optic modulator) or EOM (Electro-optic modulator) can cover such temporal regime and gives satisfactory results. However, for our broadband pulse with temporal width of sub-ps regime, temporal modulation in fs regime is required to control the temporal profile. No electronics can catch up such fast event. Thus, rather than direct shaping of the pulse in time-domain, pulse shaping in spectral domain was considered and realized. Nowadays, two typical pulse shaping schemes are widely used, one is a scheme using 4f geometry formed by a pair of gratings and a pair of cylindrical mirror, and the other utilizes acousto-optic device. Details of both schemes will be discussed below.

#### 2.1.1 Apparatus utilizing spatially mapped spectral component: SLM

To acquire access for each spectral component and apply manipulation on each, we first need to separate spectral components of a pulse. Typically, a 4f system formed by a pair of gratings and a pair of cylindrical mirrors is used for spatial separation of the spectral components. When a broadband pulse is diffracted by a grating, each spectral component of the pulse is divided by grating equation  $d \sin \theta = n\lambda$ , where  $d$  is groove size of the grating. A cylindrical mirror with focal length  $f$  is placed after  $f$  from the grating to collimate bundle of radiations of diffracted frequency components. And each frequency component is focussed on a plane after  $f$  from the cylindrical mirror. Thus, the pulse at the plane after  $f$  from the cylindrical mirror is on a frequency domain, where the spectrum is spatially mapped. Note that at Fourier plane, the frequency components of the pulse can be assumed as a bundle of CW radiations with narrow spectral width. So, by placing appropriate mask on a Fourier plane, we can manipulate each spectral component of the pulse. After the manipulation, the spectral components combined by the other cylindrical mirror and grating, which are separated by  $f$  in propagation direction. Fig. 2.1 shows

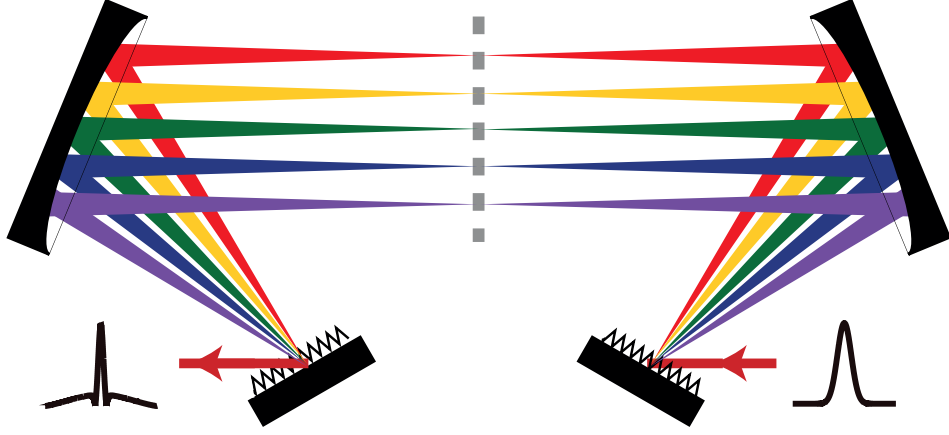


Figure 2.1: Schematic of the 4f system setup. 4f system formed by a pair of gratings and a pair of cylindrical mirrors makes frequency components of the pulse spatially mapped Fourier plane. Gray dashed line indicates Fourier plane.

a schematic of the 4f system setup, where the gray dashed line indicates Fourier plane of the 4f system.

For convenient and effective pulse shaping, the mask placed at Fourier plane can be replaced by an active device, which is called SLM (spatial light modulator). A typical SLM consists of three layers, an array of liquid crystals lies in the middle and two layers of glass coated by conductive film covers the liquid crystal array. The liquid crystal is formed by long, rod-like molecules. When electric field is applied to a liquid crystal, it rotates to be aligned with electric field and the refractive index for a certain polarization direction is changed. Thus, by individually adjusting applied voltage on each liquid crystal, it can be used as an active phase mask. Furthermore, To achieve simultaneous shaping of both amplitude and phase, one needs two SLMs and a pair of polarizer[4]. The response time of a SLM is typically order of 10 ms, the time requires for reorientation of the liquid crystals.

### 2.1.2 Acousto-optic pulse shaper

An acousto-optic programmable dispersive filter (AOPDF) is a pulse shaping device, which utilizes a quasi collinear acousto-optic interaction[11, 12]. Consider optical radiation of frequency  $\omega$  with a polarization aligned in fast ordinary axis traveling inside of an acousto-optic medium. When acoustic wave of frequency  $\Omega$  meet the optical radiation inside an acousto-optic medium and phase-matching condition is satisfied, the optical radiation is diffracted to slow extraordinary axis by acousto-optic interaction. We can define a parameter  $\alpha$  from phase matching condition, given by

$$\alpha = \Delta n \frac{V}{c} \quad (2.1)$$

where  $V$  is the speed of sound inside medium and  $c$  is the speed of light, and  $\Delta n$  is the refractive index difference between ordinary and extraordinary axis. Using the parameter  $\alpha$ , the optical frequency  $\omega$  and the acoustic frequency  $\Omega$  satisfying phase-matching condition have the relation

$$\Omega = \alpha \omega. \quad (2.2)$$

Therefore, each frequency component of a broadband pulse has its coupled acoustic frequency defined by  $\alpha$ . And the pulse diffracted into slow extraordinary axis can be expressed by

$$\tilde{E}_{\text{out}}(\omega) \propto \tilde{E}_{\text{in}}(\omega) \tilde{S}(\alpha \omega), \quad (2.3)$$

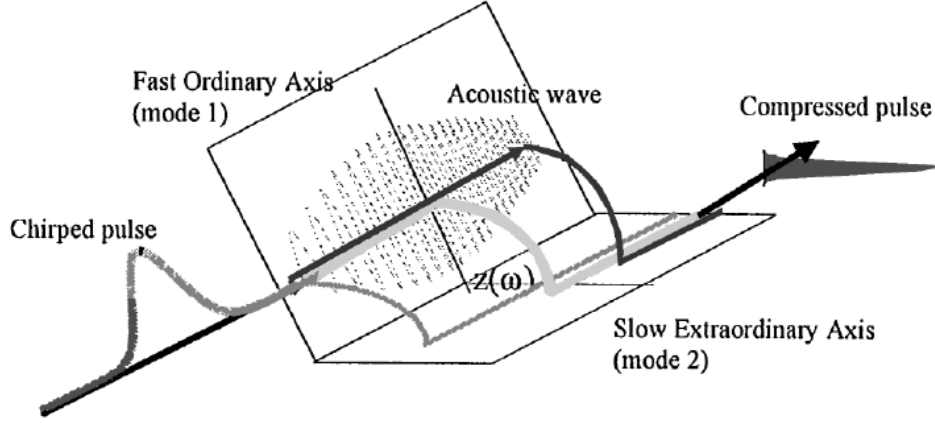


Figure 2.2: Schematic and working principle of the AOPDF. The incident optical pulse polarized along ordinary axis is diffracted by acousto-optic interaction when the phase-matching condition is satisfied. Diffracted shaped output pulse is polarized along extraordinary axis. Figure from [12] (<https://doi.org/10.1364/OL.25.000575>).

where  $\tilde{S}(\alpha\omega)$  is the spectral electric field of the acoustic wave. Also, Eq. (2.3) can be rewritten as

$$E_{\text{out}}(t) \propto E_{\text{in}}(t) * S(t/\alpha), \quad (2.4)$$

where  $*$  is a convolution symbol. So, for an acousto-optic device calibrated with respect to  $\alpha$ ,  $\tilde{S}(\alpha)(\omega)$  or  $S(t/\alpha)$  can be calculated by using the information about initial pulse shape and desired pulse shape. Since AOPDF utilizes acoustic wave for pulse shaping, it is especially outstanding for pulse shaping into smooth and continuous shape, for instance, chirping. The acousto-optic crystal used in our AOPDF (Dazzler, Fastlite) is  $\text{TeO}_2$  with  $d = 2.5$  cm.

## 2.2 Quantum control in weak field regime

In weak field regime, transition probability amplitude of one-photon transition in a two level system with resonant frequency  $\omega_0$  can be described by the equation

$$c^{(1)} = \frac{\mu}{\hbar} E(\omega_0), \quad (2.5)$$

where  $E(\omega_0)$  is spectral electric field amplitude of  $\omega_0$ ,  $\mu$  is a transition dipole moment between two states. As shown in Eq. (2.5), one-photon transition in weak field regime has no possibility of control other than electric field. Thus, quantum control in weak field regime is focused on multiphoton transitions.

Now, let's consider the simplest case of multiphoton transition, two-photon transition in a ladder system. The transition probability amplitude from a ground state  $|g\rangle$  to a final state  $|f\rangle$  via an intermediate state  $|i\rangle$  is given by a equation in spectral domain as

$$c_f^{(2)} = -\pi \frac{\mu_{fi}\mu_{ig}}{\hbar^2} E(\omega_{fi})E(\omega_{ig}) + i \frac{\mu_{fi}\mu_{ig}}{\hbar^2} \wp \int_{-\infty}^{\infty} \frac{E(\omega)E(\omega_{fg} - \omega)}{\omega_{ig} - \omega} d\omega, \quad (2.6)$$

where  $E(\omega)$  is the spectral electric field component of  $\omega$ ,  $\omega_{nm}$  is a resonant frequency of the transition between two states  $|n\rangle$  and  $|m\rangle$ ,  $\mu_{nm}$  is a transition dipole moment between two states  $|n\rangle$  and  $|m\rangle$  and  $\wp$  denotes the Cauchy principle value calculation. Note that Eq. (2.6) comes from the Fourier transform of the second order term of dyson series. The first term in Eq. (2.6), which describes a two-photon transition

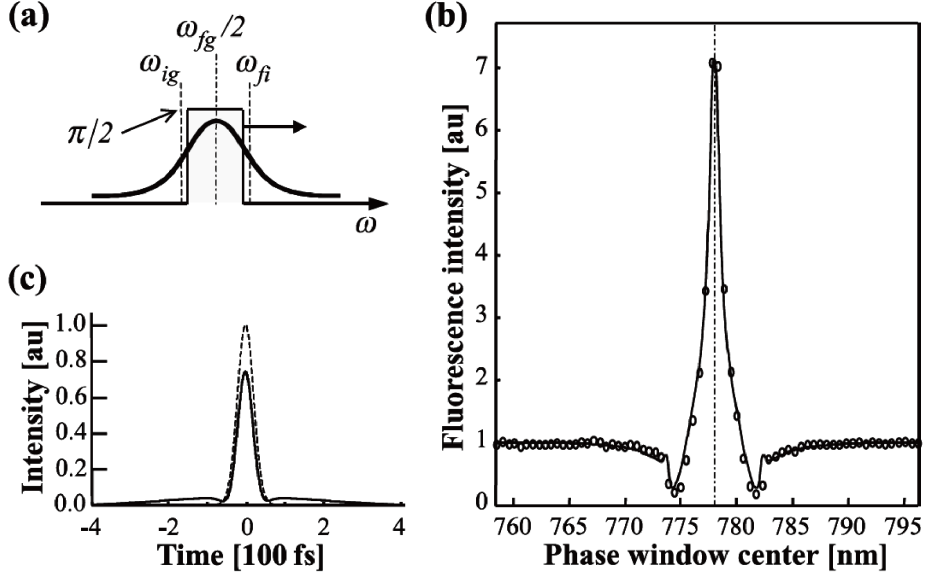


Figure 2.3: Quantum interference control in a three level ladder system via phase window. (a) Description of  $\pi/2$  phase window. The window was scanned through spectral range of the laser pulse. (b) Experimental result. Fluorescence from 5D state population was measured as a function of the phase window position. About 600% of enhancement was obtained at maximum. (c) Comparison of temporal electric field between transform limited case (dotted line) and optimal pulse (solid line). Figure from [6] (<https://doi.org/10.1103/PhysRevLett.86.47>).

by two on-resonant frequency components, is usually called a 'resonant term'. Similarly, the second term in Eq. (2.6), which describes a sum of all possible frequency pairs obeying energy conservation, *i.e.*,  $\omega_{fg} = \omega_1 + \omega_2$ , is called a 'nonresonant term'.

Silberberg and his coworkers showed a good experimental demonstration of the interference control [6] in a rubidium atom, where three states  $|5S_{1/2}\rangle = |g\rangle$ ,  $|5P_{3/2}\rangle = |i\rangle$  and  $|5D\rangle = |f\rangle$  form a three level ladder type system with  $\lambda_{ig} = 780$  nm and  $\lambda_{fi} = 776$  nm. They focussed on destructive interference of the nonresonant term and showed that transform limited pulses are not optimal to make two-photon transition between  $|g\rangle$  and  $|f\rangle$  in such a system. For better explanation of the interference control, we shall write the spectral electric field  $E(\omega)$  as  $E(\omega) = A(\omega)e^{i\Phi(\omega)}$  where  $A(\omega)$  is amplitude and  $\Phi(\omega)$  is phase. If applied pulse is transform limited, *i.e.*, has a constant spectral phase  $\Phi(\omega) = c$ , the resonant term is pure real while the nonresonant term is pure imaginary. Also, as shown in Eq. (2.6), a  $\pi$  phase discontinuity or a sign change occurs on nonresonant term at the  $\omega_{ig}$ , a resonant frequency of the transition between the ground state  $|g\rangle$  and the intermediate state  $|i\rangle$ . Thus, if the three-level ladder system is driven by a transform limited pulse, the two-photon transition probability is small because of destructive interference and not aligned probability amplitude component.

To maximize the two-photon transition probability, Silberberg and coworkers tried two approaches. One is directing the interference to a constructive one by manipulating phases of transition probability amplitude components. For this, they scanned  $\Phi(\omega) = \pi/2$  spectral phase window of about 4 nm width, which is described in Fig. 2.3 (a), through spectral range of the pulse by using spatial light modulator (SLM). Fig. 2.3 (b) shows the experimental result of the phase window scanning, which shows about 600% of maximum enhancement compared with transform limited case when the phase window centered at  $\omega_{fg}/2$ , 778 nm. Another approach is eliminating one of the two components which destructively

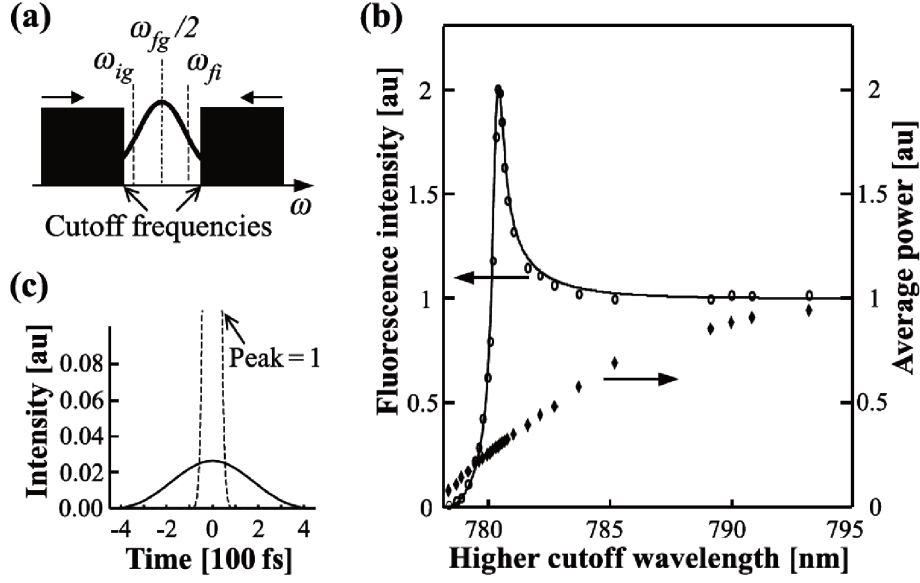


Figure 2.4: Quantum interference control in a three level ladder system via spectral blocking. (a) Description of variable slit located at the Fourier plane of pulse shaping apparatus. Blocked spectral region was varied by adjusting slit width. (b) Experimental result. Fluorescence from 5D state population was measured as a function of the cutoff frequency. About 100% of enhancement was obtained at maximum. (c) Comparison of temporal electric field between transform limited case (dotted line) and optimal pulse (solid line). Peak electric field of the pulse was reduced by a factor of 38. Figure from [6] (<https://doi.org/10.1103/PhysRevLett.86.47>).

interfere with the other. This time, a variable slit was placed on Fourier plane of the pulse shaping apparatus and width of the slit was varied to block certain outer part of the spectrum. This time, about 100% of transition probability enhancement was observed when the cutoffs are located at  $\omega_{ig}$  and  $\omega_{fi}$  as shown in Fig. 2.4 (b). Note that at the point of maximal probabilities, peak intensities of laser pulses were reduced in both schemes, to 71% and 2.6 % of transform limited case respectively. These are quite striking result because when the bandwidth of the pulse is kept constant, a transform limited pulse has maximal electric field. Silberberg and his coworkers showed that removing that destructive interference is much more important to maximize two-photon transition in three-level system rather than increasing electric field of driving pulse.

In our lab, J. Lim applied similar scheme to a V type system of rubidium, which consists of a ground state  $5S_{1/2}$  and two excited state  $5P_{1/2}$  (D1) and  $5P_{3/2}$  (D2) [13]. Dr. Lim utilized two-dimensional Fourier transform spectroscopy to separately observe inter-excited state two-photon transition of V type system. Fig. 2.5 (a) shows the phase window used in control experiment and experimental result. Maximum transition probability was obtained when  $3\pi/2$  was applied to the phase window. In this work, transition probability amplitude components were categorized into three terms, A, B, and C, based on their inherent phases. Phase of each term at marked points of the plot is shown in phasor diagrams, Fig. 2.5 (b), (c) and (d).

In above quantum control schemes, the approaches to control the transition probabilities are based on the equation, Eq (2.6), since the two-photon transition in three level system is quite simple to make analytic analysis. However, if the target of control is more complex, for example, dissociation

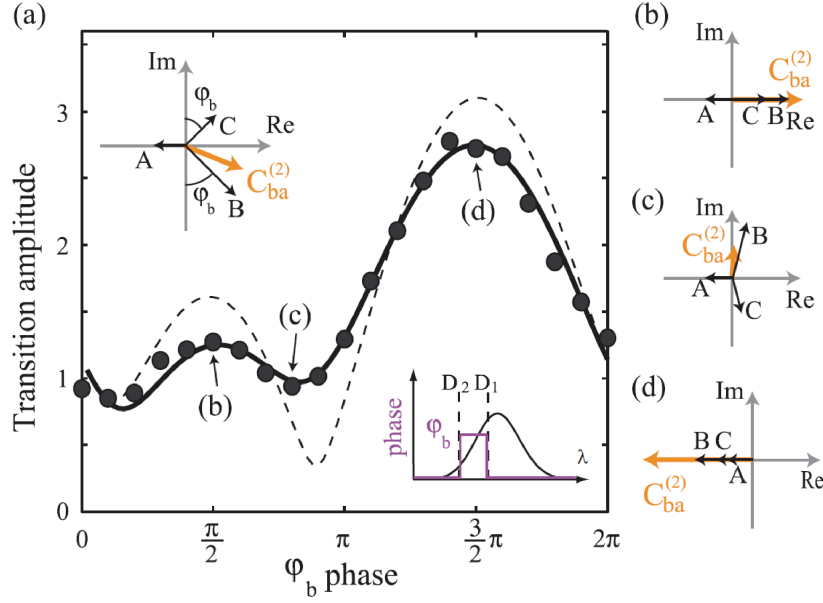


Figure 2.5: Quantum interference control of inter-excited state two-photon transition in a three level V-type system via phase window. (a) Measured inter-excited state transition probability as a function of phase applied on the phase window. Phase of the windowed region (shown in inset) was varied from 0 to  $2\pi$ . (b-d) Phasor diagram corresponds to each marked point of (a). Maximal transition probability occurred when all transition probability amplitude terms, A, B and C, are inphase, as shown in (c). Figure from [13].

of molecules, the adaptive control scheme can be used [cite]. The adaptive quantum control scheme needs a feedback loop which consists of a pulse shaping apparatus, a evolutionary algorithm and an appropriate detector. For each cycle of experiment, evolutionary algorithm modifies shape of the pulse and measured change of the target transition driven by the modified pulse is used as a feedback of the evolutionary algorithm. And after many cycles of the experiment, target transition becomes more and more efficient. The adaptive control scheme is very powerful since we can apply the scheme even if the detailed dynamics of the system is unknown. However, the analysis of the resulting maximal pulse shape is also very hard and can't give intuitive understanding. In my research, I focussed on quantum control in analytic approaches, which can be expanded and applied to similar type of system.

## 2.3 Quantum control in strong field regime

### 2.3.1 CPI and CPT in two-level system

If the electric field amplitude of the pulse becomes larger, solution of the Schödinger equation can not be approximated by few terms. In a two-level system driven by such high electric field, complete probability inversion (CPI), where an initial state  $|g\rangle$  completely becomes a final state  $|e\rangle$ , and complete probability return (CPR), where an initial state  $|g\rangle$  completely remains in a final state  $|g\rangle$  after the interaction, can be occurred. The most famous dynamics which can induce CPI and CPR is Rabi oscillation, first discovered in the context of nuclear magnetic resonance (NMR) [14, 15] and later extended to atomic physics and quantum optics [16, 17]. In the presence of a resonant driving field  $E(t) = A(t) \cos(\omega_0 t)$ , a

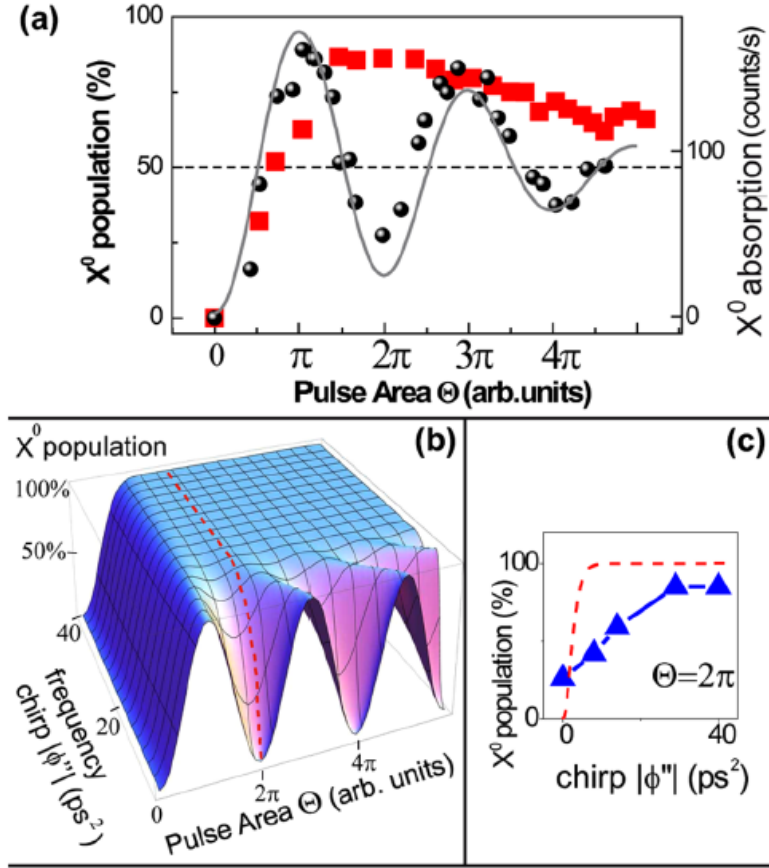


Figure 2.6: (a) Comparison between experimental results of Rabi oscillation (black circle) and rapid adiabatic passage (red square) of single quantum dot. RAP shows robustness of CPI after threshold pulse area  $\Theta > \pi$ . (b) Calculation result of transition probability of a quantum dot as functions of pulse area  $\Theta$  and linear frequency chirp. (c) Experimental result of transition probability as a function of chirp with fixed pulse area  $\Theta = 2\pi$ . CPI is shown when  $|\phi''| > 30 \text{ ps}^2$ . Figure from [29] (<https://doi.org/10.1103/PhysRevLett.106.166801>).

two-state quantum system undergoes a cyclic change of

$$P(|e\rangle) = \sin^2(\Theta/2), \quad (2.7)$$

where the pulse area  $\Theta$  is given by

$$\Theta = \int dt \frac{\mu}{\hbar} A(t), \quad (2.8)$$

with  $\mu$  is a transition dipole moment and  $A(t)$  is the envelope of the electric field. As shown in Eq. (2.7), the CPI of the system occurs when  $\Theta = (2n - 1)\pi$ , and the CPR of the system occurs when  $\Theta = (2n)\pi$  with  $n = 1, 2, 3, \dots$ . This generic feature of Rabi oscillation is universally found in a vast variety of material systems ranging from atoms and molecules [18, 19, 20] to quantum wells and dots [21, 22], superconducting quantum devices [23], and Bose-Einstein condensates [24], etc.

Another example of the phenomena which can induce CPI is adiabatic evolution. In quantum mechanics, an evolution is called adiabatic when it is slow enough to keep the state as an eigenstate of the Hamiltonian at every moment during process [9]. Famous examples of the adiabatic CPI techniques are stimulated Raman adiabatic passage (STIRAP), which uses slow electric field ramping of  $\sim \mu\text{s}$  regime



to achieve adiabatic condition [25, 26], and stark chirped rapid adiabatic passage (SCRAP), which uses slowly varying Stark shift of the state energy in  $\sim$  ns regime [27]. Here, 'slowly varying' means relatively slow change comparing to the interaction time.

For broadband pulses, slowly varying instantaneous frequency can cause adiabatic evolution of the system, which is called rapid adiabatic passage (RAP) since this kind of adiabatic interaction is usually much faster than the life time of the state [28]. When high linear chirp is applied to the broadband pulse, instantaneous carrier frequency of the pulse is modulated as a linear function of time. For a linearly chirped broadband pulse with instantaneous carrier frequency  $\omega(t) = \omega_0 + \alpha t$ , two eigenstate of the interaction between two-level system and the pulse is given by

$$|\Psi_+(t)\rangle = \sin(\theta(t))|g\rangle + \cos(\theta(t))|e\rangle \quad (2.9)$$

$$|\Psi_-(t)\rangle = \cos(\theta(t))|g\rangle - \sin(\theta(t))|e\rangle, \quad (2.10)$$

where mixing angle  $\theta(t)$  is defined by

$$\theta(t) = \frac{1}{2} \tan^{-1} \left( \frac{\Omega(t)}{\Delta(t)} \right) \quad (2.11)$$

$$\Omega(t) = \frac{\mu}{\hbar} A(t) \quad (2.12)$$

$$\Delta(t) = \omega_{eg} - \omega(t). \quad (2.13)$$

To see the basic concept of the dynamics, let us assume that the center frequency of the pulse is the resonant frequency of the transition,  $\omega_{eg} = \omega_0$  and the pulse is a Gaussian pulse  $A(t) = E_0 \exp[-t^2/\tau^2]$ , which is centered at  $t=0$ . Then, if the frequency modulation by linear chirp  $\alpha$  is positive, we have

$$\begin{aligned} \frac{\Omega(t \rightarrow -\infty)}{\Delta(t \rightarrow -\infty)} &= +0 \\ \frac{\Omega(t \rightarrow -0)}{\Delta(t \rightarrow -0)} &= \infty \\ \frac{\Omega(t \rightarrow +0)}{\Delta(t \rightarrow +0)} &= -\infty \\ \frac{\Omega(t \rightarrow \infty)}{\Delta(t \rightarrow \infty)} &= -0. \end{aligned}$$

According to the time dependent change of  $\Omega(t)/\Delta(t)$ , the mixing angle starts from  $\theta(t \rightarrow -\infty) = \pi/2$ , changes through  $\theta(t \rightarrow 0) = \pi/4$  and finally becomes  $\theta(t \rightarrow 0) = 0$ . Thus, if the evolution is adiabatic,  $|g\rangle$  becomes  $|e\rangle$  after the evolution along  $|\Psi_+(t)\rangle$  and  $|e\rangle$  becomes  $|g\rangle$  after the evolution along  $|\Psi_-(t)\rangle$ , which results CPI of the system. The adiabatic condition of the interaction can be examined by the adiabaticity function [28], which is given by

$$f(t) = \frac{1}{2} \frac{|\dot{\Omega}(t)\Delta(t) - \Omega(t)\dot{\Delta}(t)|}{[\sqrt{\Omega^2 + \Delta^2}]^3}. \quad (2.14)$$

The evolution is adiabatic when  $f(t) \ll 1$ , which requires large electric field and linear chirp. However, in RAP, unlike the Rabi oscillation, CPI always takes place beyond certain thresholds of electric field and linear chirp. Moreover, even if the center frequency of the laser pulse is detuned, CPI by RAP also occurs unless the resonant frequency of the transition located outside of the laser pulse spectrum. The robustness of the CPI by RAP gives great advantage to make CPI of inhomogeneous ensemble. A good example is quantum dots. Since the artificial systems have unexpected error, resonant frequency of each quantum dot is slightly different from desired one. Therefore, if we try to make CPI of the ensemble of

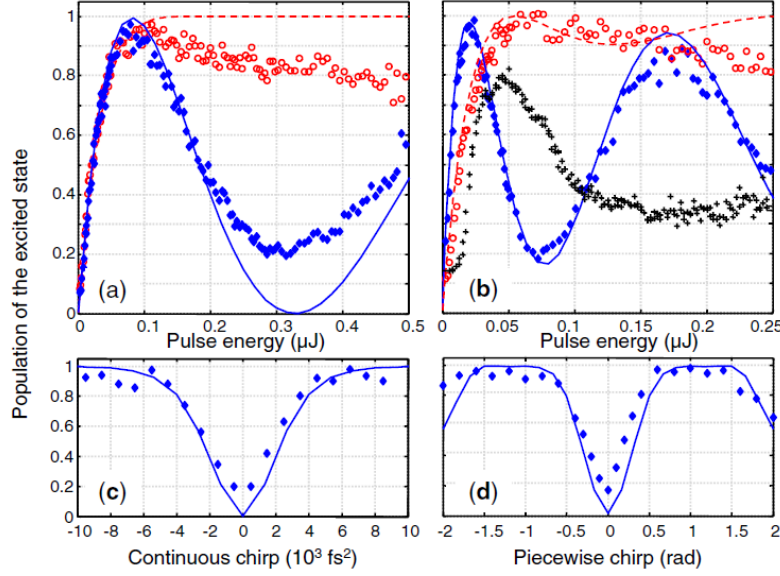


Figure 2.7: Comparison between the excitation dynamics by a single pulse (left) and 7 pulse train (right). For (a) and (b), blue solid line and dots are calculation and experimental results of Rabi oscillation, respectively. Red dashed line and dots are calculation and experimental results of adiabatic process, respectively. The adiabatic process in (a) is RAP by a single chirped pulse and in (b) is PAP (piecewise adiabatic passage) by piecewisely chirped 7 pulse train. Figure from [31] (<https://doi.org/10.1103/PhysRevLett.100.103004>)

quantum dots by Rabi oscillation, each quantum dot experiences respective detunings, which results in imperfect CPI of each quantum dot. However, if the ensemble of quantum dots is driven by a linearly chirped pulse, robustness of the RAP can induce consistent CPI to all individual quantum dots [29, 30]. Another interesting result involving adiabatic evolution by chirping is studied by Milner and coworkers [31]. Instead of a single chirped pulse, they made a train of 7 ultrashort pulses, which are programmed to be chirped piecewisely. They theoretically shown that the adiabaticity function  $f(t)$  can be kept small enough during total time evolution even for a train of pulses. They also experimentally shown that the piecewisely chirped pulse can mimic the adiabatic evolution by a single chirped pulse. Fig. 2.7 shows there experimental result, which shows that comparison between the excitation dynamics by a single chirped pulse (left) and a piecewisely chirped pulse train (right).

The robustness of RAP also has advantage on spatially averaged interaction, which will be discussed following subsection.

### 2.3.2 Spatially averaged interaction

Because of spatial profile of laser electric field, particles in an ensemble experiences position dependent difference of electric field amplitude. When the interaction is in weak field regime, this makes no difference comparing to single particle case because the dependence on electric field can be expressed by only a single degree of polynomial, for example,  $E^2(\omega)$  for two-photon transition. However, dynamics in higher field regime must be described by infinite series on  $E(t)$ , for instance, Rabi oscillation is  $\sin^2(\int E(t)dt)$ . Thus, spatial profile of laser field and ensemble cause spatially averaged dynamics which can result complete wipe out of the behavior. Several experimental techniques attempted to overcome

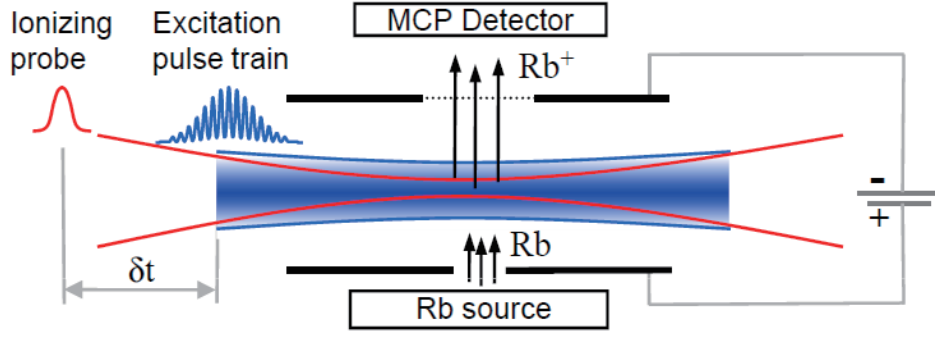


Figure 2.8: Diagram of a setup designed to reduce spatial averaging by limiting detection region. Excited state populations from only small central volume of interaction can be ionized and detected by a tightly focussed probe beam. Figure from [31] (<https://doi.org/10.1103/PhysRevLett.100.103004>)

such spatial averaging effect and we shall review three of those here. Uniformization of laser beam's spatial profile is the one of the solutions. J. Lim and his coworkers of our lab made flattop beam by using set of refractive optical elements [32] and observed two-photon Rabi oscillation of rubidium atoms. Weidemüller and his coworkers also made a flattop beam using diffractive optics and utilized it for performing Rabi oscillation of a Rydberg state of atoms [33]. Another solution is limitation of detection area. In this method, excited state populations in an ensemble are ionized by a probe beam. Therefore, even if Rabi oscillation is driven by a wide pump beam, detection area can be limited by a small probe beam. Milner and his coworkers used such a method to observe Rabi oscillation induced by femtosecond pulses [31]. Fig. 2.8 shows their detection scheme. Spatially confined ensembles like hot vapors in a microcell or cold atoms trapped in MOT also can be a solution. Recent results of our lab used a small cold atomic cloud to conduct intensity sensitive experiment such as ultrafast Ramsey spectroscopy and single qubit quantum gate operations [34].

Although ensembles have been widely used for experiments, however, organized quantitative analysis of ensemble averaged Rabi oscillation still have not been done yet. In chapter 6, we conduct quantitative analysis of the spatially average Rabi oscillation.

## Chapter 3. Theoretical backgrounds

### 3.1 Electric field notation

In this section, We discuss electric field notation and phase conversion which will be used for entire dissertation. Starting from spectral electric field, phase conversion of the spectral electric field will be discussed using concept of the linear chirp.

For a broadband laser pulse, we can define a spectral electric field  $E(\omega)$  with its spectral amplitude  $A(\omega)$  and spectral phase  $\Phi(\omega)$  as

$$E(\omega) = A(\omega)e^{i\Phi(\omega)}, \quad (3.1)$$

where sign of the the spectral phase is defined as  $+$  and the phase term is then given by  $e^{i\Phi(\omega)}$ , not  $e^{-i\Phi(\omega)}$ . Time domain electric field is given by Fourier transform relation. We define Fourier transform relation between spectral domain electric field  $E(\omega)$  and time domain electric field  $E(t)$  as

$$E(t) = \int_{-\infty}^{\infty} E(\omega)e^{-i\omega t} d\omega \quad (3.2)$$

$$E(\omega) = \int_{-\infty}^{\infty} E(t)e^{i\omega t} dt, \quad (3.3)$$

where  $E(t)$  is defined as a Fourier transform of  $E(\omega)$  and  $E(\omega)$  is defined as an inverse Fourier transform of  $E(t)$ .

The spectral phase  $\Phi(\omega)$  is usually written in a series form as

$$\Phi(\omega) = c_0 + c_1(\omega - \omega_0) + \frac{c_2}{2!}(\omega - \omega_0)^2 + \dots, \quad (3.4)$$

where  $\omega_0$  is a center frequency of the spectral phase, commonly set to the center frequency of a broadband pulse. Each proportional constant,  $c_n$ , in Eq. (3.4) gives unique property on a transformed time domain electric field. For example,  $c_0$  is a overall constant phase. It has no effect on envelope of the time-domain electric field but changes phase difference between carrier and envelope of the pulse, which is usually called Carrier-Envelope Phase (CEP).  $c_1$  describes spectral phase linearly depends on the frequency, which affects on temporal center of the time-domain envelope.

A pulse whose spectral phase has quadratic dependence on  $\omega$ ,  $\Phi(\omega) = \frac{c_2}{2}\omega - \omega_0$ , is called linearly chirped pulse. Time domain electric field of a linearly chirped pulse can be obtained by Fourier transform of the spectral electric field,

$$E(\omega) = E_0 \exp \left[ -\frac{(\omega - \omega_0)^2}{\Delta\omega^2} \right] \exp \left[ i\frac{c_2}{2}(\omega - \omega_0)^2 \right]. \quad (3.5)$$

And transformed time domain electric field is given by

$$\begin{aligned} E(t) &= \frac{E_0 \Delta\omega}{\sqrt{2}} \sqrt{\frac{\tau_0}{\tau}} \exp \left( i\frac{\phi}{2} \right) \exp \left( -\frac{t^2}{\tau^2} \right) \exp \left[ -i \left( \omega_0 t + \frac{2c_2 t^2}{\tau_0^4 + 4c_2^2} \right) \right] \\ &= \tilde{A}(t) \exp [-i\omega(t)t], \end{aligned} \quad (3.6)$$

where  $\tau_0 = \frac{2}{\Delta\omega}$ ,  $\tau = \tau_0 \sqrt{1 + \frac{4c_2^2}{\tau_0^4}}$ ,  $\phi = \tan^{-1} \left( \frac{2c_2}{\tau_0} \right)$  and a time-dependent effective carrier frequency  $\omega(t)$  is  $\omega(t) = \omega_0 + \frac{2c_2}{\tau_0^4 + 4c_2^2}$ . As shown by  $\omega(t)$ , a linearly chirped pulse is a pulse which has a frequency sweep linearly depending on time.

Note that the phase sign of Eq. (3.1) and Fourier transform relation in Eq. (3.3) are defined as a convention, without losing generality. Since physical meaning of positively (negatively) chirped pulse is a pulse whose instantaneous frequency increases (decreases) as a function of time, our convention of phase sign and Fourier transform relation is intended to make sign of  $\Delta\omega(t) = \omega(t) - \omega_0 = \frac{2c_2}{\tau_0^4 + 4c_2^2}$  equals to the sign of its parameter  $c_2$  for convenience. If the phase term of Eq. (3.1) is given as  $e^{-i\Phi(\omega)}$ , Fourier transform relation of Eq. (3.3) must be reversed to match chirp signs as above.

## 3.2 Femtosecond Rabi oscillation

When a two level system interacts with an oscillating electric field, probabilities of ground state  $|0\rangle$  and excited state  $|1\rangle$  show oscillatory behaviors as functions of time. This probability oscillation is called Rabi oscillation, named in honor of Nobel laureate Isidor Isaac Rabi. To see the dynamics of the Rabi oscillation, we start from the following Hamiltonian in Schrödinger picture

$$H = \begin{pmatrix} 0 & \mu E(t) \\ \mu E(t) & \hbar\omega_0 \end{pmatrix}, \quad (3.7)$$

where  $\omega_0$  is a resonant frequency for the transition between two states,  $\mu = \int dV \langle 1|er|0\rangle$  is a transition dipole moment,  $E(t)$  is a time dependent electric field, and  $\mu E(t)$  describes electric dipole interaction between the system and electric field. Here, size of our two level system, *i. e.*, an atom, is assumed as much smaller than wave length of electric field. Thus, position dependence of the electric field is eliminated and this approximation is called dipole approximation. Then, the time evolution of the system is then given by schrödinger equation

$$i\hbar \frac{\partial}{\partial t} |\psi\rangle = H|\psi\rangle, \quad (3.8)$$

However, it is more convenient to describe time evolution of the system in interaction picture [35]. Hamiltonian in Eq. (3.7) can be separated into two part as

$$\begin{aligned} H &= H_0 + V \\ &= \begin{pmatrix} 0 & 0 \\ 0 & \hbar\omega_0 \end{pmatrix} + \begin{pmatrix} 0 & \mu E(t) \\ \mu E(t) & 0 \end{pmatrix}, \end{aligned} \quad (3.9)$$

and the time evolution equation in Eq. (3.8) can be rewritten as

$$\begin{aligned} i\hbar \frac{\partial}{\partial t} |\psi\rangle_I &= i\hbar \frac{\partial}{\partial t} \left( e^{iH_0 t/\hbar} |\psi\rangle \right) \\ &= -H_0 e^{iH_0 t/\hbar} |\psi\rangle + e^{iH_0 t/\hbar} (H_0 + V) |\psi\rangle \\ &= e^{iH_0 t/\hbar} V e^{-iH_0 t/\hbar} e^{iH_0 t/\hbar} |\psi\rangle \\ &= V_I |\psi\rangle_I, \end{aligned} \quad (3.10)$$

where  $|\psi\rangle_I = e^{iH_0 t/\hbar} |\psi\rangle$  is a state ket in interaction picture. Thus, we can find interaction picture Hamiltonian  $V_I$  from Schrödinger picture Hamiltonian  $H$  by

$$\begin{aligned} V_I &= e^{iH_0 t/\hbar} V e^{-iH_0 t/\hbar} \\ &= \begin{pmatrix} 1 & 0 \\ 0 & e^{i\omega_0 t} \end{pmatrix} \begin{pmatrix} 0 & \mu E(t) \\ \mu E(t) & 0 \end{pmatrix} \begin{pmatrix} 1 & 0 \\ 0 & e^{-i\omega_0 t} \end{pmatrix} \\ &= \begin{pmatrix} 0 & \mu E(t) e^{-i\omega_0 t} \\ \mu E(t) e^{i\omega_0 t} & 0 \end{pmatrix}. \end{aligned} \quad (3.11)$$

An electric field of a laser pulse centered at the resonant frequency of the system  $\omega_0$  is given by

$$\begin{aligned} E(t) &= E_0 A(t) \cos(\omega_0 t) \\ &= \frac{E_0}{2} A(t) (e^{-i\omega_0 t} + e^{i\omega_0 t}), \end{aligned} \quad (3.12)$$

where  $A(t)$  is a temporal envelope of the pulse. For a Gaussian pulse,  $A(t) = e^{-t^2/\tau^2}$ . Then, the time evolution of the system is given by Eq. (3.10) and Eq. (3.11) as

$$i\hbar \begin{pmatrix} \dot{c}_0(t) \\ \dot{c}_1(t) \end{pmatrix} = \frac{1}{2} \begin{pmatrix} 0 & \mu E_0 A(t) (1 + e^{-i2\omega_0 t}) \\ \mu E_0 A(t) (1 + e^{i2\omega_0 t}) & 0 \end{pmatrix} \begin{pmatrix} c_0(t) \\ c_1(t) \end{pmatrix}. \quad (3.13)$$

Here, fast oscillation described by the  $e^{\pm i2\omega_0 t}$  terms in Eq. (3.13) is rapidly averaged out and can be neglected. The approximation which ignores such a fast oscillation is called rotating wave approximation (RWA) [36]. Under the RWA, Eq. (3.13) becomes,

$$i\hbar \begin{pmatrix} \dot{c}_0(t) \\ \dot{c}_1(t) \end{pmatrix} = \frac{1}{2} \begin{pmatrix} 0 & \mu E_0 A(t) \\ \mu E_0 A(t) & 0 \end{pmatrix} \begin{pmatrix} c_0(t) \\ c_1(t) \end{pmatrix}. \quad (3.14)$$

Since the matrix of Eq. (3.14) in different time commute, we can find the time evolution operator  $U_I(t, t_0)$  of the state as

$$\begin{aligned} |\psi(t, t_0)\rangle_I &= U_I(t, t_0) |\psi(t_0)\rangle_I \\ U_I(t, t_0) &= \exp \left[ -i \int_{t_0}^t \frac{1}{2\hbar} \begin{pmatrix} 0 & \mu E_0 A(t') \\ \mu E_0 A(t') & 0 \end{pmatrix} dt' \right]. \end{aligned} \quad (3.15)$$

Let us define pulse area  $\Theta(t)$  and  $\Theta(t, t_0)$  as

$$\begin{aligned} \Theta(t) &= \lim_{t_0 \rightarrow -\infty} \int_{t_0}^t \frac{1}{\hbar} \mu E_0 A(t') dt' \\ \Theta(t, t_0) &= \int_{t_0}^t \frac{1}{\hbar} \mu E_0 A(t') dt' = \Theta(t) - \Theta(t_0). \end{aligned} \quad (3.16)$$

Then,

$$U_I(t, t_0) = \exp \left[ -i \begin{pmatrix} 0 & \Theta(t, t_0)/2 \\ \Theta(t, t_0)/2 & 0 \end{pmatrix} \right], \quad (3.17)$$

and using diagonalization of matrix

$$\begin{pmatrix} 0 & \Theta(t, t_0)/2 \\ \Theta(t, t_0)/2 & 0 \end{pmatrix} = \frac{1}{\sqrt{2}} \begin{pmatrix} -1 & 1 \\ 1 & 1 \end{pmatrix} \begin{pmatrix} -\Theta(t, t_0)/2 & 0 \\ 0 & \Theta(t, t_0)/2 \end{pmatrix} \frac{1}{\sqrt{2}} \begin{pmatrix} -1 & 1 \\ 1 & 1 \end{pmatrix}, \quad (3.18)$$

and finally we have

$$\begin{pmatrix} c_0(t) \\ c_1(t) \end{pmatrix} = \begin{pmatrix} \cos(\Theta(t, t_0)/2) & -i \sin(\Theta(t, t_0)/2) \\ -i \sin(\Theta(t, t_0)/2) & \cos(\Theta(t, t_0)/2) \end{pmatrix} \begin{pmatrix} c_0(t_0) \\ c_1(t_0) \end{pmatrix}, \quad (3.19)$$

which describes Rabi oscillation by a resonant pulse. Note that the Rabi oscillation depends on the half of the pulse area  $\Theta(t, t_0)$ .

### 3.3 Multiphoton absorption in weak field regime

Time dependent perturbation theory says that in the interaction picture the transition probability amplitude from initial state  $|g\rangle$  to final state  $|f\rangle$  driving by a time dependent interaction  $V_I(t)$  can be expanded in series as

$$\begin{aligned}
c_f^{(0)} &= \delta_{fg} \\
c_f^{(1)} &= -\frac{i}{\hbar} \int_{t_0}^t dt_1 \langle f | V_I(t_1) | g \rangle \\
&= -\frac{i}{\hbar} \int_{t_0}^t dt_1 e^{i\omega_{fg}t_1} V_{fg}(t_1) \\
c_f^{(2)} &= \left(-\frac{i}{\hbar}\right)^2 \sum_m \int_{t_0}^t dt_1 \int_{t_0}^{t_1} dt_2 \langle f | V_I(t_1) | m \rangle \langle m | V_I(t_2) | g \rangle \\
&= \left(-\frac{i}{\hbar}\right)^2 \sum_m \int_{t_0}^t dt_1 \int_{t_0}^{t_1} dt_2 e^{i\omega_{fm}t_1} V_{fm}(t_1) e^{i\omega_{mg}t_2} V_{mg}(t_2) \\
&\vdots,
\end{aligned} \tag{3.20}$$

which is called Dyson series [35]. Here, time dependent probability  $P_f$  of the state  $|f\rangle$  is given by sum of the series as

$$\begin{aligned}
c_f &= \sum_k c_f^{(k)} \\
P_f &= |c_f|^2,
\end{aligned} \tag{3.21}$$

where  $c_f$ , sum of the series, is called a transition probability amplitude. As in Eq. (3.7), we can represent interaction between the atom and an electric field as  $V_{pq} = \mu_{pq}E(t)$ , where  $\mu_{pq} = \int dV \langle p | e r | q \rangle$  (here  $e$  is a unit charge), is a transition dipole moment between two states  $|p\rangle$  and  $|q\rangle$ . Note that  $k^{th}$  order term  $c_f^{(k)}$  in Eq. (3.21) describes a transition which consists of  $k$  distinct interactions or involves  $k$  photons. In weak field regime, the lowest possible order of transition between  $|f\rangle$  and  $|g\rangle$  becomes dominant. Representing Eq. (3.21) in spectral domain will be suitable for intuitive understading. Here,  $c_f^{(2)}$  will be considered as an example of such a transform. Starting from  $c_f^{(2)}$  of Eq. (3.21), using Fourier transform relation in Eq. (3.4), we have

$$\begin{aligned}
c_f^{(2)} &= \left(-\frac{i}{\hbar}\right)^2 \sum_m \int_{t_0}^t dt' \int_{t_0}^{t'} dt'' e^{i\omega_{fm}t'} \mu_{fm} E(t') e^{i\omega_{mg}t''} \mu_{mg} E(t'') \\
&= \left(-\frac{i}{\hbar}\right)^2 \sum_m \int_{t_0}^t dt' \int_{t_0}^{t'} dt'' \int_{-\infty}^{\infty} d\omega_1 \int_{-\infty}^{\infty} d\omega_2 e^{i(\omega_{fm}-\omega_1)t'} \mu_{fm} E(\omega_1) e^{i(\omega_{mg}-\omega_2)t''} \mu_{mg} E(\omega_2) \\
&= -\sum_m \frac{\mu_{fm}\mu_{mg}}{\hbar^2} \int_{-\infty}^{\infty} d\omega_1 \int_{-\infty}^{\infty} d\omega_2 \int_{t_0}^t dt' E(\omega_1) E(\omega_2) \frac{e^{i(\omega_{fg}-\omega_1-\omega_2)t'} - e^{i(\omega_{fm}-\omega_1)t'} e^{i(\omega_{mg}-\omega_2)t_0}}{i(\omega_{mg}-\omega_2)} \\
&= -\sum_m \frac{\mu_{fm}\mu_{mg}}{\hbar^2} \int_{-\infty}^{\infty} d\omega_1 \int_{-\infty}^{\infty} d\omega_2 E(\omega_1) E(\omega_2) \\
&\quad \times \left[ \frac{e^{i(\omega_{fg}-\omega_1-\omega_2)t} - e^{i(\omega_{fg}-\omega_1-\omega_2)t_0}}{i(\omega_{fg}-\omega_1-\omega_2)i(\omega_{mg}-\omega_2)} - \frac{e^{i(\omega_{fm}-\omega_1)t} - e^{i(\omega_{fm}-\omega_1)t_0}}{i(\omega_{fm}-\omega_1)i(\omega_{mg}-\omega_2)} e^{i(\omega_{mg}-\omega_2)t_0} \right]. \tag{3.22}
\end{aligned}$$

Using contour integral and residue theorem, Eq. (3.21) becomes

$$c_f^{(2)} = -\pi \sum_m \frac{\mu_{fm}\mu_{mg}}{\hbar^2} E(\omega_{fm}) E(\omega_{mg}) + i \sum_m \frac{\mu_{fm}\mu_{mg}}{\hbar^2} \oint \int_{-\infty}^{\infty} \frac{E(\omega) E(\omega_{fg}-\omega)}{\omega_{mg}-\omega} d\omega.$$

Eq. (3.23) describes two photon transition probability amplitude between  $|g\rangle$  and  $|f\rangle$  with intermediate states  $|m\rangle$ s.

In addition, Rabi oscillation described in a series form would be helpful to figure out how a weak field regime can be defined. Starting from Eq. (3.21), using a two level system consist of a ground state  $|g\rangle$  and excited state  $|e\rangle$  with a resonant frequency  $\omega_0$  and a transition dipole moment  $\mu$ , we have

$$\begin{aligned}
c_f^{(0)} &= \delta_{fg} = 0 \\
c_f^{(1)} &= -\frac{i}{\hbar} \int_{t_0}^t dt_1 \langle f|V_I(t_1)|g \rangle \\
&= -\frac{i\mu}{2\hbar} \int_{t_0}^t dt_1 \left( e^{i(\omega_0+\omega_0)t_1} + e^{i(\omega_0-\omega_0)t_1} \right) A(t_1) \\
&= -\frac{i\mu}{2\hbar} \int_{t_0}^t dt_1 (e^{i2\omega_0 t_1} + 1) A(t_1) \\
c_f^{(2)} &= \left( -\frac{i}{\hbar} \right)^2 \sum_m \int_{t_0}^t dt_1 \int_{t_0}^{t_1} dt_2 \langle f|V_I(t_1)|m \rangle \langle m|V_I(t_2)|g \rangle = 0 \\
c_f^{(3)} &= \left( -\frac{i}{\hbar} \right)^3 \sum_{m_1} \sum_{m_2} \int_{t_0}^t dt_1 \int_{t_0}^{t_1} dt_2 \int_{t_0}^{t_2} dt_3 \langle f|V_I(t_1)|m_2 \rangle \langle m_2|V_I(t_2)|m_1 \rangle \langle m_1|V_I(t_3)|g \rangle \\
&= \left( -\frac{i}{\hbar} \right)^3 \int_{t_0}^t dt_1 \int_{t_0}^{t_1} dt_2 \int_{t_0}^{t_2} dt_3 \langle f|V_I(t_1)|g \rangle \langle g|V_I(t_2)|f \rangle \langle f|V_I(t_3)|g \rangle \\
&= \left( -\frac{i\mu}{2\hbar} \right)^3 \int_{t_0}^t dt_1 \int_{t_0}^{t_1} dt_2 \int_{t_0}^{t_2} dt_3 (e^{i2\omega_0 t_1} + 1) A(t_1) (1 + e^{-i2\omega_0 t_2}) A(t_2) (e^{i2\omega_0 t_3} + 1) A(t_3) \\
&\vdots
\end{aligned} \tag{3.23}$$

where the state of the system is initially  $|\psi(t_0)\rangle = |g\rangle$  and the electric field of the laser pulse is centered at  $\omega_0$ . For Eq. (3.23), we have used the relation  $\langle f|V_I(t)|f \rangle = \langle g|V_I(t)|g \rangle = 0$ . Then, using RWA, Eq.(3.23) becomes,

$$\begin{aligned}
c_f^{(2n)} &= 0 \\
c_f^{(2n+1)} &= \left( -\frac{i\mu}{2\hbar} \right)^{2n+1} \int_{t_0}^t dt_1 \int_{t_0}^{t_1} dt_2 \cdots \int_{t_0}^{t_{2n}} dt_{2n+1} A(t_1) A(t_2) \cdots A(t_{2n+1}).
\end{aligned} \tag{3.24}$$

Since integrand of Eq. (3.24) is physically invariant under exchanging order of variables, we have

$$\begin{aligned}
c_f^{(2n+1)} &= \frac{1}{(2n+1)!} \left( -\frac{i\mu}{2\hbar} \right)^{2n+1} \int_{t_0}^t dt_1 \int_{t_0}^{t_1} dt_2 \cdots \int_{t_0}^{t_{2n}} dt_{2n+1} A(t_1) A(t_2) \cdots A(t_{2n+1}) \\
&= \frac{1}{(2n+1)!} \left( -\frac{i}{2} \right)^{2n+1} \Theta(t, t_0)^{2n+1},
\end{aligned} \tag{3.25}$$

where  $(2n+1)!$  is a permutation of  $2n+1$  variables and  $\Theta(t, t_0)$  is the pulse area defined in Eq. (3.16). Finally, time dependent transition probability amplitude in Eq. (3.21) is given by sum of the series as

$$\begin{aligned}
c_f &= -i \sum_{n=0}^{\infty} \frac{(-1)^n}{(2n+1)!} \left[ \frac{\Theta(t, t_0)}{2} \right]^{2n+1} \\
&= -i \sin \left( \frac{\Theta(t, t_0)}{2} \right),
\end{aligned} \tag{3.26}$$

which is identical to the result of Eq. (3.19).

The result of Eq. (3.26) shows that the Rabi oscillation can be regarded as a summation of all possible interactions between a system and a electric field. From this result, we can conclude that the criteria of weak field regime is justified by the pulse area  $\Theta(t, t_0) \ll 1$ , not the electric field  $E(t) \ll 1$ .



### 3.4 Population inversion by linearly chirped electric field

#### 3.4.1 Interaction Hamiltonian of a linearly chirped pulse

In this section, we discuss about mathematical fomulation of a linearly chirped pulse and evolution of a atomic system interacting with a linearly chirped pulse. We start from the result of Eq. (3.6),

$$\begin{aligned} E(t) &= \frac{E_0 \Delta \omega}{\sqrt{2}} \sqrt{\frac{\tau_0}{\tau}} \exp\left(i \frac{\phi}{2}\right) \exp\left(-\frac{t^2}{\tau^2}\right) \exp\left[-i \left(\omega_0 t + \frac{2c_2 t^2}{\tau_0^4 + 4c_2^2}\right)\right] \\ &= \tilde{A}(t) \exp[-i\omega(t)t], \end{aligned} \quad (3.27)$$

where  $\tau_0 = \frac{2}{\Delta\omega}$ ,  $\tau = \tau_0 \sqrt{1 + \frac{4c_2^2}{\tau_0^4}}$ ,  $\phi = \tan^{-1}\left(\frac{2c_2}{\tau_0^2}\right)$  and a time-dependent effective carrier frequency  $\omega(t)$  is  $\omega(t) = \omega_0 + \frac{2c_2}{\tau_0^4 + 4c_2^2}t$ . As shown by  $\omega(t)$ , a linearly chirped pulse is a pulse which has time-dependent frequency sweep, specifically linear on time. Interaction between linearly chirped pulse and the atomic system is described by a Hamiltonian of

$$H = \begin{pmatrix} 0 & \mu E(t) \\ \mu E^*(t) & \hbar \omega_e \end{pmatrix}, \quad (3.28)$$

where  $E(t)$  is the time-domain electric field given in Eq. (3.27). Transform to appropriate interaction picture is very helpful for eliminating the time-dependence. After rearranging matrix, we have

$$\begin{aligned} H &= H_0 + V \\ &= \begin{pmatrix} 0 & 0 \\ 0 & \hbar \omega(t) \end{pmatrix} + \begin{pmatrix} 0 & \mu E(t) \\ \mu E^*(t) & \hbar \Delta(t) \end{pmatrix}, \end{aligned} \quad (3.29)$$

where  $\Delta(t) = \omega_e - \omega(t)$  is time dependent detuning. Corresponding interaction Hamintonian is given as

$$\begin{aligned} V_I &= \exp\left[\frac{iH_0 t}{\hbar}\right] V \exp\left[\frac{-iH_0 t}{\hbar}\right] \\ &= \begin{pmatrix} 0 & \mu E(t) \exp[-i\omega(t)t] \\ \mu E^*(t) \exp[i\omega(t)t] & \hbar \Delta(t) \end{pmatrix}. \end{aligned} \quad (3.30)$$

Here, we can apply rotating wave approximation(RWA) to eliminate fast oscillation, which can't be observed at our time window. Also, without losing of generality, we can include constant phase  $\phi$  of  $\tilde{A}(t)$  into basis. Finally, the interaction picture equation after RWA is given as

$$\begin{aligned} \begin{pmatrix} \dot{C}_g \\ \dot{C}_e \end{pmatrix} &= \frac{-i}{\hbar} \begin{pmatrix} 0 & \frac{1}{2}\mu A(t) \\ \frac{1}{2}\mu A(t) & \hbar \Delta(t) \end{pmatrix} \begin{pmatrix} C_g \\ C_e \end{pmatrix} \\ &= -i \begin{pmatrix} 0 & \frac{1}{2}\Omega(t) \\ \frac{1}{2}\Omega(t) & \Delta(t) \end{pmatrix} \begin{pmatrix} C_g \\ C_e \end{pmatrix}, \end{aligned} \quad (3.31)$$

where  $\Omega(t) = \mu A(t)/\hbar$ .

#### 3.4.2 Adiabatic population inversion by a linearly chirped pulse

The characteristic equation of interaction Hamiltonian in Eq. (3.31) is

$$\lambda^2 - \Delta(t)\lambda - \frac{1}{4}\Omega^2(t) = 0, \quad (3.32)$$

and corresponding eigenvalues and eigenstates are

$$\begin{aligned}\lambda_{\pm}(t) &= \frac{\Delta(t) \pm \sqrt{\Delta(t)^2 + \Omega^2(t)}}{2} \\ &= \frac{\Delta(t) \pm \Omega'(t)}{2},\end{aligned}\tag{3.33}$$

where  $\Omega'(t) = \sqrt{\Delta(t)^2 + \Omega^2(t)}$  is a generalized Rabi frequency. From the following equations, Eq. (3.34) and Eq. (3.35),

$$\frac{C_{\pm,g}(t)}{C_{\pm,e}(t)} = \frac{\Omega(t)}{\Delta(t) \pm \Omega'(t)},\tag{3.34}$$

$$\begin{aligned}\tan\left(\frac{\theta}{2}\right) &= \frac{\sin(\theta)}{1 + \cos(\theta)} \\ \cot\left(\frac{\theta}{2}\right) &= \frac{\sin(\theta)}{1 - \cos(\theta)},\end{aligned}\tag{3.35}$$

eigenstates corresponds to  $\lambda_{\pm}(t)$  is given as

$$|\Psi_+(t)\rangle = \sin(\theta(t)/2)|g\rangle + \cos(\theta(t)/2)|e\rangle\tag{3.36}$$

$$|\Psi_-(t)\rangle = \cos(\theta(t)/2)|g\rangle - \sin(\theta(t)/2)|e\rangle.\tag{3.37}$$

Here,  $\Theta(t)$  is given by the following equation

$$\cos(\theta(t)) = \frac{\Delta(t)}{\Omega'(t)}\tag{3.38}$$

$$\sin(\theta(t)) = \frac{\Omega(t)}{\Omega'(t)}.\tag{3.39}$$

For a linearly chirped pulse with large linear chirp, state evolution becomes slower and adiabatic theorem is valid [37]. In this case, time evolution of the state occurs along the time evolution of the eigenvalue and eigenstate. Fig. 3.1 and 3.2 shows the time evolution of the eigenvalue and eigenstate by a linearly chirped pulse with  $c_2 = 50000\text{fs}^2$ , which results adiabatic inversion of atomic states.

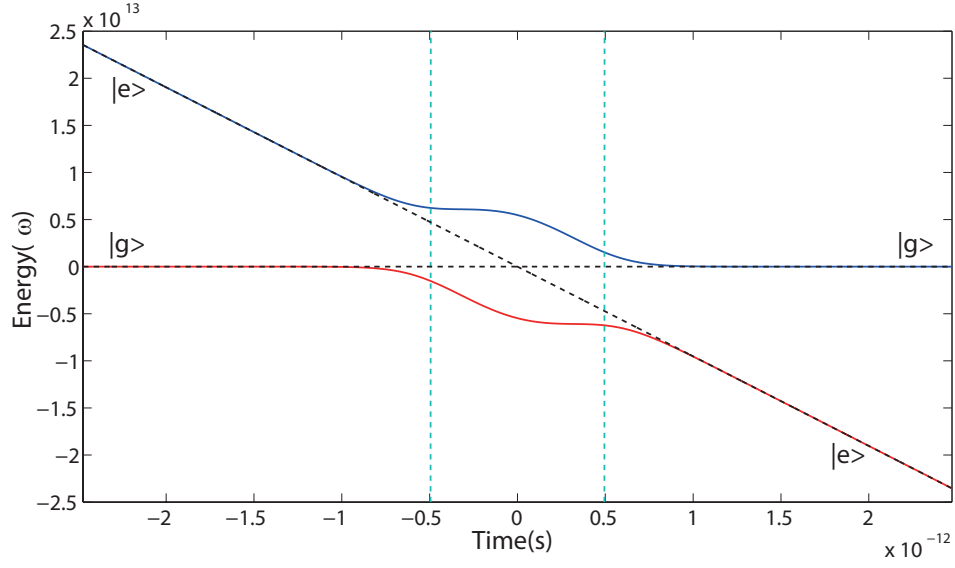


Figure 3.1: Time evolution of eigenstate represented by time dependent change of eigenenergy. A  $50000\text{fs}^2$  linearly chirped pulse with spectral FWHM of  $\sim 7\text{nm}$  and pulse area  $2\pi$  was used for calculation. Blue line represents  $\lambda_+(t)$ , red line represents  $\lambda_-(t)$ , and dotted cyan line is temporal width  $\tau$  of the pulse. Starting from initial state  $|g\rangle$ , an adiabatic time evolution occurs through red line,  $\lambda_-(t)$ , and the corresponding state evolution is  $|g\rangle \rightarrow |e\rangle$ .

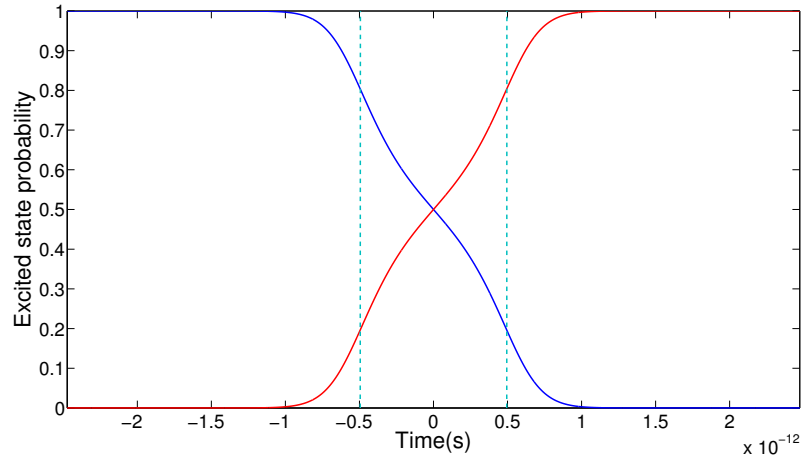


Figure 3.2: State representation of time evolution given in 3.1. Blue line represents  $|\psi_+(t)\rangle$ , red line represents  $|\psi_-(t)\rangle$ , and dotted cyan line shows temporal width  $\tau$  of the pulse. From an initial state  $|g\rangle$ , time evolution of the state is described by the red line,  $|\psi_-(t)\rangle$ , which shows the complete population inversion of atomic states.

## Chapter 4. Magneto optical trap

Magneto optical trap (MOT) is an experimental apparatus for cooling and trapping of neutral atoms. Atoms are cooled down to a temperature lower than mK via laser cooling[cite] and trapped inside a vacuum chamber. Since the temperature of the trapped cold atoms are very low, temperature dependent effects such as Doppler broadening and collisional decoherence are minimized. In addition, spatial confinement of the cold atom ensemble inside a MOT plays an important role on considering spatially inhomogeneous interaction between laser beam and the ensemble [38]. In this chapter, I describe our magneto optical trap system and its characteristics [39].

### 4.1 Vacuum chamber assembly

Usually, the high-vacuum chamber is made of the stainless-steel(SUS) due to its resistance to oxidation which may become a huge source of out-gasing. We selected SUS-316 as chamber material because of its nonmagnetic property, *i.e.*,  $\mu \simeq \mu_0$ , to minimize the disturbance of the trap magnetic field.

Fig. 4.1 show a schematic diagram of our chamber. A main spherical polyhedron chamber has two arms. One arm is connected to the vacuum system, which consists of a ion gauge, an ion pump and a turbo pump. Since base pressure of the turbo pump ( $\sim 10^{-7}$  Torr) is higher than desired pressure of the chamber ( $\sim 10^{-9}$  Torr), we installed a gatevalve between the turbo pump and the arm. Since the gatevalve sustains pressure of the chamber, the turbo can be disassembled from the arm after use. The ion pump keeps high vacuum ( $\sim 10^{-9}$  Torr) of the whole chamber assembly. The other arm is connected to a rubidium source through a gate valve. Our rubidium source is just an ingot of rubidium. If the gate valve is open, vaporized rubidium atoms are diffused into the main chamber.

There are total 18 accesible holes in our chamber, six  $\phi 38$  holes and twelve  $\phi 25$  holes. Two  $\phi 38$  holes are occupied by a MCP assembly and an ion transfer metal plate assembly. And another two  $\phi 38$  holes are conneted to two arms, the atom source and the vacuum system which are explained above. Rest two  $\phi 38$  holes and four  $\phi 25$  holes, which forms an orthogonal axis, are laser quality windows and used for MOT beams. Another two  $\phi 25$  holes are used for femtosecond laser and equipped with broadband anti reflection coated low dispersion windows. The rest four windows are remained for various purpose such as monitoring of the MOT or absorption imaging of the MOT.

### 4.2 Cooling and trapping

For cooling and trapping of the neutral atoms, we need two kinds of forces depend on motion of atoms. First, velocity dependent force for cooling or deacceleration, and second, position dependent for for trapping or spatial confinement. In the MOT, the Doppler shift produces velocity dependence of the transition rate and the Zeeman shift produces position dependence of the transition rate. And momentum kicks given by scattered photons act as forces. Fig. 4.2 and Fig.4.3 show how velocity and position dependence of the transition rate is made. Especially, the cooling process utilizes Doppler shift to make velocity dependence of transition rate is called Doppler cooling [40, 41].

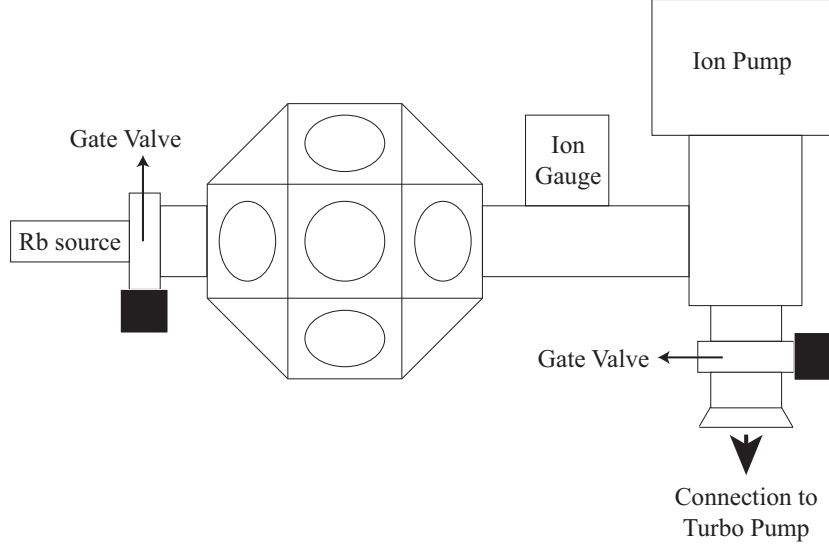


Figure 4.1: Schematic diagram of the chamber assembly.

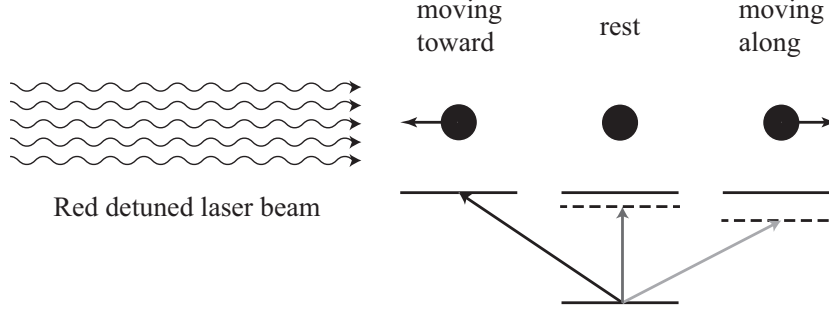


Figure 4.2: Doppler cooling inside a MOT. If an atom is moving toward the laser beam, light seen by the atom is blue shifted. Also, if an atom is moving along with the laser beam, the light is red shifted for the atom. Thus, if the beam is red detuned initially, the atoms moving toward the laser beam feels the light with smaller detuning, which results higher transition probability of the atoms moving toward the beam. Since absorbed photons transfer momentum  $\hbar\vec{k}$  to the atom, deacceleration occurs when atom and photon moving in opposite direction have higher probability of absorption.

### 4.3 MOT transitions of a $^{85}\text{Rb}$ atom

Energy levels of a  $^{85}\text{Rb}$  atom is shown in Fig. 4.4.  $F = 3 \rightarrow F' = 4$  transition is used as cooling transition due to its cycling property, *i.e.*  $F'=4$  only decays into  $F=3$  state. However, small splittings between  $5P_{3/2}$  hyperfine states, which corresponds to the  $\sim 10 \times \Gamma$  maximum, can cause unexpected excitations. Although the transition probability is very small, the excitation like  $F = 3 \rightarrow F' = 3$  can break the cycling transition by decaying into  $F=2$ . Therefore, we also need another laser light which couples  $F=2$  ground state with an appropriate excited state to transfer the atoms to  $F=3$  ground state. We call this transition as “repumping” and we use  $F = 2 \rightarrow F' = 3$  as a repumping transition.

Wavelength of a diode laser can be tuned and locked to a specific hyperfine transition by using real-time spectroscopic signal as a reference. Typically, Doppler free spectroscopic schemes such as saturated absorption spectroscopy (SAS), which can separately observe hyperfine absorption peaks from Doppler broadened profiles, are used for frequency reference. Fig. 4.5 and Fig. 4.6 show measured SAS data of

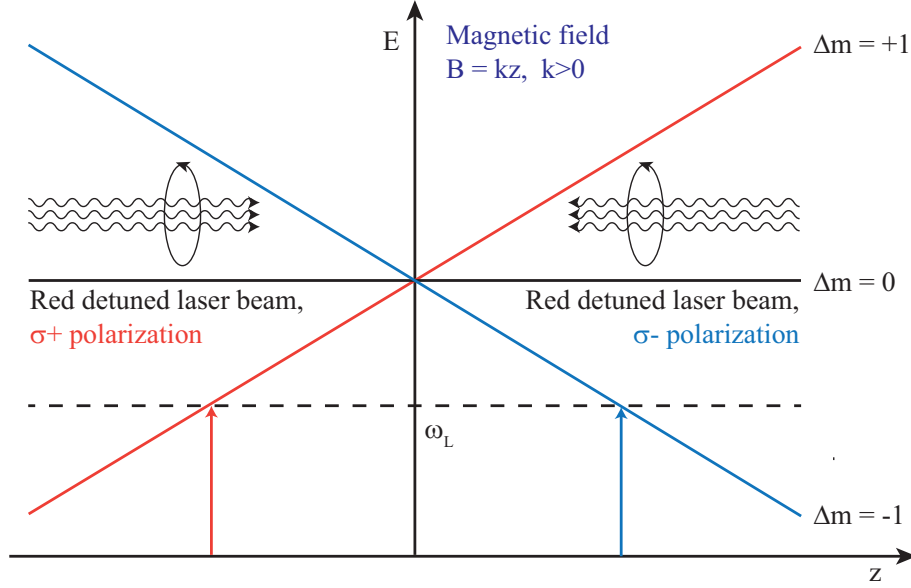


Figure 4.3: Trapping process inside a MOT. To make position dependence of the transition probability, circularly polarized beams and magnetic field are used. Since magnetic field linearly depends on position, Zeeman energy shift induced by the magnetic field is also linear to the position. The  $\sigma^\pm$  circularly polarized beams only induces  $\Delta m = \pm 1$  transition due to the angular momentum conservation. Therefore, as shown in the diagram, transitions giving momentum kicks toward the point of zero magnetic field become more probable, which gather atoms to near zero magnetic field region.

$^{85}\text{Rb}$ .

## 4.4 Magnetic field characteristics

The trench of the chamber is designed for anti-Helmholtz coil to produce magnetic field gradient required for MOT at the center of the chamber. We used 1mm diameter enamelled copper wire as a magnet wire and 290 turned coil is prepared at each trench. The anti-Helmholtz has a electrical resistance of  $\sim 7.5\Omega$ . Magnetic field produced by the anti-Helmholtz coil can be calculated by Biot-Savart's law, which is given as [42]

$$B = \frac{\mu_0}{4\pi} \int_C \frac{Id\vec{l} \times \vec{r}}{|\vec{r}|^3}. \quad (4.1)$$

Calculated radial magnetic field is 2.5G/cm/A and 2.6G/cm/A is measured. For axial magnetic field, 5G/cm/A is expected and 5.2G/cm/A is measured.

## 4.5 Process for High-vacuum

Generally, three pumps are needed to achieve high-vacuum, a rotary pump for initial vacuum pumping, a turbo molecular pump for mid-range vacuum and an ion pump of  $10^{-9}$  Torr or lower attainable pressure. Our turbo molecular pump can be started at atmosphere pressure. The rotation speed of our turbo pump is gradually increased as the pressure becoming lower, to a certain normal operation point. We can reach about the order of  $10^{-7}$  Torr with the turbo pump. At this point, we must bakeout the

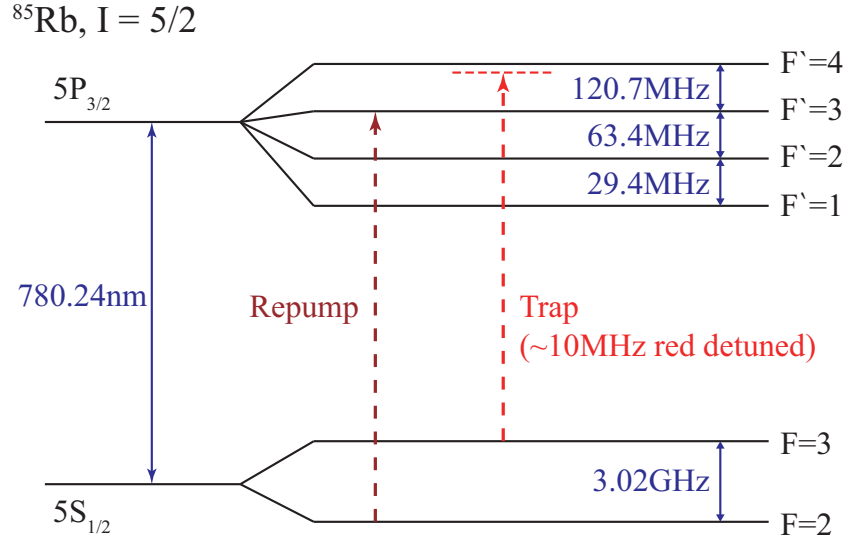


Figure 4.4: Energy level diagram and MOT transitions.

whole chamber to get rid of the out gasing from the metal surface inside of the chamber and also from some unexpected contaminations. Before the bakeout process, bakable temperatures of all parts of the chamber assembly must be carefully considered. There are two ordinary bakeout methods, by using heating tapes and heat dispenser, and by using the oven. A method using an oven needs an oven as large as the whole chamber assembly, therefore getting an oven is a difficulty of the method. However, the whole chamber can be heated evenly inside the oven and the stress from the thermal expansion is minimized. Instead of using an oven, we wound heating tapes at the outside surface of the chamber assembly as even as we can, and several layers of aluminium foils are used to dispense and insulate the heats. The turbo pump should be kept on during the whole bakeout procedure. Available maximum bakeout temperature for our chamber assembly is  $\sim 250^\circ\text{C}$  and the temperature was slowly controlled, about  $20^\circ\text{C}$  change for an hour, to minimize the stress by using variable transformers (sladacs). The real time temperature of the chamber assembly was measured and monitored at three different points. After the temperature reached to  $\sim 200^\circ\text{C}$ , voltages of sladacs were fixed. A progress of the bakeout can be monitored by a vacuum gauge. An ion gauge is ordinarily used for high vacuum as  $< 10^{-8}$  Torr. When the temperature rises, pressure inside the chamber also raises because of the out-gassing and thermal expansion of the gas. Pressure was slowly decreased during bakeout and approached to an equilibrium point after sufficient time of bakeout. If the pressure doesn't changed for a day, the bakeout is enough (It took about a week). The cooling process also must be slowly done. It is important that the turbo pump must be isolated during cooling because an ordinary turbo pump doesn't maintain vacuum higher than order of  $10^{-8}$  Torr. Therefore, if the temperature reaches to operational temperature of the ion-pump, we must close the valve between the chamber and the turbo pump, and turn on the ion pump. Then, because of the thermal contraction of the gas inside the chamber, the pressure is rapidly dropped with temperature.

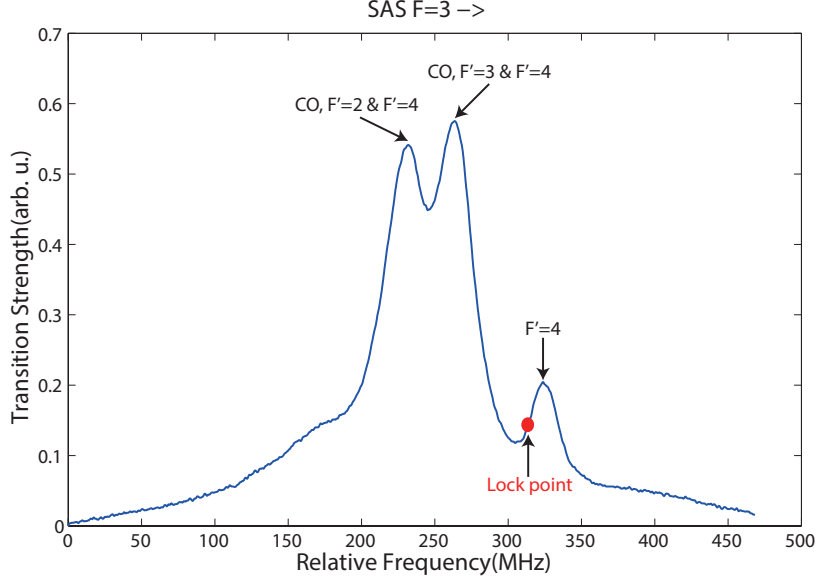


Figure 4.5: SAS signal corresponds to the hyperfine transition of  $F=3 \rightarrow F'$  of  $^{85}\text{Rb}$  atoms. The position indicated by an arrow indicates lock point for MOT cooling and trapping beam, which is 12 MHz ( $\simeq$  natural linewidth) red detuned from  $F=3 \rightarrow F'=4$  transition.

## 4.6 Diode laser system

Our diode laser uses grating feedback to achieve  $<1\text{MHz}$  linewidth for trapping atoms in MOT. The diode laser consist of a laser diode, a grating, a PZT for grating angle control and a thermoelectric cooler for temperature control. A febriferot laser diode (Toptica LD-0780-0200-1) is selected for 780nm D2 line of Rb atoms. A 1800 grooves/mm reflection grating is used for feedback control of wavelength and the efficiency of the grating is about 45% at 780nm. Diffraction from the grating is described by the grating equation as

$$d(\sin\theta_i + \sin\theta_r) = m\lambda, \quad (4.2)$$

where  $d = \frac{1}{1800}$  mm is a groove length,  $\theta_i$  is incident angle of a ray,  $\theta_r$  is the angle of diffracted ray and  $m$  is a integer. Because the 0th order diffraction of the grating is a specular reflection, we uses 1st order diffraction for feedback. For 780 nm radiation,  $\theta_i = \theta_{r,1} = 44.6^\circ$  is a successful feedback condition and corresponding 0th order diffraction is simply  $\theta_{r,0} = -44.6^\circ$ . A PZT is used for an order  $1\mu\text{m}$  displacement and the corresponding angular displacement of the grating is an order of  $10^{-3}$  degree, which gives a frequency tuning range about 10GHz. Fig. 4.9 Temperature is also an important parameter for a laser diode because the resonant mode of a laser diode is very sensity on thermal contraction and expansion of cavity length. A TEC with a PID temperature feedback controller is used for temperature control and stabilization.

## 4.7 Characterization of the MOT

In this section, We discuss about the methods to measure various MOT characteristics and the results.



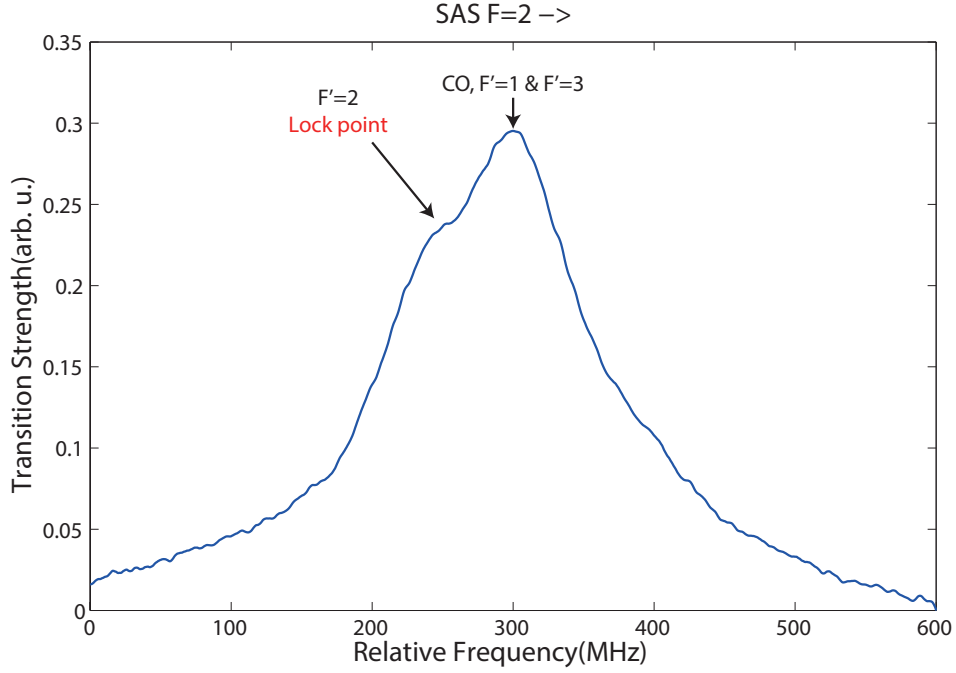


Figure 4.6: SAS signal corresponds to the hyperfine transition of  $F=2 \rightarrow F'$  of  $^{85}\text{Rb}$  atoms. The position indicated by an arrow indicates lock point for MOT repump beam which corresponds to  $F=2 \rightarrow F'=2$  transition peak. Easily resolvable  $F=2 \rightarrow F'=2$  transition was used for repump instead of  $F=2 \rightarrow F'=3$  transition, which gives no difference for cooling and trapping when repump laser power is enough.

We first observed the loading process of the MOT. A loading process of the MOT can be described by the equation

$$\dot{N} = \alpha - \beta N, \quad (4.3)$$

where  $N$  is a number of atoms loaded in a MOT,  $\alpha$  is a loading rate and  $\beta$  is the background collisional loss rate. Here we assumed that the density of the MOT is relatively low and Rb-Rb collisional loss in the MOT, which is described by a term  $\gamma N^2$ , is neglected. Straightforward calculation from Eq. (4.3) gives a loading equation as

$$N = \frac{\alpha}{\beta} + ce^{-\beta t}, \quad (4.4)$$

where  $c$  is defined by a integral constant  $C$  as  $c = -\frac{e^{-\beta C}}{\beta}$ . From Eq. (4.4), a loading time of the MOT is given as  $\frac{1}{\beta}$ .

To observe the loading process, 780nm fluorescence from the atomic cloud was measured as a function of time and measured fluorescence curve was fitted with Eq. (4.4). Fig. 4.10 shows the loading curve of the MOT, with a ground line.

Density of the captured atomic cloud can be calculated by using volume of atomic cloud and number of atoms in cloud. By adjusting magnetic field, we made atomic cloud nearly spherical shape, which make volume calculation easier. Because the chamber hole has a cylindrical shape, we used geometrical method to estimate the radius of atomic cloud. Fig. 5 shows imaged atomic cloud and two circular boundaries of chamber hole at near and far side. According to a geometrical fact, radius of the cylinder at the center of the chamber should be the mean value of two circles. Estimated diameter is 0.13cm and corresponding volume is  $1.53 \times 10^{-3} \text{ cm}^3$ . Here we assumed a spatially gaussian atom cloud. Number of

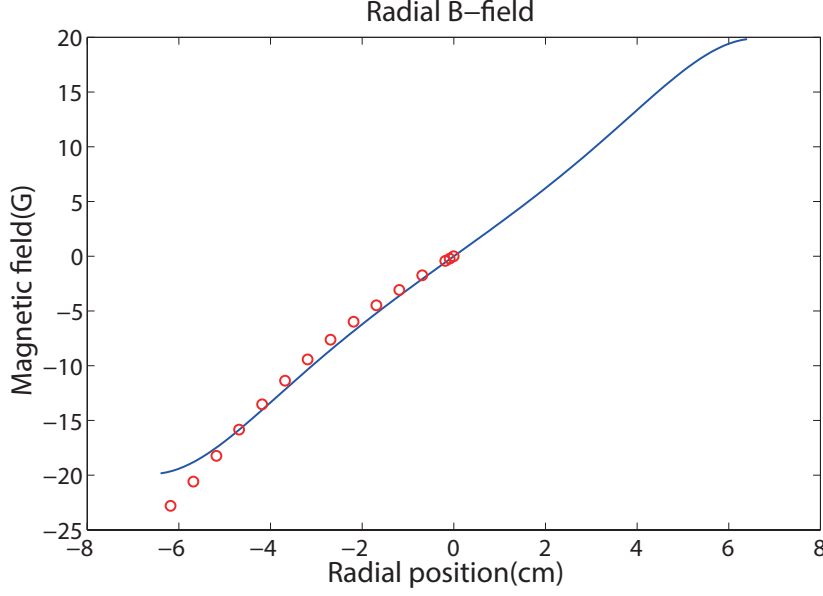


Figure 4.7: Radial magnetic field produced by the anti-Helmholtz coil, theoretical calculation(blue) and measured data(red dots) at 1A of current. Data shows the linearity of the magnetic field at the center of the chamber.

atoms in cloud is calculated from a saturation value of the loading curve. The fraction of the number of atoms in an excited state is given as [41]

$$F = \frac{I/(2I_s)}{1 + I/I_s + (2\Delta/\Gamma_0)^2}, \quad (4.5)$$

where  $I$  is an intensity of the laser beam,  $I_s$  is the saturation intensity for the transition,  $\Delta$  is detuning of the laser beam and  $\Gamma_0$  is a natural linewidth of the transition.  $\Gamma_0 \simeq 6\text{MHz}$  and  $I_s = 1.67\text{mW/cm}^2$  for the  $F = 3 \rightarrow F' = 4$  transition and we used  $\Delta \simeq 12\text{MHz}$  detuned frequency for cooling. Then, number of the atoms can be estimated from the fluorescence as

$$N_{atom} = \frac{P\tau}{Fhf\Omega_A}, \quad (4.6)$$

where  $P$  is measured power of fluorescence in W,  $\tau$  is a life time of the excited state, which is 26ns for the  $F = 3 \rightarrow F' = 4$  transition,  $\Omega_A$  is a solid angle of a photon collecting aperture and  $f$  is a resonant frequency for the transition. In our measuring condition,  $\Omega_A = \frac{\pi r^2}{4\pi R^2}$  where  $R = 10\text{cm}$  is a distance from the atom cloud and the aperture and  $r = 1.25\text{cm}$  is a radius of the aperture. The 0.155V saturation value in the loading curve was measured with 1M $\Omega$  impedance and the estimate current from PMT is  $1.55 \times 10^{-7}\text{A}$ . Also, our PMT has 2500 gain at 700V and 2mA/W sensitivity at 780nm. Therefore, power of measured fluorescence is

$$P = \frac{\text{current}}{\text{gain} \times \text{sensitivity}} = \frac{1.55 \times 10^{-7}}{2500 \times 2} = 31\text{nW}. \quad (4.7)$$

With  $\simeq 3\text{mW}$  radiation at each direction with half inch size,  $I = \frac{3 \times 6}{\pi \times 0.625^2}$  and finally we have  $F = 0.21$ ,  $N = 3.85 \times 10^6$  and the density  $\rho_{atom} = 2.52 \times 10^9$ .

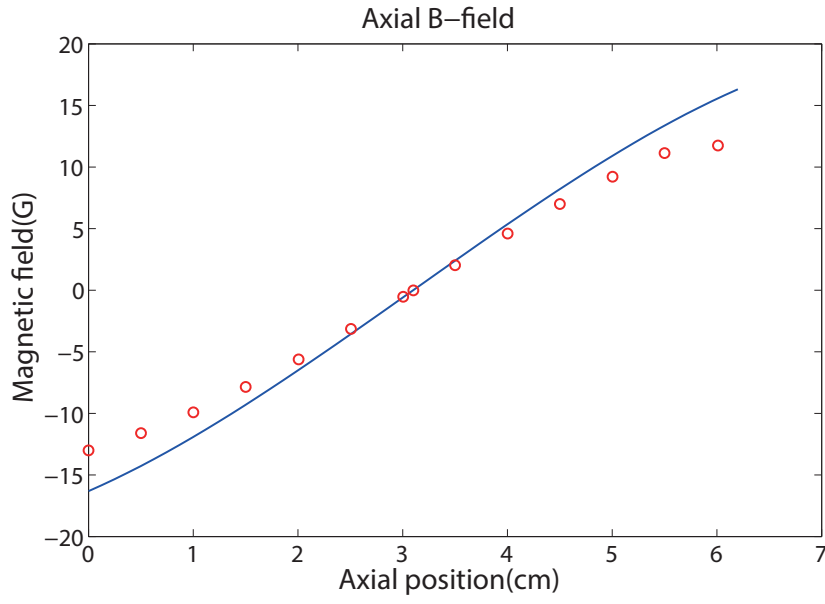


Figure 4.8: Axial magnetic field produced by the anti-Helmholtz coil, theoretical calculation(blue) and measured data(red dots) at 1A of current. Data shows the linearity of the magnetic field at the center of the chamber.

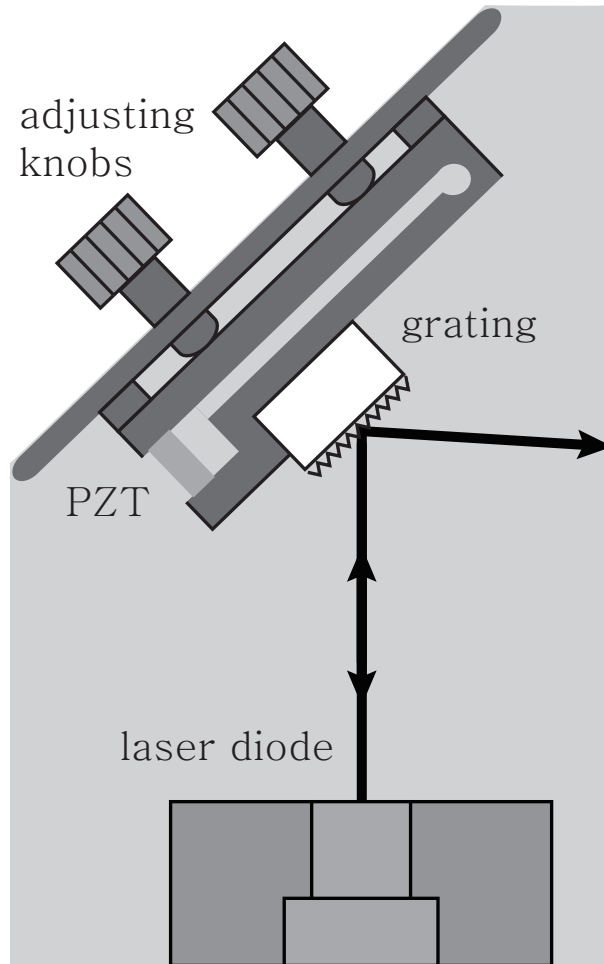


Figure 4.9: Schematic diagram of a grating feedback diode laser.

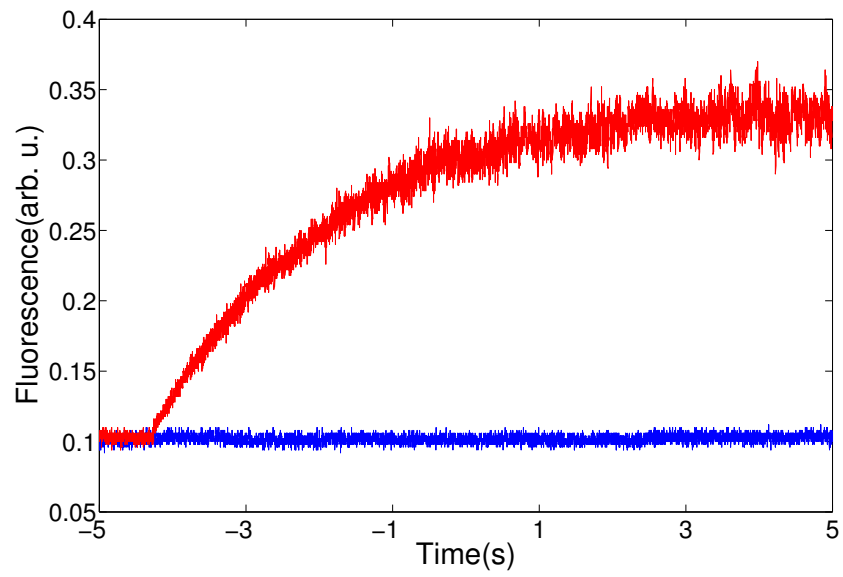


Figure 4.10: Loading curve(red) of the MOT. The ground line(blue) was recorded when all lasers were blocked. Estimated loading time from fitted equation is 2.35(s).

## Chapter 5. Interference control of a four level diamond system

### 5.1 Theoretical consideration of interference control

Two-photon transition probability in weak field regime was already discussed in chapter 3. Based on Eq. (3.23), consider a four-level diamond-configuration system of rubidium. This work has been published in Physical Review A Vol. **88**, pp. 053427 (2013) [43]. For a four-level diamond-configuration system, which comprises a ground state  $|g\rangle$ , two intermediate states  $|a\rangle$  and  $|b\rangle$ , and a final state  $|f\rangle$ , the two-photon transition probability amplitude of  $|g\rangle \rightarrow |f\rangle$  transition is given in weak-field regime by the summation of the two quantum paths via each intermediate state, and written as

$$\begin{aligned} c_{fg} &= -\pi \sum_{i=a,b} \frac{\mu_{fi}\mu_{ig}}{\hbar^2} E(\omega_{ig})E(\omega_{fi}) \\ &+ i \sum_{i=a,b} \frac{\mu_{fi}\mu_{ig}}{\hbar^2} \oint \int_{-\infty}^{\infty} \frac{E(\omega)E(\omega_{fg}-\omega)}{\omega_{ig}-\omega} d\omega. \end{aligned} \quad (5.1)$$

Now we will decompose the net transition probability amplitude into spectral subsets to solve the maximal interference problem for the two-photon transition. First, we denote the resonant and non-resonant two-photon contributions in Eq. (5.1) as

$$\begin{aligned} c_{fg} &= \sum_{i=a,b} c_{fg,i}^r + \sum_{i=a,b} c_{fg,i}^{nr} \\ &= c_{fg}^r + c_{fg}^{nr}. \end{aligned} \quad (5.2)$$

Each resonant term,  $c_{fg,i}^r$ , is solely contributed by the two-photon resonant spectral components of the laser pulse, so the amplitude of  $c_{fg,i}^r$  is not affected by the spectral phase function. However, the non-resonant term,  $c_{fg,i}^{nr}$ , is integrated over the whole spectral range, and, therefore, sensitively responds to the spectral phase function. Let us assume that the laser pulse has constant spectral phase over the whole spectrum. For convinience, we define  $f(\omega)$ , the integrand of the total non-resonant part  $c_{fg}^{nr}$  as

$$f(\omega) = \sum_{i=a,b} \frac{\mu_{fi}\mu_{ig}}{\hbar^2} \frac{E(\omega)E(\omega_{fg}-\omega)}{\omega_{ig}-\omega}. \quad (5.3)$$

An imaginary unit  $i$  is omitted from  $f(\omega)$  because the relative phase between resonant and non-resonant part is not important here. Then,  $f(\omega)$  changes its phase at resonant frequency  $\omega_{ig}$  due to the sign change of the denominator  $\omega_{ig}-\omega$  across the resonance for each pathway,  $|g\rangle \rightarrow |a\rangle \rightarrow |f\rangle$  and  $|g\rangle \rightarrow |b\rangle \rightarrow |f\rangle$ . Also, the interference between the two pathways introduce another critical frequency,  $\omega_c$ , where  $f(\omega)$  changes its sign [see, Fig. 5.1(b)].  $\omega_c$  is located between  $\omega_{ag}$  and  $\omega_{bg}$ , and defined as

$$\omega_c = \frac{k\omega_{ag} + \omega_{bg}}{k+1}, \quad k = \frac{\mu_{fb}\mu_{bg}}{\mu_{fa}\mu_{ag}}. \quad (5.4)$$

Finally, a photon pair make up the two-photon transition satisfies the frequency-sum relation,  $\omega_{fg} = \omega_1 + \omega_2$  as appeared in the numerator of  $f(\omega)$ ,  $E(\omega)E(\omega_{fg}-\omega)$ . Since the spectral components are symmetrically added around  $\omega_{fg}/2$ , the spectral boundaries are also symmetric around  $\omega_{fg}/2$ . So, there are seven spectral boundaries,  $\omega_{ag}$ ,  $\omega_c$ ,  $\omega_{bg}$ ,  $\omega_{fg}/2$ ,  $\omega_{fb}$ ,  $\omega_{fg}-\omega_c$ , and  $\omega_{fa}$  which make eight spectrum blocks divided by the boundaries. Within each block, the phase of  $f(\omega)$  is in-phase if the given spectral block has a constant phase. Shape of the function  $f(\omega)$  is schematically described in Fig. 5.1(b)

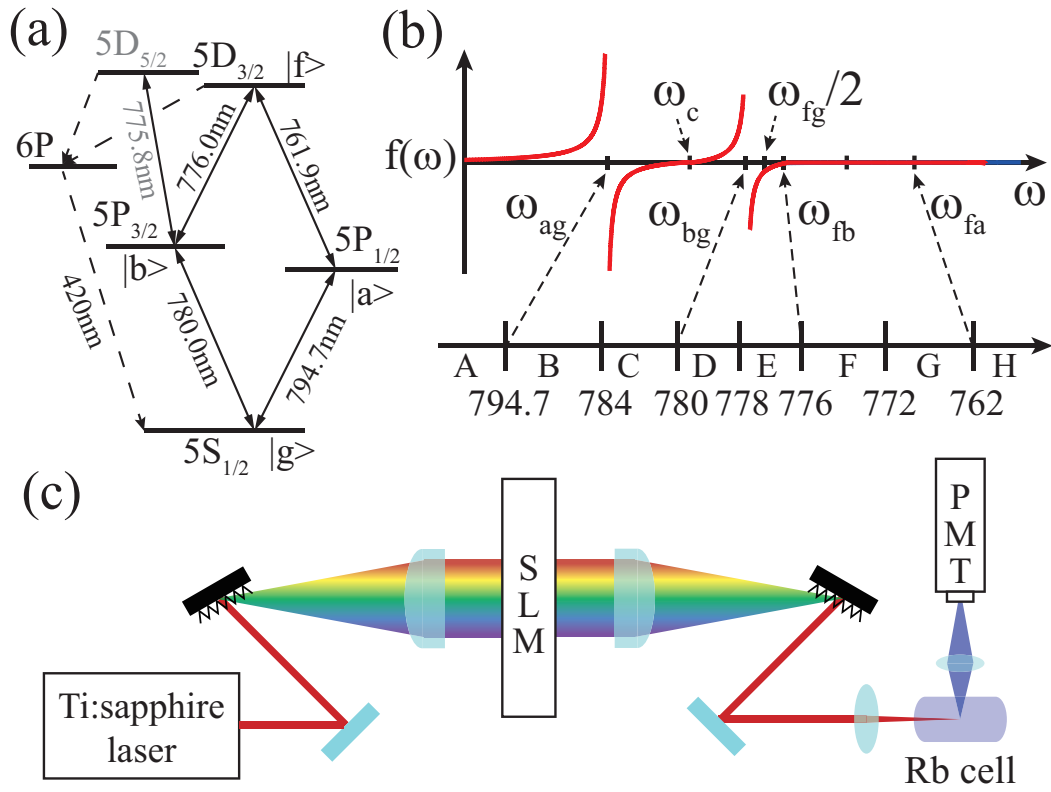


Figure 5.1: (a) Rubidium energy level configuration [44]. Four states,  $5S_{1/2}$ ,  $5P_{1/2}$ ,  $5P_{3/2}$ , and  $5D_{3/2}$ , form a diamond system, while the two-photon transition to  $5D_{5/2}$  (gray) via  $5P_{3/2}$  forms a ladder system. (b) The spectrum blocks and the schematic shape of  $f(\omega)$ , the integrand of  $c_{fg}^{nr}$ . (c) Schematic experimental setup.

To be more specific, we denote the eight spectrum blocks as  $A = (-\infty, \omega_{ag})$ ,  $B = (\omega_{ag}, \omega_c)$ ,  $C = (\omega_c, \omega_{bg})$ ,  $D = (\omega_{bg}, \omega_{fg}/2)$ ,  $E = (\omega_{fg}/2, \omega_{fb})$ ,  $F = (\omega_{fb}, \omega_{fg} - \omega_c)$ ,  $G = (\omega_{fg} - \omega_c, \omega_{fa})$ ,  $H = (\omega_{fa}, \infty)$ , and also define positive-definite functions  $\alpha(\omega)$  and  $\beta(\omega)$  as

$$\begin{aligned}\alpha(\omega) &= \frac{\mu_{fa}\mu_{ag}}{\hbar^2} \frac{|E(\omega)E(\omega_{fg} - \omega)|}{|\omega_{ag} - \omega|} \\ \beta(\omega) &= \frac{\mu_{fb}\mu_{bg}}{\hbar^2} \frac{|E(\omega)E(\omega_{fg} - \omega)|}{|\omega_{bg} - \omega|}.\end{aligned}\quad (5.5)$$

Then, the non-resonant part  $c_{fg}^{nr}$  is given as

$$\begin{aligned}-ic_{fg}^{nr} &= \left[ \int_A \alpha(\omega) d\omega + \int_A \beta(\omega) d\omega - \int_H \alpha(\omega) d\omega - \int_H \beta(\omega) d\omega \right] e^{i\phi_A} e^{i\phi_H} \\ &- \left[ \int_B \alpha(\omega) d\omega - \int_B \beta(\omega) d\omega + \int_G \alpha(\omega) d\omega + \int_G \beta(\omega) d\omega \right] e^{i\phi_B} e^{i\phi_G} \\ &+ \left[ \int_C \beta(\omega) d\omega - \int_C \alpha(\omega) d\omega - \int_F \alpha(\omega) d\omega - \int_F \beta(\omega) d\omega \right] e^{i\phi_C} e^{i\phi_F} \\ &- \left[ \int_D \beta(\omega) d\omega + \int_D \alpha(\omega) d\omega + \int_E \alpha(\omega) d\omega + \int_E \beta(\omega) d\omega \right] e^{i\phi_D} e^{i\phi_E},\end{aligned}\quad (5.6)$$

where  $\phi_i$  denotes the phase of the spectrum block  $i$ . The phase function  $\phi(\omega)$  needs to be uniform in each spectrum block to make the corresponding non-resonant transitions constructively interfere with each other. Note that the first term in each square bracket of Eq. (5.6) indicates the dominant term in each spectrum block since the function  $\alpha(\omega)$  or  $\beta(\omega)$  in Eq. (5.5) shows singular behavior as  $\omega$  approaches to  $\omega_{ag}$  or  $\omega_{bg}$ , respectively.

As easily found in Eq. (5.6), not all the phases  $\{\phi_A, \phi_B, \dots, \phi_H\}$  are independently controlled. So, we use only the four phases of  $A$  to  $D$  and leave the phases of  $E$  to  $H$  to be zero. By substituting the spectrum of the laser pulse, Eq. (5.6) becomes

$$c_{fg}^{nr} = i[c_A e^{i\phi_A} - c_B e^{i\phi_B} + c_C e^{i\phi_C} - c_D e^{i\phi_D}], \quad (5.7)$$

where  $c_j$  for  $j \in \{A, B, C, D\}$  is the sum of integrals in each square bracket of Eq. (5.6), labeled with its dominant spectrum block  $j$ . As all the  $c_j$ 's are positive, the maximal  $c_{fg}^{nr}$  is obtained when  $\phi(\omega)$  satisfies the relations:

$$\phi_A = \phi_C = \phi_B + \pi = \phi_D + \pi. \quad (5.8)$$

## 5.2 Four level approximation of hyperfine states

Transition dipole moments for the hyperfine transitions are calculated using the reduction formulas [45, 46],

$$\langle F, m_F | er_q | F', m_{F'} \rangle = \langle F || er || F' \rangle \langle F, m_F | F', 1, m_{F'}, q \rangle, \quad (5.9)$$

and

$$\begin{aligned}\langle F || er || F' \rangle &= \langle JIF || er || J'I'F' \rangle \\ &= \langle J || er || J' \rangle (-1)^{F'+J+1+I} \begin{Bmatrix} J & J' & 1 \\ F' & F & I \end{Bmatrix},\end{aligned}\quad (5.10)$$

where the nuclear spin  $I = 5/2$  for  $^{85}\text{Rb}$ . We limit our calculation to  $\Delta m_F = 0$  as our experiment uses linearly polarized light. We also assume that there is no external magnetic field, *i.e.*, all Zeeman sub-levels are degenerate. Taking into account the hyperfine splitting, the transition probability amplitude from a ground sub-level  $(F, m_F)$  to a final sub-level  $(F'', m_F)$  is described by

$$\begin{aligned} c_{F''F, m_F} = & -\pi\sqrt{P_{F, m_F}} \sum_{J', F'_{J'}} \frac{\mu_{F''F'_{J'}, m_F} \mu_{F'_{J'}, F, m_F}}{\hbar^2} E(\omega_{F''F'_{J'}}) E(\omega_{F'_{J'}, F}) \\ & + i\sqrt{P_{F, m_F}} \sum_{J', F'_{J'}} \frac{\mu_{F''F'_{J'}, m_F} \mu_{F'_{J'}, F, m_F}}{\hbar^2} \wp \int_{-\infty}^{\infty} \frac{E(\omega) E(\omega_{F''F} - \omega)}{\omega_{F'_{J'}, F} - \omega} d\omega, \end{aligned} \quad (5.11)$$

where  $P_{F, m_F}$  is the statistical probability of the ground sub-levels  $(F, m_F)$  and  $\mu_{F'_{J'}, F, m_F}$  is the transition dipole moment for  $(F, m_F) \rightarrow (F'_{J'}, m_F)$ .  $F'_{J'}$  indicates the hyperfine state  $F'$  of  $J'$  and the  $J'$  summation denotes the sum of all possible two-photon transitions via  $5P_{1/2}$  and  $5P_{3/2}$ . Then, the resulting transition probability from  $5S_{1/2}$  to  $5D_{3/2}$  is given by

$$P_{5S_{1/2} \rightarrow 5D_{3/2}} = \sum_{F'', F, m_F} |c_{F''F, m_F}|^2. \quad (5.12)$$

Since  $c_{F''F, m_F}$  is rapidly diverging near resonance, we can approximate  $F'$  states are degenerated at the region far enough from the  $F'$  hyperfine resonances. Also, The resonant part of the equation also can be expressed by  $\mu_{F''F, m_F, J'}^{(2)}$  because our laser bandwidth is large enough to be considered as a constant intensity over the hyperfine splittings. Then Eq. (5.11) can be simplified as

$$\begin{aligned} c_{F''F, m_F} \approx & -\pi\sqrt{P_{F, m_F}} \sum_{i=a, b} \frac{\mu_{F''F, m_F, J'(i)}^{(2)}}{\hbar^2} E(\omega_{fi}) E(\omega_{ig}) \\ & + i\sqrt{P_{F, m_F}} \sum_{i=a, b} \frac{\mu_{F''F, m_F, J'(i)}^{(2)}}{\hbar^2} \int_{|\omega - \omega_{ig}| \gg 0} \frac{E(\omega) E(\omega_{fg} - \omega)}{\omega_{ig} - \omega} d\omega + S, \end{aligned} \quad (5.13)$$

where  $\mu_{F''F, m_F, J'(i)}^{(2)} = \sum_{F'_{J'(i)}} \mu_{F''F'_{J'(i)}, m_F} \mu_{F'_{J'(i)}, F, m_F}$  for  $i = a, b$  is the sum of two-photon transition dipole moments via all possible  $J'(i)$  states. Here,  $S$  is the spectral integral near the hyperfine resonance region, which remains constant in our experiments because of the limited spectral resolution. Moreover, the numerical calculation finds the fixed ratio between  $\mu_{F''F, m_F, J'(a)}^{(2)}$  and  $\mu_{F''F, m_F, J'(b)}^{(2)}$ , or

$$\frac{\mu_{F''F, m_F, J'=3/2}^{(2)}}{\mu_{F''F, m_F, J'=1/2}^{(2)}} = \frac{\sqrt{3}}{5}, \quad (5.14)$$

of which the result is also independent of  $m_F$ . Therefore, Eq. (5.13) is simply reduced to Eq. (5.1) and, even if hyperfine transitions are considered,  $\omega_c$  in Eq. (5.4) is a constant for all possible  $F$  and  $F''$  pairs.

### 5.3 Experimental details

For the experiment, broadband laser pulses were produced by a Ti:sapphire mode-locked laser oscillator operating at a repetition rate of 80 MHz, and were then spectrally programmed by a spatial light modulator (SLM) [see, Fig. 5.1(c)] [4]. The laser spectrum was centered at 782 nm, close to the two-photon resonant wavelength 778 nm. The SLM with 128 liquid-crystal pixels was located in the Fourier plane of the 4- $f$  geometry zero-dispersion Martinez stretcher [3] with a pair of cylindrical lenses



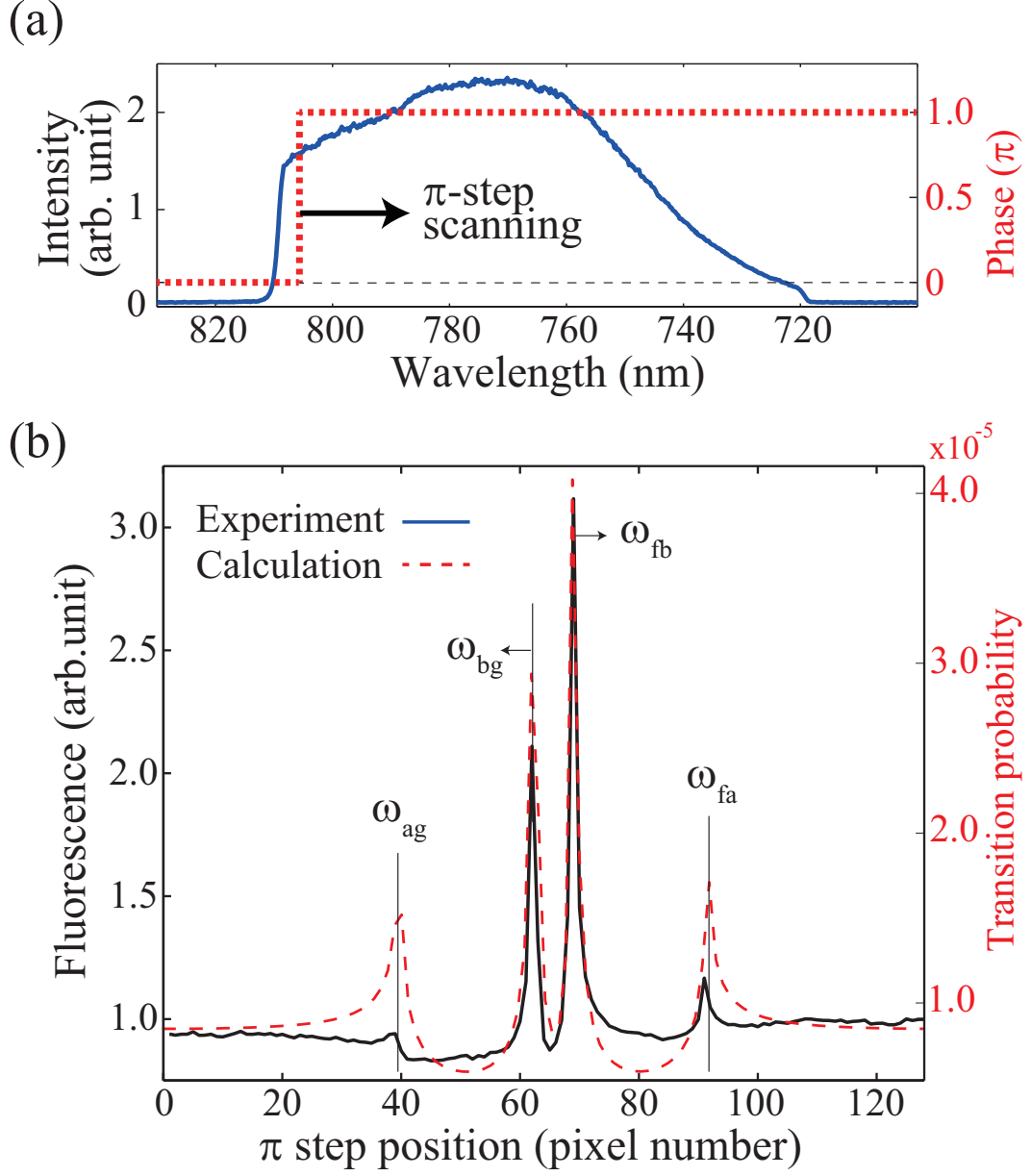


Figure 5.2: Phase-step scanning experiment: (a) Laser spectrum after the SLM (solid line) and phase-step function (dashed line), where the spectral tails were cut for better spectral resolution. (b) The fluorescence signal (solid line) obtained by sweeping the spectral  $\pi$ -phase step, overlapped with the numerical calculation (dashed line). Each peak is labeled with the corresponding resonant frequency.

( $f = 100$  mm) and a pair of gratings (1200/mm). The spectral resolution per pixel for a liquid crystal cell unit  $97\text{ }\mu\text{m}$  wide and with  $3\text{ }\mu\text{m}$  spacing was  $0.5\text{ nm}$ , so the spectral region of each rubidium resonant level was excluded from the phase shaping. The shaped laser pulses, with energy up to  $0.5\text{ nJ}$ , were focused by a lens with a focal length of  $75\text{ mm}$  inside the rubidium vapor cell and the fluorescence signal at  $420\text{ nm}$  via  $6P$  was collected by a photo-multiplier tube. The collected signal did not exclude the two-photon transition to  $5D_{5/2}$  due to the small splitting between the two  $5D$  states. However, the ladder transition to  $5D_{5/2}$ , which is only sensitive to the spectral blocks  $C$  and  $D$ , did not interfere with the diamond transitions to  $5D_{3/2}$  in the perturbative interaction regime. A brief estimation of the pulse area  $\int_{-\infty}^{\infty} \mu A(t)/\hbar dt \sim 0.1$ , where  $A(t)$  is the electric field envelope, calculated with an estimated peak electric field of  $5\text{ MV/m}$  and pulse duration of  $100\text{ fs}$ , confirms that the interaction is in the perturbative regime [32]. To observe the quantum interference between the two excitation passages,  $|g\rangle \rightarrow |a\rangle \rightarrow |f\rangle$  and  $|g\rangle \rightarrow |b\rangle \rightarrow |f\rangle$ , laser pulses with a wide spectral width, about  $45\text{ nm}$  FWHM, were required due to the energy difference ( $15\text{ nm}$ ) between  $|a\rangle$  and  $|b\rangle$ .

### 5.3.1 SLM calibration

Before proceeding to the quantum interference experiment, we performed a phase-step scanning experiment. The laser pulse was spectrally shaped with a phase function  $\phi(\lambda) = \pi\Theta(\lambda - \lambda_s)$ , where  $\Theta(\lambda)$  is the Heaviside step function and  $\lambda_s$  changes through the laser spectrum. As shown in Fig. 5.2(a), the  $\pi$ -phase step was swept to calibrate the spectral position of the SLM pixels. When the  $\pi$ -phase step was located at a resonant frequency, it inverted the base sign of the non-resonant transition probability amplitude in Eq. (5.1) and part of the destructive interference was removed. As a result, at each resonant frequency position, the two-photon transition probability increased and a sharp peak occurred. Figure 5.2(b) shows the experimental results of the phase-step sweeping and identifies the rubidium resonant-level locations in the SLM.

## 5.4 Experimental result

The phase programming of spectrum blocks aims to control the interference between the two passages of rubidium two-photon transition from  $|g\rangle$  to  $|f\rangle$ . Assume that the laser pulse has a constant phase over the spectrum. Then, as described in Eq. (5.7), destructive interference occurs due to the base phase differences in the transition probability amplitude components. We can represent this behavior in a vector diagram, as in Fig. 5.3(a). The phases of the resonant and non-resonant transition probability amplitude components are shown as vectors, with the proper labeling introduced in Eq. (5.7). For convenience, we define

$$c_+^{nr} = c_A e^{i\phi_A} + c_C e^{i\phi_C} \quad \text{and} \quad c_-^{nr} = c_B e^{i\phi_B} + c_D e^{i\phi_D}. \quad (5.15)$$

### 5.4.1 $A+C$ phase rotation

The first experiment considered the interference control of  $A$  and  $C$  with respect to  $B+D$  and the resonant components. The vector diagram in Fig. 5.3(b) shows the schematics of this experiment, where we applied a  $-\pi/2$  to  $2\pi$  phase to  $A$  and  $C$  independently with  $\pi/10$  steps. As the phase increased, the non-resonant components corresponding to  $A$  and  $C$  rotated counter-clockwise and the initial destructive interference was gradually removed. Figure 5.3(d) shows the result. As the phase of  $A$  and  $C$  respectively

reached  $\pi/2$ , the two-photon transition probability increased and a maximum occurred. Note that the maximum point shifted toward  $\pi$  in both the  $\phi_A$  and  $\phi_C$  directions because of the other non-resonant components  $B$  and  $D$ , in which the phase differences with respect to  $A$  and  $C$  are inherently  $\pi$ .

#### 5.4.2 $B+C$ phase rotation

The second experiment used the phases of  $B$  and  $C$  to control the interference with respect to  $A+D$  and the resonant component. The vector diagram in Fig. 5.3(c) describes the concept of this experiment. For this, we applied a  $-\pi/2$  to  $2\pi$  phase to  $B$  and  $C$  independently with  $\pi/10$  steps. Unlike in the previous case of  $A$  and  $C$  control,  $B$  and  $C$  were initially in opposite directions from each other, or with the phase difference of  $\pi$ . Hence, the maximal occurred near  $\phi_B = \pi/2$  and  $\phi_C = 3\pi/2$ , as shown in Fig. 5.3(e).

#### 5.4.3 $AC+BD$ phase rotation

Finally, we applied interference control to all non-resonant components with respect to the resonant component. Direct phase shaping of a resonant frequency component was not available via our SLM due to the limit of the frequency resolution. Therefore, we controlled the non-resonant components to align them with the resonant one. In this experiment,  $\theta$ , the phase of  $A$  and  $C$ , which has an inherent phase of  $\pi/2$ , was simultaneously varied from 0 to  $2\pi$ , while the phase of  $B$  and  $D$ , which has an inherent phase of  $3\pi/2$ , was varied from 0 to  $-2\pi$ , *i.e.*,  $-\theta$ . Then, as described in Fig. 5.4, the non-resonant component  $c_+^{nr}$  rotated counter-clockwise and  $c_-^{nr}$  rotated clockwise. After  $\theta = \pi/2$  rotation, the two non-resonant components and the resonant component were all aligned and the maximal transition probability was achieved. Another local maximum occurred at  $\theta = 3\pi/2$  as a consequence of the anti-parallel resonant and non-resonant components. Figure 5.4 shows the experimental results of the interference control. The data were fitted with the empirical formula

$$c_{fg} = -r + xe^{i(\theta+\pi/2)} + ye^{i(-\theta-\pi/2)}, \quad (5.16)$$

where  $r$  is  $|c_{fg}^r|$ ,  $x$  is  $|c_+^{nr}|$ ,  $y$  is  $|c_-^{nr}|$  and  $\theta$  is the phase applied to the spectrum blocks. The result confirms the phase function solution summarized in Table 5.1, that  $A$  and  $C$  should be  $\pi/2$  phase-shifted from resonant transitions and  $\pi$  phase-shifted from  $B$  and  $D$ .

Table 5.1: Phase function solution of the four-level diamond-configuration system

blocks	$A$	$B$	$C$	$D$
$\omega$	$(-\infty, \omega_{ag})$	$(\omega_{ag}, \omega_c)$	$(\omega_c, \omega_{bg})$	$(\omega_{bg}, \frac{\omega_{fg}}{2})$
$\phi(\omega)$	$\frac{\pi}{2} - \phi_H$	$-\frac{\pi}{2} - \phi_G$	$\frac{\pi}{2} - \phi_F$	$-\frac{\pi}{2} - \phi_E$
blocks	$E$	$F$	$G$	$H$
$\omega$	$(\frac{\omega_{fg}}{2}, \omega_{fb})$	$(\omega_{fb}, \omega_{fg} - \omega_c)$	$(\omega_{fg} - \omega_c, \omega_{fa})$	$(\omega_{fa}, \infty)$
$\phi(\omega)$	$\phi_E$	$\phi_F$	$\phi_G$	$\phi_H$

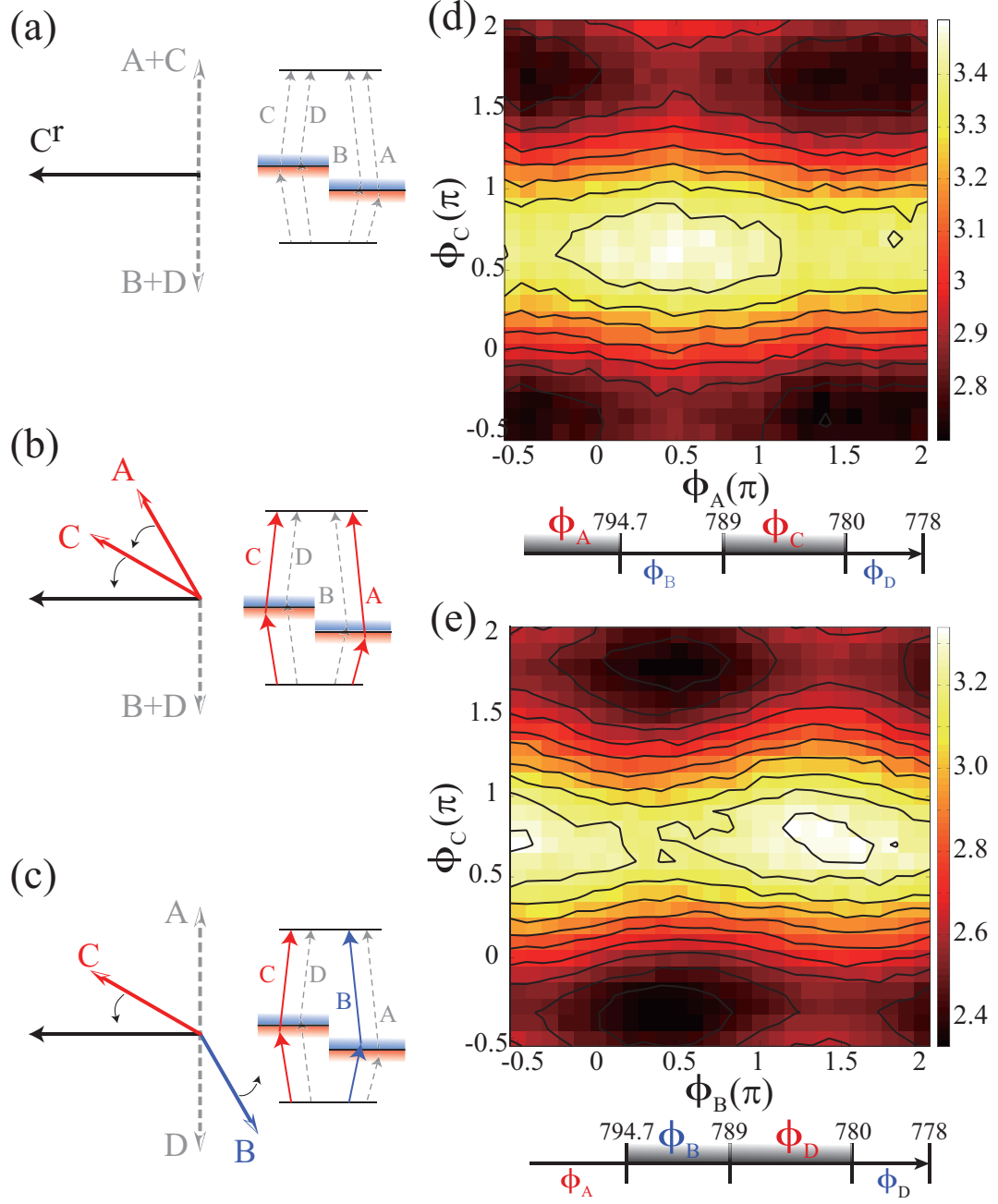


Figure 5.3: (a) Vector diagram for the resonant ( $C^r$ ) and non-resonant ( $A + C$ ,  $B + D$ ) transitions. (b)  $A + C$  phase rotation. (c)  $B + C$  phase rotation. (d) Experimental result for (b), where the phases  $\phi_A$  and  $\phi_C$  are independently varied from  $-\pi/2$  to  $2\pi$ . (e) Experimental result for (c), where  $\phi_B$  and  $\phi_C$  are independently varied from  $-\pi/2$  to  $2\pi$ .

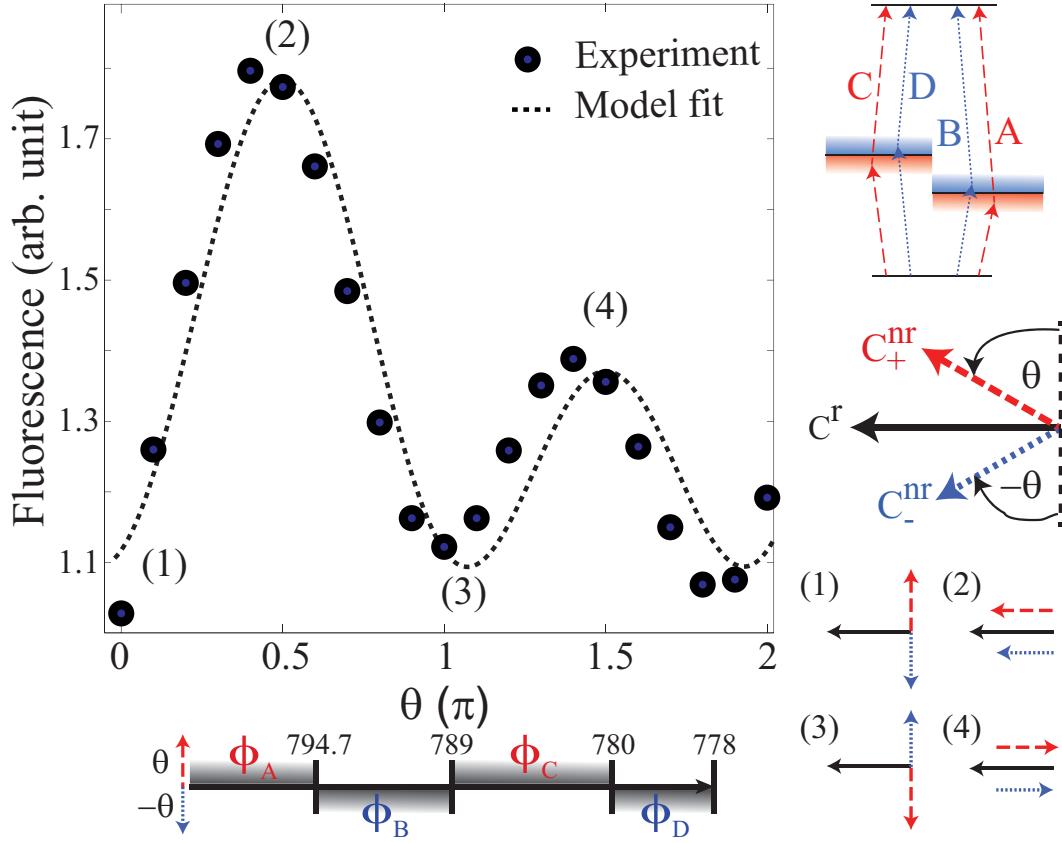


Figure 5.4: Interference control of all non-resonant components with respect to the resonant component. The phases of  $A$  and  $C$  vary from  $0$  to  $2\pi$  while the phases of  $B$  and  $D$  vary simultaneously from  $0$  to  $-2\pi$ . The vector diagrams in the bottom right corner show the orientation of each transition probability amplitude component corresponding to the numbered points in the main plot.

## Chapter 6. Spatially averaged Rabi oscillation

### 6.1 Spatial averaging effect

When a two-state atom interacts with a resonant laser pulse, the dynamics of the excited state probability, which we may refer to as single-atom Rabi oscillation (SARO), is represented by

$$P(\Theta_o) = \sin^2 \frac{\Theta_o}{2}, \quad (6.1)$$

where  $\Theta_o$  is the pulse area defined by  $\Theta_o = \int \mu A(t) dt / \hbar$ , as in Eq. (3.16). Since the pulse area is subject to both the pulse duration and the electric-field envelope, Rabi oscillations of an ultra-short time scale can be implemented by ultrafast optical interaction at a strong-enough laser intensity regime. However, the spatial extent of the laser beam over the laser-atom interaction region inevitably causes spatial average effect that often leads to a complete wide out of the oscillatory behavior. To overcome this problem, homogenizing the spatial profile of laser beams [32, 33] and adapting chirped laser interaction [31] have been considered. This work has been published in Optics Letters Vol. **40**, pp. 510 (2015) [38].

For quantitative analysis of spatially averaged Rabi oscillation, we use the atom ensemble localized in a magneto-optical trap (MOT) and make it interact with ultrafast laser pulses. As a theoretical model to investigate the spatially inhomogeneous interaction, we consider a Gaussian laser beam propagating along  $z$  direction. The pulse area in Eq. (6.1) is then represented in the cylindrical coordinate system as

$$\Theta(r, z) = \Theta_o \frac{w_o}{w(z)} e^{-r^2/w(z)^2} = \Theta_z e^{-r^2/w(z)^2}, \quad (6.2)$$

where  $r = \sqrt{x^2 + y^2}$ ,  $w(z)$  is the beam waist at  $z$ ,  $w_o = w(0)$  is the minimal beam waist,  $\Theta_o$  is the maximal pulse area, and  $\Theta_z = w_o \Theta_o / w(z)$ . When we assume the atom density profile in the MOT is also a Gaussian, *i.e.*,  $\rho(r, z) = \rho_o e^{-(r^2+z^2)/w_a^2}$ , the excitation probability averaged over the entire atom ensemble,  $\langle P(\Theta_o) \rangle = \int P(r, z; \Theta_o) \rho(r, z) dV / \int \rho(r, z) dV$ , which we may call the ensemble-atom Rabi oscillation (EARO), is then given by

$$\begin{aligned} \langle P(\Theta_o) \rangle &= \frac{1}{\sqrt{\pi} w_a^3} \int_{-\infty}^{\infty} dz \int_0^{\infty} dr^2 \sin^2 \frac{\Theta}{2} e^{-(r^2+z^2)/w_a^2} \\ &= \frac{1}{\sqrt{\pi} w_a^3} \int_{-\infty}^{\infty} dz w^2 e^{-z^2/w_a^2} f(\Theta_z), \end{aligned} \quad (6.3)$$

where  $f(\Theta_z) = \int_0^{\Theta_z} (\Theta/\Theta_z)^{w^2/w_a^2} \sin^2(\Theta/2) d\Theta/\Theta$ .

Figure 6.1 shows the numerical calculation of EARO in Eq. (6.3) for various size ratios  $w_o/w_a$ , which is compared with SARO in Eq. (6.1). Note that the all EARO peaks coincide with the SARO curve in Fig. 6.1. The locations of the EARO peaks are found from the condition

$$\frac{d\langle P \rangle}{d\Theta_o} = \frac{1}{\sqrt{\pi} w_a^3} \int_{-\infty}^{\infty} dz w^2 e^{-z^2/w_a^2} f' \frac{d\Theta_z}{d\Theta_o} = 0. \quad (6.4)$$

It is straightforward to show that  $f(\Theta_n) = (w_a/w)^2 \sin^2 \Theta_n/2$  for those  $\Theta_n$ 's that satisfy  $f' = 0$ . Then, Eq. (6.3) at  $\Theta = \Theta_n$  results in

$$\langle P(\Theta_n) \rangle = \sin^2 \frac{\Theta_n}{2}, \quad (6.5)$$

indicating that all EARO peaks are on the SARO curve.

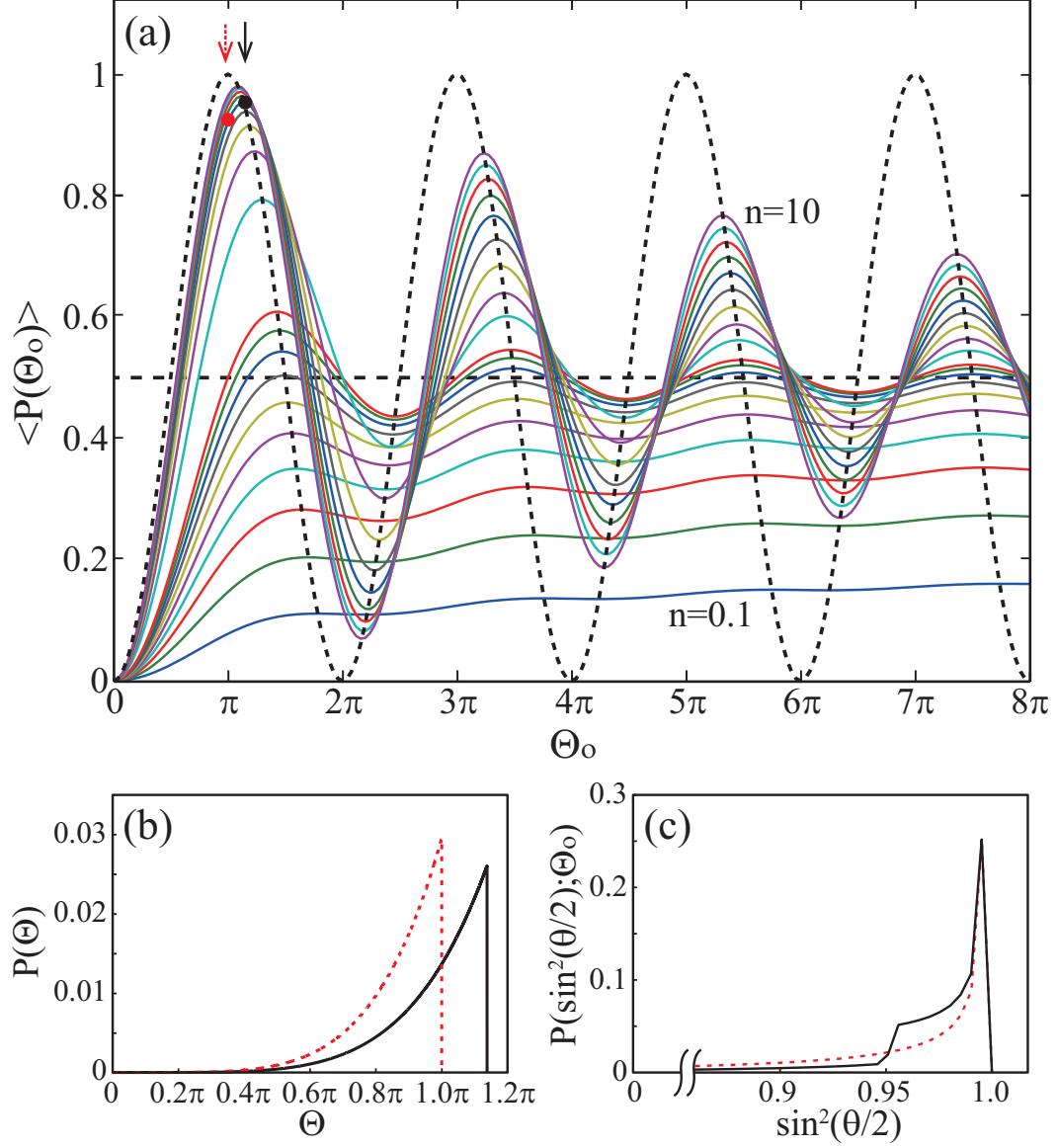


Figure 6.1: (a) Ensemble-atom Rabi oscillation in Eq. (6.3) for various size ratios  $w_o/w_a = \sqrt{n}$  for  $n = 0.1, 0.2, \dots, 0.9$  and  $1, 2, \dots, 10$  (from the bottom to the top). Dotted line represents the single-atom Rabi oscillation in Eq. (6.1). (b,c) Atom probability distributions, at the marked points from the EARO curve for  $w_o/w_a = \sqrt{6}$  in (a), plotted as a function of (b)  $\Theta(r, z; \Theta_o)$ , the pulse area, and (c)  $\theta$ , the polar angle of Bloch vector.

## 6.2 Experimental details

Experiments were performed with atomic rubidium ( $^{85}\text{Rb}$ ) in a MOT as shown in Figs. 6.2(a,b). The  $5S_{1/2}$  and  $5P_{1/2}$  energy states are the ground and excited states, respectively, of the two-level system. The atoms were initially prepared in  $F = 3$  hyperfine level of  $5S_{1/2}$  by the MOT, and a  $\pi$ -polarized laser pulse induced  $\Delta m_F = 0$  transition to  $F' = 2$  and 3 of  $5P_{1/2}$ . The excited and ground states of the combined hyperfine levels formed an effective two-level system, for a ultrafast laser interaction with a moderated laser bandwidth [34, 47]. The atomic transition was driven by ultrafast laser pulses from a Ti:sapphire laser amplifier that produced 250-fs-short pulses at a repetition rate of 1 kHz. When the laser pulses were focused by a lens of focal length  $f = 500$  mm on to the atom ensemble, the pulse energy of up to  $20 \mu\text{J}$  corresponded to the pulse area  $\Theta_o$  up to  $5\pi$ . The laser spectrum was centered at  $\lambda = 794.7$  nm, the resonant wavelength of the  $5S_{1/2} \rightarrow 5P_{1/2}$  transition, and the spectral bandwidth was  $\Delta\lambda = 3$  nm (FWHM). The laser pulse was focused on the atom cloud by a  $f = 500$  mm lens, and the beam size at the atom cloud was adjusted by translating the lens. The detection of the excited atom population was carried out by photo-ionization as shown in Fig. 6.2(c). The probing UV pulse for the photo-ionization was prepared by frequency-doubling of a fraction of the main pulse via second-harmonic generation. The beam size of the probing UV pulse was adjusted by another lens  $f = 300$  mm. Both laser pulses were combined after the lenses by a dichroic mirror and collinearly delivered to the atom cloud. The time difference controlled by a delay stage between the main and probing pulses was fixed to 10 ps, a thousand times smaller than the decay time of the Rb excited state [45].

In each cycle of experiment operating at 2 Hz, atoms were first prepared by turning on 500 ms and off the MOT by mechanical shutters, then immediately interacted with the ultrafast laser pulse, and finally photo-ionized by the probing UV pulse. The excited-state probability was estimated by comparing the fluorescence image counting of the atoms in the MOT and the ion count.

## 6.3 Experimental result

### 6.3.1 Spatially averaged oscillation

Figure 6.3 shows the main experimental result, which clearly exhibits the seemingly decay-like oscillatory behavior. The above analysis on the ensemble-atom laser interaction predicts that such behavior is the spatially averaged Rabi oscillation. The agreement of the numerical calculation by Eq. 6.3 and the experimental result is excellent. It is noted, however, that the discrepancy between them is evident in particular for a high pulse-area exceeding  $\Theta_o = 3\pi$  and also for a higher spatial inhomogeneity in Fig. 6.3(c) for  $w_o/w_a = 1$  than the others. As a cause of the error, we can consider the three-photon ionization directly by the main laser pulse in addition to the one-photo ionization by the probing UV pulse. Such effect is however already systematically taken into account in the data analysis, and the error is estimated less than 2% in the given range of pulse area. The main reason for the discrepancy is the axis mis-alignment of at most  $50\mu\text{m}$  between the laser and the atom cloud, not to mention the imperfect shape of the atom cloud. Our calculation predicts the case in Fig. 3(c) exhibits total 5% of error. It is noted that the ratios of the adjacent peaks are uniquely determined as a function of the size ratio  $w_o/w_a$ , which result can be used as an alternative means to calibrate the excited-state probability of the atom ensemble.





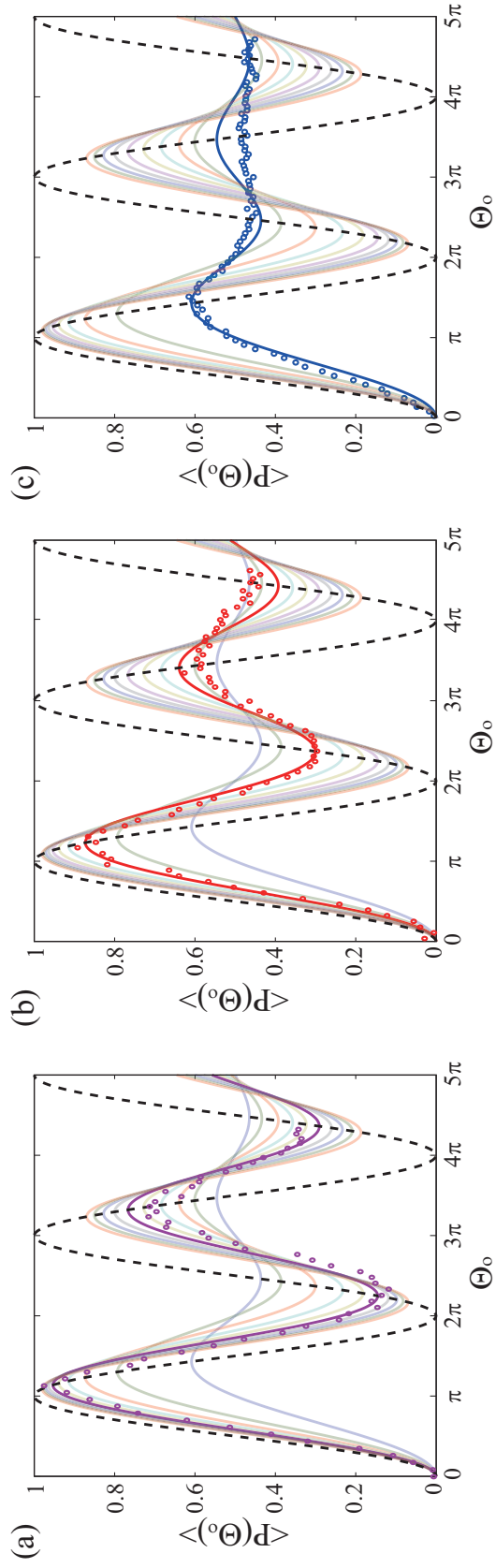


Figure 6.3: Experimental result of ensemble-atom Rabi oscillations: (a) Laser beam width ( $w_o$ ) was 2.5 times of the atom cloud size ( $w_a$ ) or  $w_o = 2.5w_a$ , (b)  $w_o = 1.7w_a$ , and (c)  $w_o = w_a$ . The highlighted line in each figure illustrates the calculation for the closest integer  $(w_o/w_a)^2$  that corresponds to (a)  $(w_o/w_a)^2 = 6$ , (b) 3, and (c) 1, respectively.

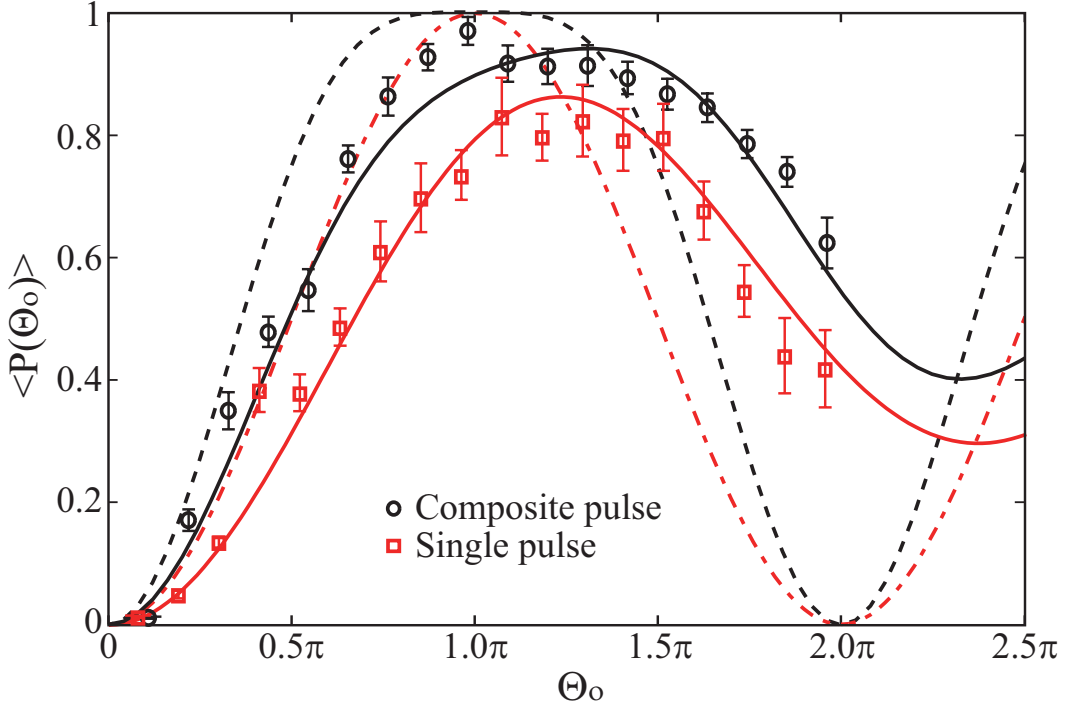


Figure 6.4: Composite-pulse experiment of ensemble-atom Rabi oscillation. For an atom ensemble of the size 1.7 times smaller than a laser beam (*i.e.*,  $w_o = 1.7w_a$ ), the excited-state population for the composite-pulse operation  $R_x(\Theta_o/2)R_y(\Theta_o)R_x(\Theta_o/2)$  was measured and plotted in black circles. In comparison, the single pulse experiment  $R_x(\Theta_o)$  was plotted in red boxes. The solid lines represent the corresponding numerical calculations, when the spatial inhomogeneity of the ensemble-atom experiment is taken into account. The dotted lines are for the spatially homogeneous case (*i.e.*,  $w_o \gg w_a$ ), when the theoretical formulas are given by  $1 - \cos^4(\Theta_o/2)$  (black) for the composite pulse and  $\sin^2(\Theta_o/2)$  (red) for single pulses, respectively.

### 6.3.2 $R_x(\Theta_o/2)R_y(\Theta_o)R_x(\Theta_o/2)$ composite-pulse operation

In the second experiment, we considered a composite pulse to achieve a higher-fidelity Rabi oscillation. We tested the three-pulse composite consisting of two  $\pi/2$  rotations about  $x$ -axis and a  $\pi$  rotation about  $y$ -axis, or  $R_x(\pi/2)R_y(\pi)R_x(\pi/2)$ , which sequence of pulses is well-known in NMR designed to correct errors caused by pulse-area fluctuation [48, 49]. The  $\pi$ -rotation  $R_y(\pi)$  about the  $y$ -axis in the middle corrects the rotation error of the pair of  $\pi/2$  rotations  $R_x(\pi/2)^2$ . In our experiment, we used the three-pulse composite to reduce the spatial inhomogeneity in the ensemble-atom laser interaction. To make the three pulses of the specific amplitude and phase coding, we used an acousto-optic pulse shaper as shown in Fig. 6.2(a), and the accurate control of the pulses was checked by in-situ auto-correlation measurement [50]. Figure 6.4 shows the result of the pulse composite experiment. The first-order corrections of the pulse area  $\Theta_o$  for the  $\pi$  and  $\pi/2$  pulses in an ensemble-atom experiment are respectively given by  $\pi + \alpha$  and  $\pi/2 + \beta$ , where  $\alpha$  and  $\beta$  are determined by the size ratio  $w_o/w_a$ . The experiment was thus performed by a pulse sequence  $R_x(\pi/2 + \alpha)R_y(\pi + \beta)R_x(\pi/2 + \alpha)$ , and the excited-state population is plotted in Fig. 6.4 as a function of  $\Theta_o = \pi + 2\alpha = \pi + \beta$  by fixing  $\beta = 2\alpha$  for the experimental convenience. The result in Fig. 6.4 clearly demonstrates 15% of increase at the first peak of the oscillation by the composite pulse (black circles) compared to the oscillation by the single pulse (red boxes). The

robustness of the composite pulse scheme manifested by the broadened oscillation peak around the  $\pi$  rotation is also clearly observed in Fig. 6.4. It is straight-forward to show that the excited state probability for a single-atom excitation is given by

$$P_e(\Theta_o) = 1 - \cos^4 \frac{\Theta_o}{2} \quad (6.6)$$

for the composite pulse, which results in a broader peak shape around  $\Theta_o = \pi$  than  $\sin^2(\Theta_o/2)$  for a single pulse in Eq. 6.1.

## Chapter 7. Quantum dynamics of a two-state system induced by a chirped zero-area pulse

In this chapter, we consider *chirped zero-area pulses* to study the two-state system dynamics induced by them. To begin with, in the basis of the pulse-area theorem [9], “simple” zero-area pulses make no net transition, leaving the two-state system intact. However, to be more precise, the system does change during the dynamics, although it ends up as a complete population return (CPR) after the completion of the interaction. In that regards, certain manipulation of the initial zero-area pulse could alter the system evolution completely, leading to a significant change in the final transition probability. Even CPI could take place by detuning the zero-area pulse [52, 53], where abrupt phase change makes transitions in adiabatic basis or a crossover between adiabatic evolution and Rabi oscillations. Inspired by these counter-intuitive examples, we proceed further to consider chirping an (on-resonant) zero-area pulse in this chapter. For this, we have conducted laser-atom interaction experiments with intense shaped laser pulses and spatially confined atomic vapor. The results are (1) chirped zero-area pulses could produce both CPI and CPR; (2) the excited-state probability oscillates as a function of the effective pulse-area defined by unshaped pulses; and (3) the given dynamics can be modeled in terms of Ramsey-type three-pulse sequence  $R_x(\pi/2)R_z(\Theta_z)R_x(\pi/2)$  (to be explained below), all of which can be summarized by an interplay between adiabatic evolution and Rabi rotations. This work has been published in Physical Review A Vol. **93**, pp. 023423 (2016) [54].

### 7.1 Theoretical consideration

#### 7.1.1 A chirped zero-area pulse

When the electric field of a laser pulse is defined in time domain as

$$E(t) = \mathcal{E}(t) \cos(\omega_o t + \varphi), \quad (7.1)$$

where  $\mathcal{E}(t)$  and  $\varphi$  are the envelope and phase, respectively, of the electric-field that oscillates with the carrier frequency of  $\omega_o$  set to the Bohr transition frequency of the two-state atom, the pulse area  $\Theta$  is given under the rotating wave approximation by

$$\Theta = \frac{2\mu}{\hbar} \int_{-\infty}^{\infty} E(t) e^{-i\omega_o t} dt = \frac{\sqrt{8\pi}\mu}{\hbar} \tilde{E}(\omega_o), \quad (7.2)$$

where  $\tilde{E}(\omega)$  is the amplitude spectrum of the electric field. In that regards, on-resonance pulses with zero resonant-frequency component, *i.e.*,  $\tilde{E}(\omega_o) = 0$ , are *zero-area pulses* ( $\Theta = 0$ ) defined in frequency domain, which is consistent with the zero-area pulse alternatively defined in time domain [52]. For instance, a Gaussian pulse with a spectral hole around the resonance frequency  $\omega_o$  is a zero-area pulse, which is given by the difference of two Gaussian pulses both frequency-centered at  $\omega_o$ , *i.e.*,

$$\frac{\tilde{E}(\omega)}{E_o} = \exp\left[-\frac{(\omega - \omega_o)^2}{\Delta\omega_1^2}\right] - \exp\left[-\frac{(\omega - \omega_o)^2}{\Delta\omega_2^2}\right]. \quad (7.3)$$

When the spectral width of the first pulse,  $\Delta\omega_1$ , is significantly bigger than that of the second,  $\Delta\omega_2$ , (*i.e.*,  $\Delta\omega_1 \gg \Delta\omega_2$ ), the second pulse (or, to say, the hole pulse) is regarded as a narrow spectral hole of the first pulse (the main pulse).

Let us consider now a *chirped zero-area pulse*, by chirping the above zero-area pulse, which reads

$$\begin{aligned} \frac{\tilde{E}(\omega)}{E_o} &= \left[ \exp \left[ -\frac{(\omega - \omega_o)^2}{\Delta\omega_1^2} \right] - \exp \left[ -\frac{(\omega - \omega_o)^2}{\Delta\omega_2^2} \right] \right] \\ &\times \exp \left[ -\frac{ic_2}{2}(\omega - \omega_o)^2 \right], \end{aligned} \quad (7.4)$$

where the two constituent Gaussian pulses are simultaneously chirped with the frequency chirp  $c_2$ . The electric field in time domain is then given by

$$\begin{aligned} E(t) &= \mathcal{E}_1(t) \cos [(\omega_o + \alpha t)t + \varphi_1] \\ &\quad - \mathcal{E}_2(t) \cos [(\omega_o + \beta t)t + \varphi_2] \\ &\equiv E_1(t) - E_2(t), \end{aligned} \quad (7.5)$$

where the amplitude and the phase for each pulse  $i = 1, 2$  are, respectively,

$$\mathcal{E}_i(t) = \frac{E_o \Delta\omega_i}{\sqrt{2}} \sqrt{\frac{\tau_{o,i}}{\tau_i}} e^{-t^2/\tau_i^2}, \quad (7.6)$$

$$\varphi_i = -\frac{1}{2} \tan^{-1} \frac{2c_2}{\tau_{o,i}^2}, \quad (7.7)$$

with  $\tau_{o,i} = 2/\Delta\omega_i$ , the initial pulse widths, and  $\tau_i = \sqrt{\tau_{o,i}^2 + 4c_2^2/\tau_{o,i}^2}$ , the chirped pulse widths. The chirp parameters are  $\alpha = 2c_2/(\tau_{o,1}^4 + 4c_2^2)$  and  $\beta = 2c_2/(\tau_{o,2}^4 + 4c_2^2)$ , respectively, for the main and hole pulses. Note that, although Eq. (7.5) satisfies  $\Theta = 0$  based on the definition in Eq. (7.2), the conventional pulse area defined in time domain,  $\int_{-\infty}^{\infty} \mu \mathcal{E}_{\text{total}}(t)/\hbar dt$ , for real envelope  $\mathcal{E}_{\text{total}}(t)$  of the total electric field  $E(t) = E_1(t) - E_2(t)$ , is generally non-zero for  $c_2 \neq 0$ .

As to be discussed below, this type of chirped zero-area pulses can induce both CPI and CPR of a two-state system. To understand the nature of the given dynamics, we will transform the two-state system in three steps: first to an interaction basis (to freeze the phase evolution of the bare atomic state), then to an adiabatic basis [55] (to trace the system's state-mixing during the interaction), and finally to another interaction basis (to clear out the remaining fast phase-evolution of the state). After obtaining the model Hamiltonian, we will discuss the resulting state-evolution in terms of Ramsey-like three rotations in the Bloch sphere representation.

### 7.1.2 Schrödinger equation described in the interaction picture of the main pulse

The dynamics of the two-state system interacts with the electric field  $E(t)$ , in Eq. (7.5), is governed by the Schrödinger equation, which reads

$$i\hbar \frac{d}{dt} |\psi(t)\rangle = H(t) |\psi(t)\rangle, \quad (7.8)$$

where  $|\psi(t)\rangle \equiv [a(t), b(t)]^T$  is the column vector with the probability amplitudes  $a(t)$  and  $b(t)$  of the two-states  $|1\rangle$  and  $|2\rangle$  (bare atomic states), respectively, and the Hamiltonian  $H(t)$  is given by

$$H(t) = \frac{\hbar}{2} \begin{bmatrix} -\omega_o & 0 \\ 0 & \omega_o \end{bmatrix} + \mu \begin{bmatrix} 0 & E_1 - E_2 \\ E_1 - E_2 & 0 \end{bmatrix}. \quad (7.9)$$

First, we consider the rotating-wave approximation corresponding to the atom interaction with the main pulse  $E_1(t)$  (only). In the given interaction picture [35] defined by the state transformation

$$|\psi(t)\rangle_I = \exp \left( \frac{i}{\hbar} \int_0^t H_\omega(t') dt' \right) |\psi(t)\rangle \equiv T_\omega |\psi(t)\rangle \quad (7.10)$$

with

$$H_\omega = \frac{\hbar}{2} \begin{bmatrix} -\omega(t) & 0 \\ 0 & \omega(t) \end{bmatrix}, \quad (7.11)$$

where  $\omega(t) = \omega_o + 2\alpha t$  is the (instantaneous) carrier frequency [56] of  $E_1(t)$ , the interaction Hamiltonian  $V_I$  is given by

$$\begin{aligned} V_I &= \frac{\hbar}{2} \begin{bmatrix} -\Delta(t) & \Omega_1(t) \\ \Omega_1(t) & \Delta(t) \end{bmatrix} - \frac{\hbar}{2} \begin{bmatrix} 0 & \Omega_2(t) \\ \Omega_2^*(t) & 0 \end{bmatrix} \\ &\equiv V_{I,1} + V_{I,2}, \end{aligned} \quad (7.12)$$

where  $\Delta(t) = \omega_o - \omega(t) = -2\alpha t$  is the (instantaneous) detuning. The Rabi frequencies of the main and hole pulses are, respectively, given by

$$\Omega_1(t) = \frac{\mu}{\hbar} \mathcal{E}_1(t), \quad (7.13)$$

$$\Omega_2(t) = \frac{\mu}{\hbar} \mathcal{E}_2(t) e^{i[(\beta - \alpha)t^2 + \varphi]}, \quad (7.14)$$

where we define  $\varphi \equiv \varphi_1 - \varphi_2$ , and the time-independent phase  $\varphi_1$  is included in the base vector for the sake of simplicity.

### 7.1.3 Dynamics described in the adiabatic basis of the main pulse

In Eq. (7.12),  $V_{I,1}$ , the first part of the interaction Hamiltonian, varies slowly compared to the second  $V_{I,2}$ , so the system dynamics can be more easily understood in the adiabatic basis [55] of the main pulse. The eigenvalues of  $V_{I,1}$  are given by

$$\frac{\hbar}{2} \lambda_{\pm}(t) = \pm \frac{\hbar}{2} \sqrt{\Omega_1^2(t) + \Delta^2(t)} \quad (7.15)$$

and the corresponding eigenstates are

$$\begin{aligned} |\psi_-(t)\rangle &= \cos \vartheta(t) |0\rangle_I - \sin \vartheta(t) |1\rangle_I, \\ |\psi_+(t)\rangle &= \sin \vartheta(t) |0\rangle_I + \cos \vartheta(t) |1\rangle_I, \end{aligned} \quad (7.16)$$

where  $|0\rangle_I$  and  $|1\rangle_I$  form the eigenbasis in the interaction picture, and the mixing angle  $\vartheta(t)$  is defined by

$$\vartheta(t) = \frac{1}{2} \tan^{-1} \frac{\Omega_1(t)}{\Delta(t)} \quad \text{for } 0 \leq \vartheta(t) \leq \frac{\pi}{2}. \quad (7.17)$$

So, the two-state system can be described in adiabatic basis ( $|\psi_-(t)\rangle, |\psi_+(t)\rangle$ ) with the transformation  $|\psi(t)\rangle_A = R(\vartheta) |\psi(t)\rangle_I$ , where the rotation  $R(\vartheta)$  is defined by

$$R(\vartheta) = \begin{bmatrix} \cos \vartheta(t) & -\sin \vartheta(t) \\ \sin \vartheta(t) & \cos \vartheta(t) \end{bmatrix}. \quad (7.18)$$

Note that each adiabatic base vector,  $|\psi_-(t)\rangle$  or  $|\psi_+(t)\rangle$ , changes from one atomic state to the other, as time evolves from  $t = -\infty$  to  $\infty$ . In other words, when  $c_2 > 0$ ,

$$\begin{aligned} \lim_{t \rightarrow -\infty} |\psi_-(t)\rangle &= |0\rangle_I, & \lim_{t \rightarrow \infty} |\psi_-(t)\rangle &= -|1\rangle_I, \\ \lim_{t \rightarrow -\infty} |\psi_+(t)\rangle &= |1\rangle_I, & \lim_{t \rightarrow \infty} |\psi_+(t)\rangle &= |0\rangle_I, \end{aligned} \quad (7.19)$$

and when  $c_2 < 0$ , the relation is reversed, since the time dependence of  $\Delta$  is opposite.

In the given adiabatic basis, the Schrödinger equation is given by

$$i\hbar \frac{d}{dt} |\psi(t)\rangle_A = \left( RV_I R^{-1} - i\hbar R \dot{R}^{-1} \right) |\psi(t)\rangle_A, \quad (7.20)$$

where the second term in the parenthesis can be ignored, when the evolution by  $\Omega_1(t)$  is adiabatic, *i.e.*,

$$i\hbar R \dot{R}^{-1} = i\hbar \begin{bmatrix} 0 & -\dot{\vartheta} \\ \dot{\vartheta} & 0 \end{bmatrix} \approx 0, \quad (7.21)$$

so the resulting interaction Hamiltonian is given by

$$V_A = \frac{\hbar}{2} \begin{bmatrix} \lambda_- & -\Omega_2 \\ -\Omega_2^* & \lambda_+ \end{bmatrix} + \hbar \Re(\Omega_2) \sin \vartheta \begin{bmatrix} \cos \vartheta & \sin \vartheta \\ \sin \vartheta & -\cos \vartheta \end{bmatrix}, \quad (7.22)$$

where  $\Re(\Omega_2)$  is the real part of  $\Omega_2(t)$ .

#### 7.1.4 Ramsey-type three pulsed interactions

Let us take a closer look at Hamiltonian  $V_A$ . At the extreme times  $|t| \rightarrow \infty$ , it becomes

$$\begin{aligned} V_A &= \frac{\hbar}{2} \begin{bmatrix} -|\Delta(t)| & -\Omega_2(t) \\ -\Omega_2^*(t) & |\Delta(t)| \end{bmatrix} \quad \text{for } t \rightarrow -\infty \\ &= \frac{\hbar}{2} \begin{bmatrix} -|\Delta(t)| & \Omega_2^*(t) \\ \Omega_2(t) & |\Delta(t)| \end{bmatrix} \quad \text{for } t \rightarrow \infty. \end{aligned} \quad (7.23)$$

Note that the phase evolutions of the diagonal terms are opposite with each other. So, it is convenient to remove the phase factor,  $\exp(i \int_0^t |\Delta(t')| dt') = \exp(i|\Delta(t)|t/2)$ , through a transformation to another interaction basis, *i.e.*,

$$|\psi(t)\rangle_F \equiv T_\Delta |\psi(t)\rangle_A, \quad (7.24)$$

where  $T_\Delta = \exp\left(i \int_0^t H_\Delta(t') dt' / \hbar\right)$  with

$$H_\Delta = \frac{\hbar}{2} \begin{bmatrix} -|\Delta(t)| & 0 \\ 0 & |\Delta(t)| \end{bmatrix}. \quad (7.25)$$

The resulting final Hamiltonian becomes

$$V_F = T_\Delta (V_A - H_\Delta) T_\Delta^\dagger = \frac{\hbar}{2} \begin{bmatrix} -\Delta_F(t) & \Omega_F(t) \\ \Omega_F^*(t) & \Delta_F(t) \end{bmatrix}, \quad (7.26)$$

where the effective “detuning”  $\Delta_F$  and “coupling”  $\Omega_F$  are given by

$$\begin{aligned} \Delta_F &= \sqrt{\Omega_1^2(t) + \Delta^2(t) + \Re(\Omega_2) \sin[2\vartheta(t)]} - |\Delta(t)|, \\ \Omega_F &= \{-\cos[2\vartheta(t)] \Re(\Omega_2) - i \Im(\Omega_2)\} e^{-i|\Delta(t)|t/2}, \end{aligned} \quad (7.27)$$

where  $\Im(\Omega_2)$  is the imaginary part of  $\Omega_2(t)$ . The above Hamiltonian leads to the detuned Rabi oscillation [9] after a second rotating-wave approximation. The remaining time-dependence in  $\Omega_F(t)$ , the slowly-varying phase factor  $e^{i\beta t^2}$ , is negligible for the considered chirp values.

Figure 7.1(a) plots the Rabi frequencies of the main pulse,  $\Omega_1(t)$ , the hole,  $|\Omega_2(t)|$ , and the total electric field,  $|\Omega(t)| = |\Omega_1(t) - \Omega_2(t)|$ , of a chirped zero-area pulse that results in a CPR. The numerical values for the given pulse are  $c_2 = 5.1 \times 10^4 \text{ fs}^2$ ,  $\Delta\omega_1 = 1.5 \times 10^{13} \text{ rad/s}$ , and  $\Delta\omega_2 = 1.9 \times 10^{12} \text{ rad/s}$ .



The peak electric field of the main pulse is  $E_o\Delta\omega_1/\sqrt{2} = 2.3 \times 10^8$  V/m, and the dipole moment of atomic rubidium ( $^{85}\text{Rb}$ ) for linearly polarized light is given by  $\mu = 1.46 \times 10^{-29}$  Cm [47, 45]. To examine adiabaticity, we use the adiabaticity function  $f(t) = |\dot{\Omega}(t)\Delta(t) - \Omega(t)\dot{\Delta}(t)|/2[\sqrt{\Omega^2 + \Delta^2}]^3$  [28]. Adiabatic evolution condition is given by  $f(t) \ll 1$ . For linearly chirped pulses, the function  $f(t)$  can be explicitly written as,

$$f_1(t) = \frac{\alpha|\Omega_1(t)|(2t^2/\tau_1^2 + 1)}{[\sqrt{|\Omega_1|^2 + 4\alpha^2 t^2}]^3}, \quad (7.28)$$

$$f_2(t) = \frac{\beta|\Omega_2(t)|(2t^2/\tau_2^2 + 1)}{[\sqrt{|\Omega_2|^2 + 4\beta^2 t^2}]^3}, \quad (7.29)$$

where  $f_1(t)$  and  $f_2(t)$  are the adiabatic functions for the main and the hole pulses, respectively. Note that the pulse width  $\tau_i$  and the chirp parameters  $\alpha$  and  $\beta$  are functions of the bandwidth  $\Delta\omega_i$  as well as of the linear chirp  $c_2$ . With the given parameters in Fig. 7.1, we obtain the adiabatic condition,  $f_1(t) < 0.2$ , for the main pulse with  $E_o\Delta\omega_1/\sqrt{2} > 1.2 \times 10^8$  V/m and  $c_2 > 2 \times 10^4$  fs<sup>2</sup>, which ensures the adiabatic evolution by the main pulse. However, we obtain  $f_2(t) > 1.2$ , so the hole pulse induces simple Rabi rotations, even up to the region  $c_2 \simeq 1 \times 10^5$  fs<sup>2</sup>.

Figure 7.1(b) shows the time-evolution of the transition probability in the adiabatic basis compared with the transition in the bare basis. The overall transition is a CPI in the adiabatic basis, or a CPR in the bare basis. We plot, in Fig. 7.1(c), the polar angle,  $\theta_{\text{rot}}(t)$ , of the rotational axis on the Bloch sphere in the adiabatic basis, defined by

$$\theta_{\text{rot}}(t) = \tan^{-1} \frac{|\Omega_F(t)|}{|\Delta_F(t)|}. \quad (7.30)$$

When  $\theta_{\text{rot}} \approx 0$ , the given rotation becomes approximately a phase evolution (about the  $z$  axis); however, when  $\theta_{\text{rot}} = 0.5\pi$ , it becomes a Rabi rotation. Therefore, the three plateaus in Fig. 7.1(c) suggest that there are three distinct regions: In the two tail regions ( $t < -\tau_1$  and  $t > \tau_1$ ), the coupling  $|\Omega_F|$  is dominant compared to the detuning  $|\Delta_F|$ , so a Rabi rotation is expected. Figure 1(b) clearly shows that, in the both tail regions, Rabi rotations of  $\pi/2$  (starting from the transition probability zero to 0.5, and from 0.5 to 1, respectively) occur in the adiabatic basis. However, in the central region ( $-\tau_1 < t < \tau_1$ ), the detuning  $|\Delta_F|$  is large, causing approximately a phase evolution of the system.

### $|\Delta(t)| \gg \Omega_1(t)$ (the tail regions)

In the tail regions ( $t < -\tau_1$  and  $t > \tau_1$ ), the detuning  $\Delta(t)$  greatly exceeds the main-pulse interaction  $\Omega_1(t)$ , *i.e.*,  $|\Delta(t)| \gg \Omega_1(t)$ . So, we get  $\Delta_F \rightarrow 0$ , and  $\Omega_F \rightarrow -|\Omega_2|e^{i\varphi}$  (for  $t < \tau_1$ ) or  $|\Omega_2|e^{-i\varphi}$  (for  $t > \tau_1$ ). Given that, the Hamiltonian in Eq. (7.26) is approximated, when the slowly varying phase  $e^{i\beta t^2}$  in  $\Omega_2$  is neglected, as

$$\begin{aligned} V_F &\approx \frac{\hbar}{2} \begin{bmatrix} 0 & |\Omega_2(t)|e^{i(\pi+\varphi)} \\ |\Omega_2(t)|e^{-i(\varphi+\pi)} & 0 \end{bmatrix} \text{ for } t < -\tau_1 \\ &\approx \frac{\hbar}{2} \begin{bmatrix} 0 & |\Omega_2(t)|e^{-i\varphi} \\ |\Omega_2(t)|e^{i\varphi} & 0 \end{bmatrix} \text{ for } t > \tau_1, \end{aligned} \quad (7.31)$$

which means that the dynamics in the tail regions are rotations on the Bloch-sphere surface, represented by  $R_{\pi+\varphi}(\Theta_2^-)$  and  $R_{-\varphi}(\Theta_2^+)$ , respectively, for  $t < \tau_1$  and  $t > \tau_1$ . The rotation axes are on the  $xy$  plane, of which the directions are defined by azimuthal angles  $\phi = \pi + \varphi$  and  $\phi = -\varphi$ , respectively. The rotation angles are given by

$$\Theta_2^- = \int_{-\infty}^{-\tau_1} |\Omega_2(t)|dt \quad \text{and} \quad \Theta_2^+ = \int_{\tau_1}^{\infty} |\Omega_2(t)|dt, \quad (7.32)$$

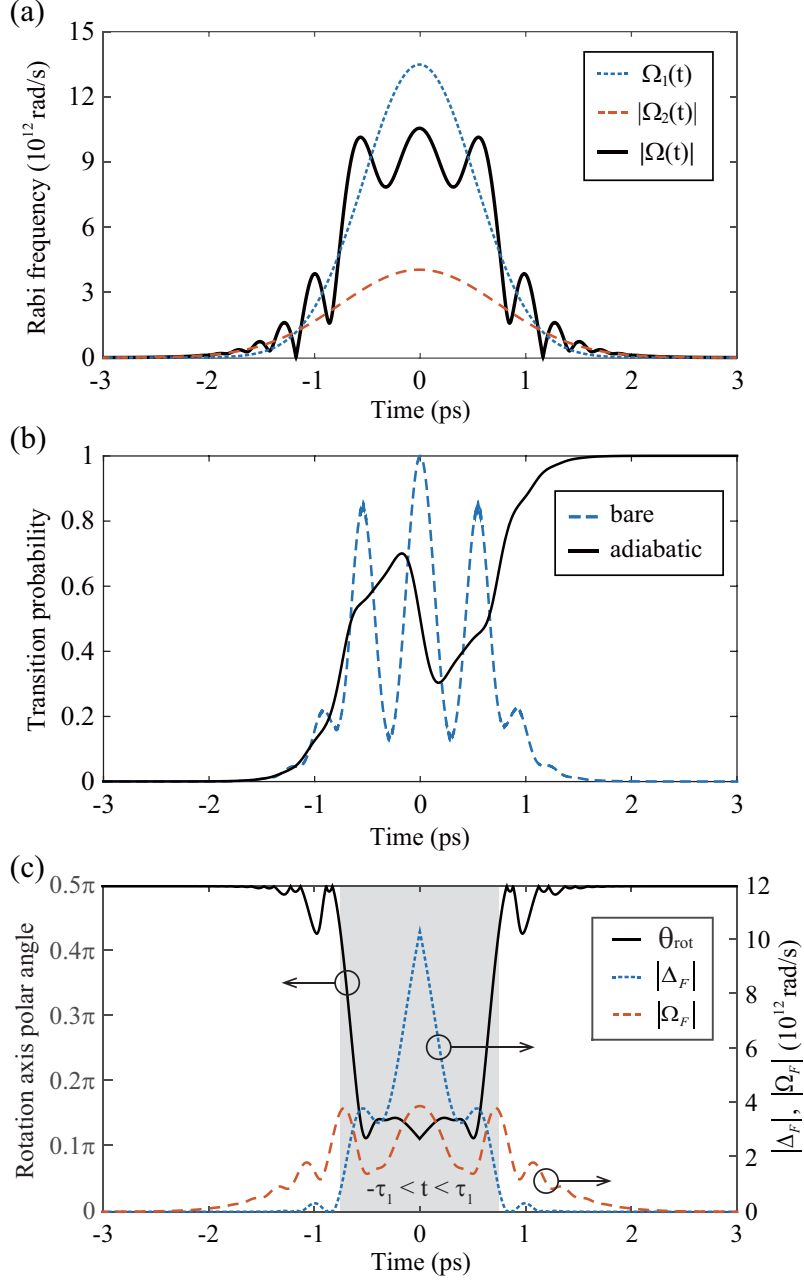


Figure 7.1: (a) The Rabi frequencies  $\Omega_1(t)$  (dotted line) for the main pulse,  $|\Omega_2(t)|$  (dashed line) for the hole, and  $|\Omega(t)|$  (solid line) for the total electric field. (b) The time evolution of the transition probabilities in bare atom and adiabatic bases. (c) The transience of the polar angle  $\theta_{\text{rot}}(t)$  (solid line) for the rotational axis of the Bloch vector in the adiabatic basis compared with  $|\Delta_F(t)|$  (dotted line) and  $|\Omega_F(t)|$  (dashed line). The calculation parameters chosen at a CPR are given in the text.

as a function of the hole pulse  $E_2(t)$ , and  $\Theta_2^+ = \Theta_2^-$  due to the symmetry.

$|\Delta(t)| \ll \Omega_1(t)$  (**the central region**)

In the central time region ( $-\tau_1 < t < \tau_1$ ), the main pulse  $E_1(t)$  plays an important role. To understand the dynamics in this region, we consider an extreme approximation under the conditions  $\Omega_1(t) \gg \Delta(t)$  and  $\Omega_1(t) \gg |\Omega_2(t)|$ . (Note that the case depicted in Fig. 1 is different from this extreme case.) Then, we get  $\Delta_F \approx \Omega_1(t) - |\Delta(t)|$ , which leads to

$$V_F \approx \frac{\hbar}{2} \begin{bmatrix} -\Omega_1(t) + |\Delta(t)| & 0 \\ 0 & \Omega_1(t) - |\Delta(t)| \end{bmatrix}. \quad (7.33)$$

The resulting two-state dynamics is the rotation about the  $z$ -axis, or  $R_z(\Theta_1)$ , by an angle

$$\Theta_1 = \int_{-\tau_1}^{\tau_1} (\Omega_1(t) - |\Delta(t)|) dt \quad (7.34)$$

defined by the main pulse  $E_1(t)$ .

As a result, the overall dynamics of the two-state system by the chirped zero-area pulse (in the transformed adiabatic basis) can be summarized as following:

$$R_{-\varphi}(\Theta_2^+) R_z(\Theta_1) R_{\pi+\varphi}(\Theta_2^-). \quad (7.35)$$

This manifestation of the three-step interaction is a reminiscence of the Ramsey rotation often described by  $R_x(\pi/2) R_z(\Theta_z) R_x(\pi/2)$ , from which the difference is to be discussed.

Note that the necessary condition required (in our consideration) for Ramsey-type three pulse sequence (First Rabi + Second adiabatic evolution + Third Rabi) modeling is in fact the contrast in the spectral width between the main and hole pulses. When the spectral width of the main pulse is large enough, chirping makes the main pulse satisfy the adiabatic condition, while the same amount of chirp makes the spectrally-narrow hole pulse remain as a Rabi-inducing pulse. Therefore, pulses of smooth envelope shapes other than Gaussian, when they have the spectral hole and the chirp, could be approximated to a Ramsey-type three pulse sequence. Also, the three-pulse Ramsey sequence model captures the population dynamics of the system when it is initially in the ground state, *i.e.*, it is shown to be applicable for population dynamics with such an initial state.

## 7.2 Calculation results

Figure 7.2 presents the numerical simulation for the two-state system dynamics induced by the chirped zero-area pulses. For the numerical calculation, the Schrödinger equation in Eq. (7.20) is used with  $\Delta\omega_1 = 1.5 \times 10^{13}$  rad/s and  $\Delta\omega_2 = 1.9 \times 10^{12}$  rad/s. In Fig. 7.2(a), the probability of the transition to the excited state in bare atomic basis is shown as a function of  $\Theta_{\text{Rabi}}$  and  $c_2$ , where  $\Theta_{\text{Rabi}}$  denotes the effective Rabi rotation phase for the main pulse with zero chirp, defined by

$$\Theta_{\text{Rabi}} = \frac{\mu}{\hbar} \int_{-\infty}^{\infty} \mathcal{E}_1(t; c_2 = 0) dt. \quad (7.36)$$

Note that  $\Theta_{\text{Rabi}}$  was varied by changing  $E_o$ , the electric field amplitude, in experiment and calculation.

We can identify several CPR and CPI regions in Fig. 7.2: The CPR regions appear as localized dark spots, besides the wide dark region in low pulse energies; and the CPI regions are bright strips. To

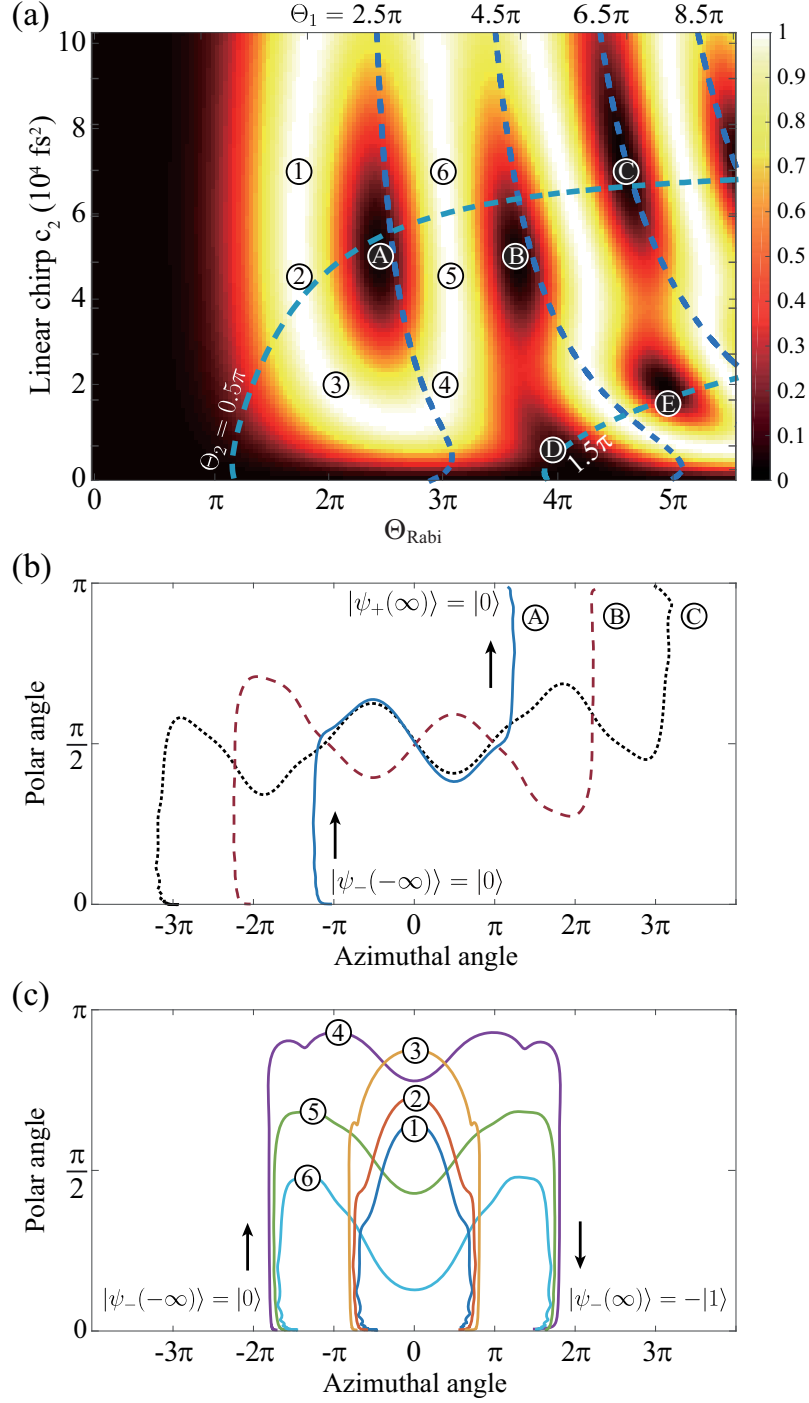


Figure 7.2: (a) Numerical calculation of the transition probability in the atomic basis is plotted as a function of  $\Theta_{\text{Rabi}}$ , the unshaped-pulse Rabi phase, and  $c_2$ , the frequency chirp. Localized CPR regions appear as spots around  $\textcircled{A}$ ,  $\textcircled{B}$ ,  $\dots$ ,  $\textcircled{E}$ ; and CPI regions as strips, e.g., along  $\textcircled{1}$ - $\textcircled{6}$ . The dotted lines indicate contours for the estimated rotation angles  $\Theta_1$  and  $\Theta_2$  defined by Eqs. (7.32) and (7.34). (b) and (c) Trajectories of CPR and CPI represented in the adiabatic basis for chosen points in (a), respectively.

understand the dynamics, we select a few characteristic points in Fig. 7.2(a) and trace their quantum trajectories in adiabatic basis. In Figs. 7.2(b,c), the trajectories are plotted on the  $(\theta, \phi)$  surface of the Bloch sphere (defined in adiabatic basis), where  $\theta$  and  $\phi$  denote the polar and azimuthal angles, respectively, of the Bloch vector. At the CPR points, marked by ①, ②, and ③, each trajectory starts from  $\theta = 0$  and ends at  $\theta = \pi$ , as shown in Fig. 7.2(b). Likewise, at the CPI points, marked by ④, ⑤,  $\dots$ , and ⑥, each trajectory starts from  $\theta = 0$  and ends at  $\theta = 0$ , as shown in Fig. 7.2(c). Note that CPR in bare atomic basis,  $|0\rangle \rightarrow |0\rangle$ , is CPI in adiabatic basis,  $|\psi_-(-\infty)\rangle \rightarrow |\psi_+(\infty)\rangle$ , and CPI in bare atomic basis,  $|0\rangle \rightarrow -|1\rangle$ , is CPR in adiabatic basis,  $|\psi_-(-\infty)\rangle \rightarrow |\psi_-(\infty)\rangle$ .

In particular, each CPR trajectory (CPI in adiabatic basis) in Fig. 7.2(b) consists of three distinctive rotations: a rotation of  $\pi/2$  about a rotation axis in the  $xy$ -plane, a wobbling rotation about the  $z$ -axis, and again a  $\pi/2$  rotation about another axis in the  $xy$ -plane. Note that the azimuthal rotation angles for the second wobbling rotations for the ①, ②, ③ trajectories are about  $2\pi$ ,  $4\pi$ , and  $6\pi$ , respectively. The CPR trajectories are therefore represented in accordance with Eq. (7.35) by

$$R_{-\varphi}(\pi/2)R_z(2n\pi + \gamma)R_{\pi+\varphi}(\pi/2), \quad (7.37)$$

where  $n$  is a positive integer. It is noted that  $\gamma = -\varphi - (\pi + \varphi) = \pi - 2\varphi$  compensates the angle difference between the first and third rotation axes, explaining the deviation of the azimuthal rotation angle from  $2n\pi$ . Here, from Eqs. (7.7) and (7.14),  $\varphi$  is given by  $\varphi = \varphi_1 - \varphi_2 = [\tan^{-1}(2c_2/\tau_{0,1}^2) - \tan^{-1}(2c_2/\tau_{0,2}^2)]/2$ . Since  $\Delta\omega_1 > \Delta\omega_2$ ,  $\gamma$  varies from  $\pi$  to  $\sim\pi/2$ , while  $c_2$  varies from 0 fs<sup>2</sup> to 100000 fs<sup>2</sup>, and  $\gamma \simeq 0.6\pi$  at ①, ②, and ③. Similarly, the trajectories for ④ and ⑤ (not shown) can be approximately represented by  $R_{-\varphi}(3\pi/2)R_z(2\pi + \gamma)R_{\pi+\varphi}(3\pi/2)$  and  $R_{-\varphi}(3\pi/2)R_z(4\pi + \gamma)R_{\pi+\varphi}(3\pi/2)$ , respectively.

The actual trajectories in Fig. 7.2(b) are slightly deviated from the approximated model in Eq. (7.35). It can be explained that, in the central region, the rotation axis is not perfectly aligned with the  $z$ -axis, causing the wobbling of the  $z$ -rotation. As a result, CPRs do not occur at exact  $\Theta_2 = n\pi + \pi/2$ . Also, in the tail regions, the mixing angle  $\vartheta(t)$  does not converge to 0 (for  $t < -\tau_1$ ) or  $\pi/2$  (for  $t > \tau_1$ ) during the evolution, and gives  $\cos[2\vartheta(t)] = 1 - \delta$  (for  $t < -\tau_1$ ) and  $\cos[2\vartheta(t)] = -1 + \delta$  (for  $t > \tau_1$ ) in Eq. (7.27), where  $\delta > 0$  is a small deviation. Since the azimuthal angle of a rotation axis is given by  $\arg[\Omega_F(t)]$ , the actual azimuthal angle difference between the two rotation axes becomes smaller than the model. Thus, as shown in Fig. 7.2(a), the CPRs (①, ②, and ③) occur near  $\Theta_1 = 2n\pi + 0.5\pi$ , rather than  $\Theta_1 = 2n\pi + \gamma (\simeq 2n\pi + 0.6\pi)$ .

The intermediate region between the tail regions and the central region, appearing in Figs. 7.2(b,c) around the end the vertical evolution and beginning of the wobbling  $z$ -rotation, is short in time compared to other regions (the ratio is roughly 0.2 compared to the central region). Also, the change of the rotation axis is much faster (roughly 5 times faster) than the rotation. Therefore, as shown in Figs. 7.2(b,c), there are no significant influence to the dynamics in the intermediate region.

### 7.3 Experimental setup

The experimental investigation of the chirped-zero area-pulse interaction of the two-state system is performed with shaped intense laser pulses and cold atomic vapor. The experimental setup is shown in Fig. 7.3. Femto-second laser pulses were first produced from a home-made Ti:sapphire laser oscillator with 80 MHz repetition rate, and amplified about  $5 \times 10^5$  times by a home-made Ti:sapphire multi-pass amplifier operating at 1 kHz repetition rate. The wavelength of the pulses was centered at  $\lambda_o = 794.7$  nm, resonant to the atomic rubidium (<sup>85</sup>Rb)  $5S_{1/2} \rightarrow 5P_{1/2}$  transition. The two states of the quantum

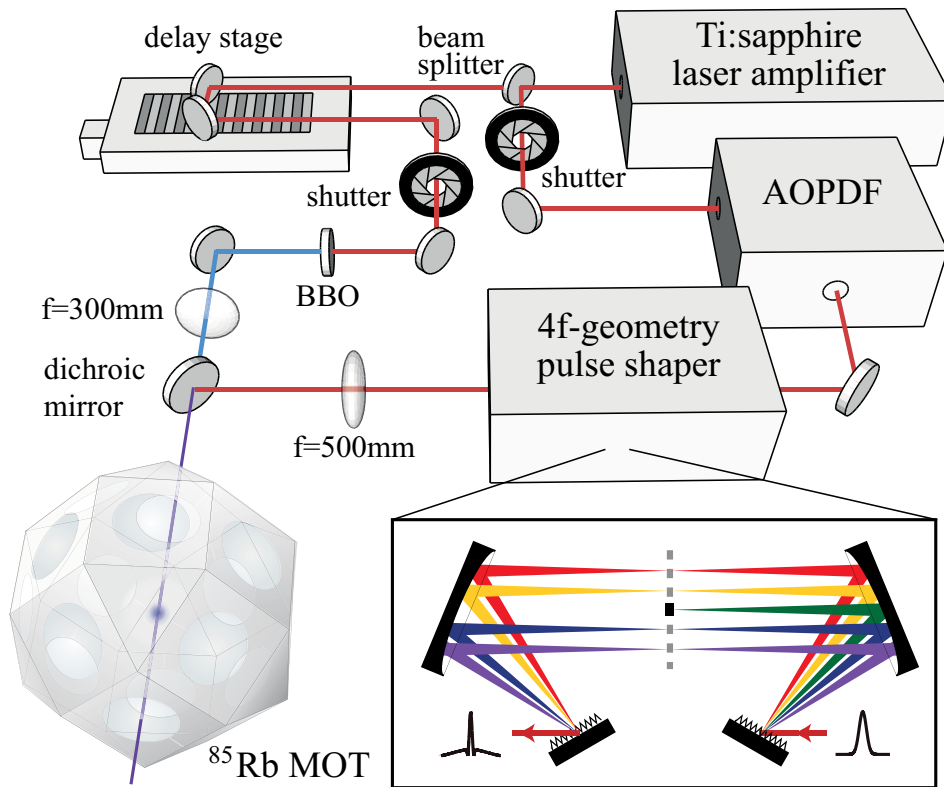


Figure 7.3: Schematics of the experimental setup. Femto-second laser pulses were shaped by an acousto-optic programmable dispersive filter (AOPDF) and a  $4f$ -geometry zero-dispersion stretcher; and as-produced chirped zero-area pulses interacted with cold rubidium atoms ( $^{85}\text{Rb}$ ) in a magneto-optical trap. After 3 ns, frequency-doubled laser pulses ionized the excited atoms.

system were  $|0\rangle = |5S_{1/2}\rangle$  and  $|1\rangle = |5P_{1/2}\rangle$ . The laser bandwidth was  $\Delta\lambda_{\text{FWHM}} = 7 \text{ nm}$  ( $\Delta\omega_1 = 1.5 \times 10^{13} \text{ rad/s}$ ), which was narrow enough to restrict the quantum system to a two-state system, and the corresponding pulse duration was  $\tau_{0,1} \simeq 140 \text{ fs}$ . Since the hyperfine splittings of  $|5S_{1/2}\rangle$  and  $|5P_{1/2}\rangle$  states (up to 3GHz) are much smaller than the laser bandwidth of THz order, the hyperfine states can be reduced to a two-state system through Morris-shore transform [47], giving  $\mu = 1.46 \times 10^{-29} \text{ Cm}$  [45].

Each femto-second laser pulse was divided into two: the first (control) pulse after being shaped to a chirped zero-area pulse induced the atomic transition, and the second (probe) pulse was frequency-doubled to ionize atoms in the excited state. The chirped zero-area pulse was prepared in two stages: the laser pulse was first frequency-chirped, up to  $c_2 = 6 \times 10^4 \text{ fs}^2$ , by an acousto-optic programmable dispersive filter (Dazzler from Fastlite) [12], and the spectrum near the resonance was removed by a spectral block in the Fourier plane defined by a  $4f$ -geometry Martinez zero-dispersion stretcher (home-made) [3, 57], which consisted of a pair of  $R=500 \text{ mm}$  cylindrical mirrors and a pair of gratings with 1800 grooves/mm. For the spectral block, we used various metal wires of which the spectral width ranges from 200 to 1000 GHz in FWHM (or  $\Delta\omega_2 = 7.7 \times 10^{11} \sim 3.9 \times 10^{12} \text{ rad/s}$  in Gaussian width). After the two-stage of pulse shaping, the laser pulse energy was up to  $20 \mu\text{J}$ .

We used a conventional magneto-optical trap (MOT) to spatially isolate the rubidium atoms [34]. By adjusting the diameters of the cooling and repumping laser beams, an atomic cloud of about  $200 \mu\text{m}$  diameter and  $6 \times 10^9 \text{ cm}^3$  atom density was prepared. The atoms were tightly confined in particular to achieve a uniform laser-atom interaction [38]. When the laser pulses were focused on to the atomic vapor, the laser beam diameter of  $600 \mu\text{m}$  was about 3 times bigger than the diameter of the atom cloud. With this diameter ratio, we achieved 95% of high fidelity for a  $\pi$ -area transform-limited pulse excitation. The laser pulse energy (up to  $20 \mu\text{J}$ ) with the given beam diameter was equivalent to  $\Theta_{\text{max}} = 3.5\pi$ . After being interacted with the control pulse (the chirped zero-area pulse), atoms in the excited state were ionized by the probe pulse, and resulting ions were measured by a multichannel plate detector. The overall experimental cycle controlled by mechanical shutters in laser beam lines was 2 Hz to grant the restoration of the MOT.

## 7.4 Experimental Results and discussion

Figure 7.4(a) shows the experimental result. By varying the power and the chirp parameter  $c_2$  of the chirped zero-area pulse, the excited-state population was measured. The spectral block of  $\Delta f(\text{FWHM}) = 500 \text{ GHz}$  ( $\Delta\omega_2 = 1.9 \times 10^{12} \text{ rad/s}$ ) around the resonance was removed in the  $4f$ -geometry stretcher. In comparison, the corresponding numerical calculation is shown in Fig. 7.4(b). The numerical calculation is based on Eq. (7.20). Since the experiment was performed under the condition of non-uniform spatial profiles of the laser pulse and the atom cloud, the calculation took into account the spatial averaging effect [38], where  $\Theta_{\text{Rabi}}^{\text{max}}$  in the  $x$ -axis denotes the maximum of the Gaussian distribution of  $\Theta_{\text{Rabi}}$ . The measured populations were calibrated to probabilities by using the first peak of Rabi oscillations as a reference. Within the available measurement region, the experimental result shows that the dark CPR region is surrounded by the bright CPI region, in a good agreement with the theoretical calculation. In addition, we probed the effect of the width of the spectral hole. The frequency chirp was fixed at  $c_2 = 5 \times 10^4 \text{ fs}^2$ , and the spectral hole was varied from 200 to 1000 GHz (FWHM). In Fig. 7.4(c), the measured pulse energies (shown with squares) for the first CPI peaks are displayed in comparison with the corresponding numerical calculation (dots).

We now consider possible applications of the chirped zero-area excitation implicated from the results

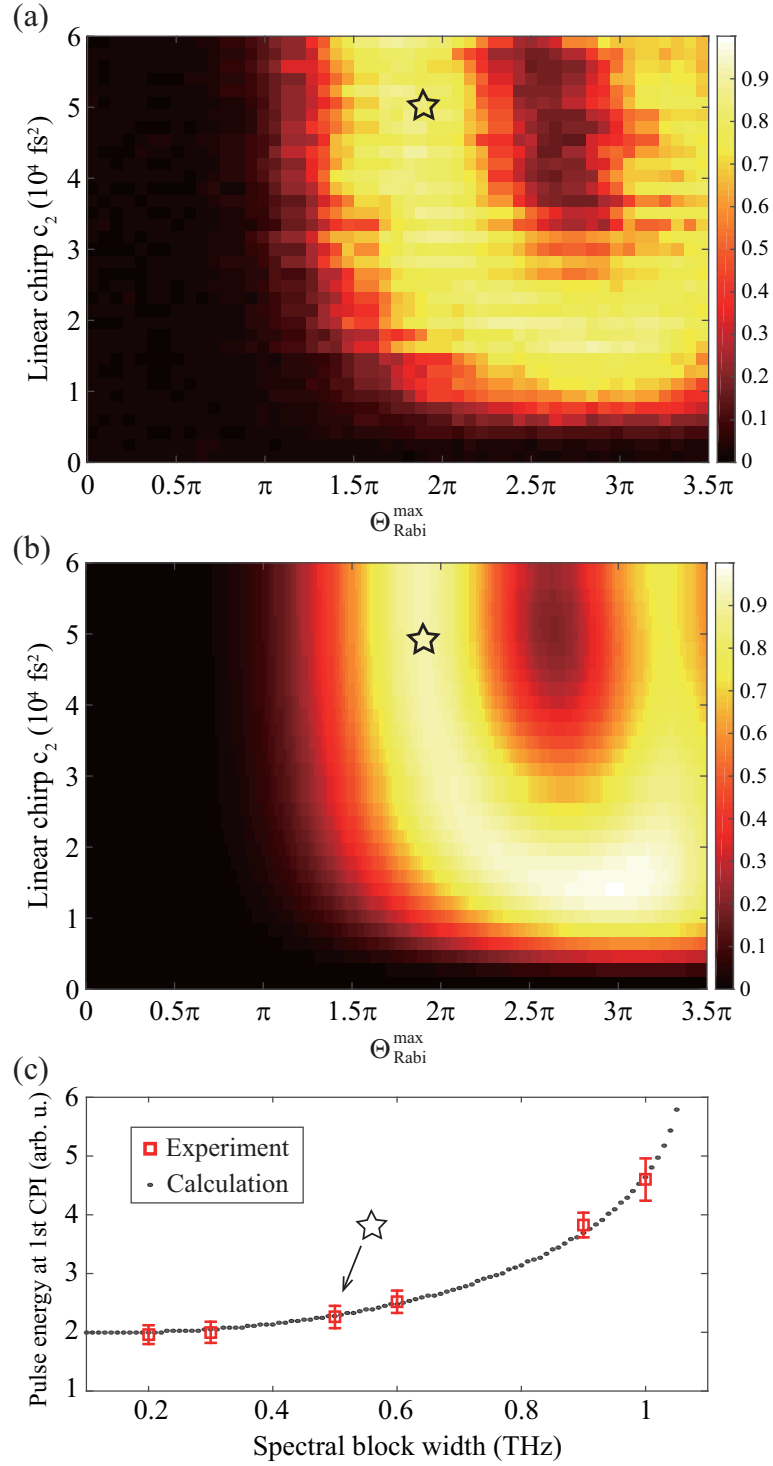


Figure 7.4: (a) Experimental result and (b) numerical simulation of the chirped zero-area pulse excitation of a cold rubidium atom ensemble. The transition probabilities were plotted as a function of  $c_2$  (linear chirp) and  $\Theta_{\text{Rabi}}^{\text{max}}$ . Interaction inhomogeneity due to the Gaussian spatial profile of the atom ensemble was taken into account for the calculation of (b). (c) Experimental result of spectral hole-width scan. Measured pulse energies for the first CPI (e.g., the stars marked in (a) and (b)) are plotted for various spectral hole widths (red squares), in comparison with the calculation result (black dots).



obtained in this study. Since the two-state system interacting with the chirped zero-area pulse can undergo, amid the adiabatic evolution ( $z$ -rotation) by the main pulse, Rabi-like rotation due to the non-adiabatic interaction by the hole pulse, an interplay between Rabi-like rotations and adiabatic evolutions can be made by shaping the spectral width and position of the hole. This approach can be a powerful and alternative control means in selective excitation of, in particular, multi-state systems. In a  $V$ -type system [13] of  $5S_{1/2}$ ,  $5P_{1/2}$ , and  $5P_{3/2}$  in rubidium, for example, a numerical simulation (not shown) with chirped zero-area pulses results in over 97% population of the system driven to either excited states, by simply changing the pulse intensity only. Also, this control method implicates that the laser spatial profile is also useful for position-dependent selective excitations, which can be applied to, for example, atom or ion qubits in spatial arrangements [58, 59].

## Chapter 8. Dynamics of a two-state system induced by a temporal hole on a chirped pulse

From the successful study on dynamics induced by chirped zero-area pulse, we have noticed great possibilities of quantum control in adiabatic basis. And for the first step of such control scheme, we considered Rabi rotations naturally described in adiabatic basis. In adiabatic basis, the time-dependent change of mixing angle  $\vartheta(t)$  gives coupling between two states. Thus, to make Rabi rotation in adiabatic basis, we should change  $\vartheta(t)$  rapidly at a certain  $t$ . This can be efficiently done at  $t = 0$  since  $\Delta(t) \rightarrow 0$  at near  $t = 0$ . Small change of  $\Omega(t)$  at near  $t = 0$  can give very rapid change of  $\vartheta(t)$ . For a simple and experimentally possible pulse shape to induce such rapid change, we attempted to make a temporal hole on a chirped pulse. Detailed dynamics of a two-level system induced by a chirped pulse with a temporal hole and experimental result will be discussed in this chapter.

### 8.1 Theoretical model

Let us start from the interaction between a two-level system, which consists of a ground state  $|0\rangle$  and an excited state  $|1\rangle$ , and a linearly chirped pulse. The Hamiltonian for the interaction is given by

$$H = \begin{bmatrix} -\hbar\omega_o/2 & \mu E(t) \\ \mu E(t) & \hbar\omega_o/2 \end{bmatrix}, \quad (8.1)$$

where  $E(t)$  is electric field of the pulse,  $\omega_o$  is a resonant frequency and  $\mu$  is a transition dipole moment of the two-level system. The temporal electric field,  $E(t)$ , of a linearly chirped pulse centered at  $\omega_o$  is written as

$$E(t) = E_o A(t) \cos[(\omega_o + \alpha t)t], \quad (8.2)$$

where  $E_o$  is an amplitude parameter,  $A(t)$  is a normalized envelope of the electric field and  $\alpha$  is a linear chirp parameter. If the pulse is Gaussian, the envelope is given by  $A(t) = e^{-t^2/\tau^2}$ . Note that the instantaneous frequency of  $E(t)$  is  $\omega(t) = \frac{d}{dt}[(\omega_o + \alpha t)t] = \omega_o + 2\alpha t$ . After transforming into the interaction picture and making rotating wave approximation, the Hamiltonian of (8.1) becomes an interaction Hamiltonian  $V_I$  as

$$V_I = \frac{\hbar}{2} \begin{bmatrix} -\Delta(t) & \Omega(t) \\ \Omega(t) & \Delta(t) \end{bmatrix} \quad (8.3)$$

where  $\Delta(t) = \omega_o - \omega(t) = -2\alpha t$  is instantaneous detuning and  $\Omega(t) = \mu E(t)/\hbar$  is the Rabi frequency.

When the applied chirp is large and the Rabi frequency is kept large enough during the evolution, the system's evolution is adiabatic. This well-known adiabatic evolution by a linearly chirped pulse is called RAP (rapid adiabatic passage) and results in CPI (complete probability inversion) of the system. However, by making a temporal hole on the chirped pulse, we can manipulate the Rabi frequency in the middle of the time evolution, and can induce non-adiabatic coupling for controlling the evolution. If the adiabatic evolution is described in adiabatic basis, a basis formed by eigenstates of the interaction Hamiltonian  $V_I$ , the system stays in same state all along the evolution. Thus, transforming into the

adiabatic basis will be helpful to study non-adiabatic coupling induced by the temporal hole. The eigenvalues of  $V_I$  are given by

$$\frac{\hbar}{2}\lambda_{\pm}(t) = \pm \frac{\hbar}{2}\sqrt{\Omega_1^2(t) + \Delta^2(t)} \quad (8.4)$$

and the corresponding eigenstates are

$$\begin{aligned} |\psi_{-}(t)\rangle &= \cos \vartheta(t)|0\rangle - \sin \vartheta(t)|1\rangle, \\ |\psi_{+}(t)\rangle &= \sin \vartheta(t)|0\rangle + \cos \vartheta(t)|1\rangle, \end{aligned} \quad (8.5)$$

where the mixing angle  $\vartheta(t)$  is given by

$$\vartheta(t) = \frac{1}{2} \tan^{-1} \frac{\Omega_1(t)}{\Delta(t)} \quad \text{for } 0 \leq \vartheta(t) \leq \frac{\pi}{2}. \quad (8.6)$$

Here, we can define a unitary transform  $|\psi(t)\rangle_A = R(\vartheta(t))|\psi(t)\rangle$ , from a state of the initial two-level system,  $|\psi(t)\rangle$ , to a state in adiabatic basis,  $|\psi(t)\rangle_A$ . The transform matrix  $R(\vartheta)$  is defined by

$$R(\vartheta) = \begin{bmatrix} \cos \vartheta(t) & -\sin \vartheta(t) \\ \sin \vartheta(t) & \cos \vartheta(t) \end{bmatrix}. \quad (8.7)$$

In the given adiabatic basis, the Schrödinger equation is given by

$$i\hbar \frac{d}{dt} |\psi(t)\rangle_A = \left( R V_I R^{-1} - i\hbar R \dot{R}^{-1} \right) |\psi(t)\rangle_A, \quad (8.8)$$

where the term  $-i\hbar R \dot{R}^{-1}$  is from time-dependence of the transform matrix  $R(\vartheta(t))$  and given by

$$-i\hbar R \dot{R}^{-1} = i\hbar \begin{bmatrix} 0 & -\dot{\vartheta} \\ \dot{\vartheta} & 0 \end{bmatrix}. \quad (8.9)$$

Thus, the interaction Hamiltonian in adiabatic basis is defined as

$$V_A = \frac{\hbar}{2} \begin{bmatrix} \lambda_{-} & -2i\dot{\vartheta} \\ 2i\dot{\vartheta} & \lambda_{+} \end{bmatrix}, \quad (8.10)$$

which describes a two-state system with a time-varying energy splitting of  $\lambda_{+} - \lambda_{-} = \sqrt{\Delta^2 + \Omega^2}$  and driving interaction  $2\dot{\vartheta}$ . Note that the off-diagonal term  $2\dot{\vartheta}$  in adiabatic basis usually called “non-adiabatic coupling”, and explicitly given by

$$2\dot{\vartheta} = \frac{|\dot{\Omega}(t)\Delta(t) - \Omega(t)\dot{\Delta}(t)|}{\Delta^2(t) + \Omega^2(t)}. \quad (8.11)$$

The diagonal components of the Hamiltonian in Eq. (8.10) doesn't become 0 even if  $\Omega(t) = 0$ . Thus, the phase of the state evolves without the pulse and diverges at  $t \rightarrow \pm\infty$ . To remove the phase evolution before and after the pulse duration, we need another transform  $T_{\Delta} = \exp \left( i \int_0^t H_{\Delta}(t') dt' / \hbar \right)$ , where  $H_{\Delta}$  is defined by

$$H_{\Delta} = \frac{\hbar}{2} \begin{bmatrix} -|\Delta(t)| & 0 \\ 0 & |\Delta(t)| \end{bmatrix}. \quad (8.12)$$

And the interaction Hamiltonian finally becomes

$$V_F = \frac{\hbar}{2} \begin{bmatrix} -\Delta_F(t) & \Omega_F(t) \\ \Omega_F^*(t) & \Delta_F(t) \end{bmatrix}, \quad (8.13)$$

where

$$\begin{aligned}\Delta_F(t) &= \sqrt{\Delta^2(t) + \Omega^2(t)} - |\Delta(t)| \\ \Omega_F(t) &= -2i\dot{\vartheta}e^{-i|\Delta(t)|/2}.\end{aligned}\quad (8.14)$$

Note that the additional phase of off-diagonal component is  $|\Delta(t)|t/2$ , which is defined by  $\int_0^t |\Delta(t')|dt'$ . The Hamiltonian in Eq. (8.10) and Eq. (8.13) gives identical time evolution except phase evolution. Since its components are all real, Eq. (8.10) is convenient to consider dynamics intuitively. On the other hand, Eq. (8.13) is suitable to describe time evolution in numerical way because unnecessary phase evolution is dropped. Thus, the dynamics will be explained in Eq. (8.10) and the numerical calculations of time evolution will be given in Eq. (8.13).

Now consider a chirped pulse with a temporal hole. To suppress altering of the spectrum by the temporal hole, and also for experimental realization, the temporal hole must be smooth. For a good example, let us define a chirped Gaussian pulse with a Gaussian temporal hole, which is given by

$$E(t) = NE_o(e^{-t^2/\tau^2} - ke^{-t^2/\tau_h^2})\cos[(\omega_o + \alpha t)t], \quad (8.15)$$

where  $\tau_h$  is width and  $k$  is depth of a temporal hole. Note that the temporal hole directly changes energy of the pulse, a normalization factor  $N$  is introduced to maintain the pulse energy and given by

$$N = \sqrt{\frac{\int_{-\infty}^{\infty} e^{-2t^2/\tau^2} dt}{\int_{-\infty}^{\infty} (e^{-t^2/\tau^2} - e^{-t^2/\tau_h^2})^2 dt}}. \quad (8.16)$$

Fig. 8.1 a) and b) show time dependent change of electric field envelope  $A(t)$  and mixing angle  $\vartheta(t)$  for cases without and with a temporal hole, respectively. As shown in Fig. 8.1 a), a largely chirped Gaussian pulse gives slowly varying  $2\dot{\vartheta}$  during evolution, because of slow and smoothly varying  $\Delta(t)$  and  $\Omega(t)$ . Also,  $A(t)$  maintains the energy splitting  $\lambda_+ - \lambda_- = \sqrt{\Delta^2 + \Omega^2}$  large, even at near  $t = 0$  where  $\Delta(t) \rightarrow 0$ . Thus, the condition  $2\dot{\vartheta} \ll |\lambda_+ - \lambda_-|$  is kept all along the system evolution, which results in  $z$ -rotation in adiabatic basis, or adiabatic evolution. However, as shown in Fig. 8.1 b), a temporal hole located at  $t = 0$  makes  $A(t)$  small at  $t = 0$ . As a result, rapid change of  $\vartheta(t)$  occurs across  $t = 0$  and the conditions  $\vartheta(t) \gg |\lambda_+ - \lambda_-|$  is made near  $t = 0$ , which results in rabi rotation. Note that in Fig. 8.1 b), temporal hole is defined by width of  $\tau_h = 0.1\tau$  and depth of  $k = 0.9$ .

Starting from a common initial state  $(|\psi_- \rangle + |\psi_+ \rangle)/\sqrt{2}$ , time evolution on a Bloch sphere corresponding to two cases Fig. 8.1 a) and b), are respectively plotted in Fig. 8.1 d) and e). Fig. 8.1 d) and e) are calculated in the system described by Eq. (8.13) and  $x$ -axis  $y$ -axis are azimuthal angle and polar angle on a Bloch sphere, respectively. As shown in Fig. 8.1 e), a narrow and deep enough temporal hole induces very rapid change of  $\dot{\vartheta}(t)$  and rabi rotation occurs at central region of the hole. Thus, for a narrow and deep temporal hole, the Hamiltonian in the central region (also indicated by red solid line in Fig. 8.1 b) and e)) of temporal hole,  $-\tau_h < t < \tau_h$ , can be approximated by

$$V_{\text{hole}} \simeq \frac{\hbar}{2} \begin{bmatrix} 0 & -2i\dot{\vartheta} \\ 2i\dot{\vartheta} & 0 \end{bmatrix}, \quad (8.17)$$

which describes  $y$  rotation on Bloch sphere. The  $y$ -rotation angle can be obtained by

$$\begin{aligned}\Theta &= \int_{-\tau_h}^{\tau_h} 2\dot{\vartheta} dt \\ &= 2[\vartheta(t = \tau_h) - \vartheta(t = -\tau_h)].\end{aligned}\quad (8.18)$$

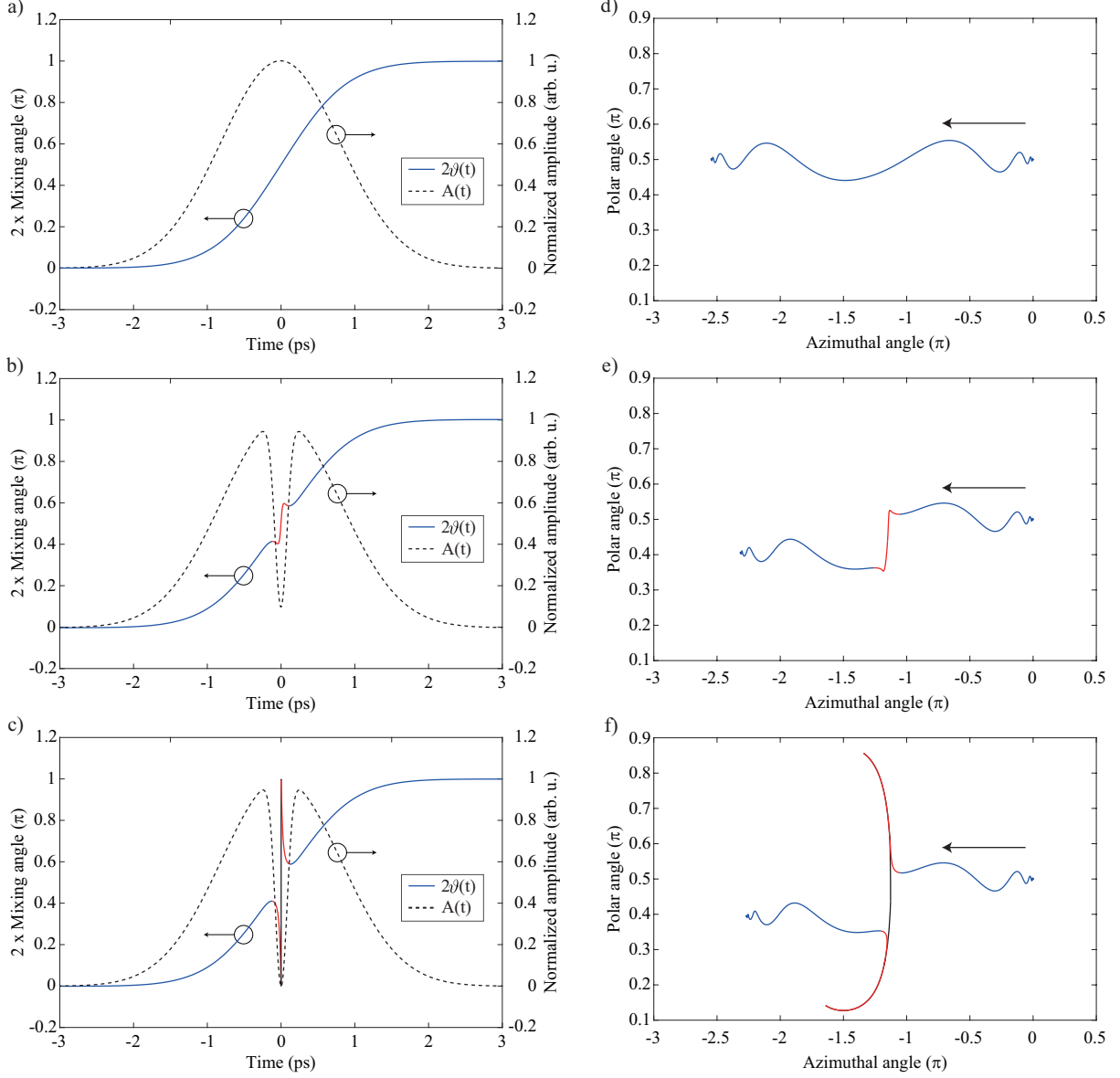


Figure 8.1: a-c) Time dependences of Normalized electric field envelope and mixing angle  $2\theta$  are plotted for a) a chirped pulse, b) a chirped pulse with a temporal hole of width  $\tau_h = 0.1\tau$  and depth  $k = 0.9$ , c) a chirped pulse with a temporal hole of width  $\tau_h = 0.1\tau$  and depth  $k = 1$ . d-f) Evolution on Bloch sphere in adiabatic basis corresponding to a), b) and c) are respectively plotted and the arrows indicates direction of evolution. x-axis is azimuthal angle on the Bloch sphere and y-axis is polar angle on the Bloch sphere. For b), c), e) and f), red line indicated  $-\tau_h < t < \tau_h$  region, and For c) and f), black line indicates changes at  $t = 0$ .

In the outside region  $t > \tau_h$  and  $t < -\tau_h$ , two  $z$ -rotations occur. The  $z$ -rotation angles also can be calculated using Hamiltonian Eq. (8.13),

$$\begin{aligned}\phi_1 &= \int_{-\infty}^{-\tau_h} \sqrt{\Delta^2(t) + \Omega^2(t)} - |\Delta| dt \\ \phi_2 &= \int_{\tau_h}^{\infty} \sqrt{\Delta^2(t) + \Omega^2(t)} - |\Delta| dt.\end{aligned}\quad (8.19)$$

Note that  $\phi_1 = \phi_2$  if the temporal envelope of the pulse is symmetric with respect to  $t = 0$ .

Fig. 8.1 c) shows time dependent change of  $\vartheta$  and  $A(t)$ , and f) shows corresponding evolution described on Bloch sphere when  $k = 1$ . If depth of the temporal hole becomes  $k = 1$ , nonlinear change of envelope  $A(t)$  can exceed linear change of  $\Delta(t)$  at near  $t = 0$ . As a result,  $\Omega(t) < \Delta(t)$  relation hold for  $t \rightarrow \pm 0$  and a discontinuous step change of the mixing angle  $\vartheta$  occurs at  $t = 0$ . The change of  $\vartheta$  is  $\pi$  since  $\lim_{x \rightarrow 0^+} \tan^{-1}(x) = 0$  and  $\lim_{x \rightarrow 0^-} \tan^{-1}(x) = \pi$  in the range of  $\vartheta$ . The  $\pi$  change of  $\vartheta$  at  $t = 0$  is indicated by black solid line in Fig. 8.1 c) and this step change of  $\vartheta$  causes a Rabi rotation at  $t = 0$ , shown in Fig. 8.1 f) also by black solid line. In addition, in the region of  $-\tau_h < t < 0$  and  $0 < t < \tau_h$  (indicated by red solid line in Fig. 8.1 f)), two rabi rotations are respectively occurs. Since Hamiltonian for all Rabi rotations can be approximated by Eq. (8.17), they are  $y$ -rotations. The rotation angle is given by

$$\begin{aligned}\Theta &= \pi + \int_{-\tau_h}^{0^-} 2\dot{\vartheta} dt + \int_{0^+}^{\tau_h} 2\dot{\vartheta} dt \\ &= \pi + 2\vartheta(t = \tau_h) - \pi + 0 - 2\vartheta(t = -\tau_h) \\ &= 2[\vartheta(t = \tau_h) - \vartheta(t = -\tau_h)].\end{aligned}\quad (8.20)$$

From Eq. (8.18) and Eq. (8.20), the  $y$ -rotation angle at central region is always given by  $\Theta = 2[\vartheta(t = \tau_h) - \vartheta(t = -\tau_h)]$ . The  $z$ -rotation angle in  $|t| > \tau_h$  region is same as  $k < 1$  case, given as Eq. (8.19).

From the discussion above, the total time evolution operator  $U$  by a chirped pulse with a temporal hole can be expressed by three-rotations

$$U = R_z(\phi_2)R_y(\Theta)R_z(\phi_1). \quad (8.21)$$

Explicitly,  $U$  is given by

$$U = \begin{bmatrix} e^{i\phi_2} & 0 \\ 0 & e^{-i\phi_2} \end{bmatrix} \begin{bmatrix} \cos(\Theta) & -\sin(\Theta) \\ \sin(\Theta) & \cos(\Theta) \end{bmatrix} \begin{bmatrix} e^{i\phi_1} & 0 \\ 0 & e^{-i\phi_1} \end{bmatrix}. \quad (8.22)$$

If the initial state is given by

$$\psi(-\infty) = (|\psi_- \rangle + e^{i\varphi} |\psi_+ \rangle) / \sqrt{2}, \quad (8.23)$$

where  $\varphi$  is the relative phase, then probabilities of two states after time evolution is respectively given by

$$\begin{aligned}P_- &= |\langle \psi_- | U | \psi(-\infty) \rangle|^2 \\ &= \frac{1}{2} [1 - \sin(2\Theta) \cos(2\phi_1 - \varphi)], \\ P_+ &= |\langle \psi_+ | U | \psi(-\infty) \rangle|^2 \\ &= \frac{1}{2} [1 + \sin(2\Theta) \cos(2\phi_1 - \varphi)].\end{aligned}\quad (8.24)$$

Eq. (8.24) shows that when the initial state of the system is a superposition state, the system undergoes a probability oscillation by a chirped pulse with a temporal hole. The oscillation amplitude is governed by  $y$ -rotation angle  $\Theta$ , and peak position depends on  $z$ -rotation angle  $\phi_1$ .

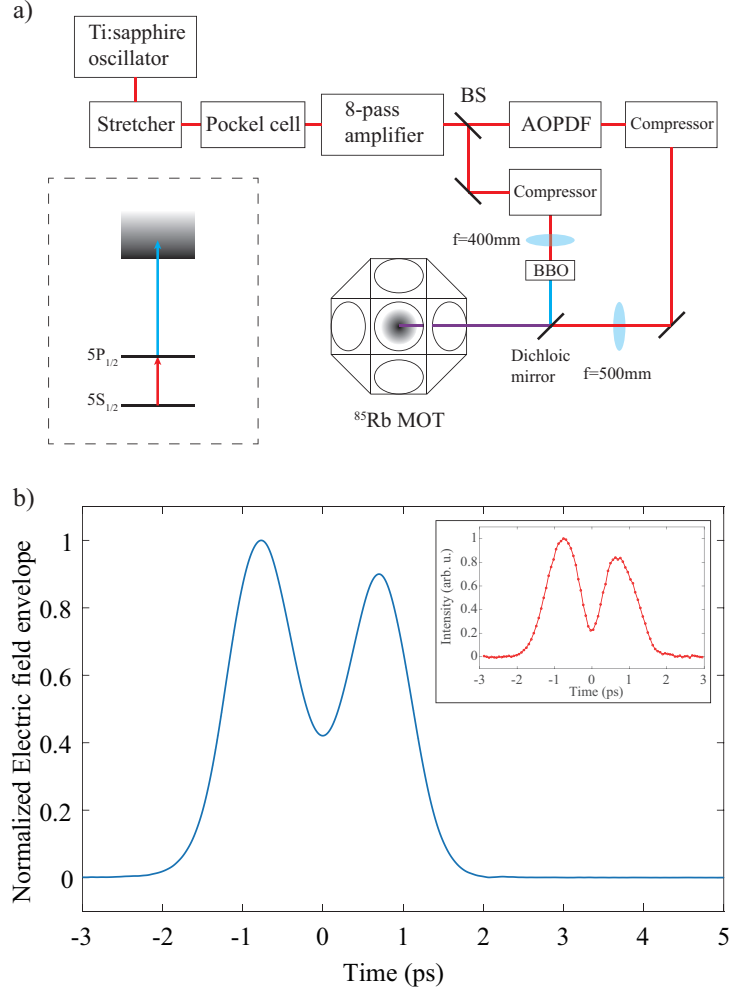


Figure 8.2: a) Schematics of the experimental setup and level diagram of  $^{85}\text{Rb}$  atom. Our two-level system consists of  $5S_{1/2}$ ,  $5P_{1/2}$  states of  $^{85}\text{Rb}$ . To measure  $|\psi_{-}\rangle$  probability after the interaction, applied ionization pulse ionize  $5P_{1/2}$  state atoms only and  $\text{Rb}^{+}$  ions counted via microchannel plate(MCP). b) Electric field envelope used for experiment, which is calculated from measured intensity profile. Due to the limited spectral resolution of pulse shaping, the temporal hole removed about 60% of electric field at  $t = 0$ . Inset shows measured intensity profile via cross-correlation. The asymmetry of the pulse comes from spectral asymmetry, however, gives no significant effect on dynamics.

## 8.2 Experimental Setup

As stated in Eq. (8.24), a chirped pulse with a temporal hole induces probability oscillation of a two-level system when the initial state is a superposition of  $|\psi_{-}\rangle$  and  $|\psi_{+}\rangle$ . For experimental realization of such phenomenon, we used a Ti:sapphire laser amplifier system, which is equipped with a pulse shaping apparatus. Our homemade Ti:sapphire laser amplifier generates femtosecond laser pulses in 1 kHz repetition rate. Spectrum of the pulse was centered at 794.7 nm, corresponding to the  $5S_{1/2} \rightarrow 5P_{1/2}$  transition of the rubidium atom, and the bandwidth of the pulse was 3 THz in Gaussian width. Since the time evolution by a chirped pulse with a temporal hole should start from a superposition state, a  $\pi/2$  pulse was required in advance to prepare  $(|0\rangle + |1\rangle)/\sqrt{2}$  initial state. To generate a pulse sequence of a  $\pi/2$  pulse and a chirped pulse with temporal hole, an acousto-optic pulse shaper (AOPDF, Dazzler from Fastlite) simultaneously programmed both spectral amplitude and phase of each laser pulse. The generation a pulse sequence is handled in frequency domain and the priciple can be written as

$$\tilde{S}(\omega) = \tilde{S}_1(\omega) + n\tilde{S}_2(\omega) \exp(i\varphi) \quad (8.25)$$

where  $\tilde{S}_1(\omega)$  is a spectral electric field for a  $\pi/2$  pulse,  $\tilde{S}_2(\omega)$  is for a chirped pulse with a temporal hole,  $n$  is relative amplitude of the chirped pulse with a temporal hole and  $\varphi$  is a relative phase. The linear chirp of the chirped pulse with a temporal was fixed at  $60000 \text{ fs}^2$ . Because the total energy  $|\tilde{S}(\omega)|^2$  of the programmed pulse sequence output from the acouto-optic pulse shaper is limited by RF power, relative amplitude  $n$  and applied RF power must be controlled simultaneously to keep the  $\tilde{S}_1(\omega)$  as a  $\pi/2$  pulse. Thus, along with the change of RF power and relative amplitude  $k$ , the relative energy between two pulses was measured and calibrated by using a photodiode and cross-correlation. Figure 8.2 b) shows an electric field envelope of the chirped pulse with a temporal hole. The envelope was calculated from measured intensity profile via cross-correlation. Another pulse with temporal Gaussian width of 300 fs was used for cross-correlation measurement and the result is plotted in the inset of Figure 8.2 b). The delay between the  $\pi/2$  pulse and the chirped pulse with a temporal hole was maintained as 2.2 ps and relative phase between two pulses was controlled by changing  $\varphi$ , which is defined in Eq. (8.25). Total energy of the shaped pulse sequence was upto  $20 \mu\text{J}$ . After interating with the chirped pulse with a temporal hole,  $5P_{1/2}$  state atoms are selectively ionized by a frequency doubled 400 nm ionization pulse, and ions are measured via micro channel plate. Note that after the interaction,  $\psi_{-}\rangle$  state probability is identical to  $5P_{1/2}$  state probability since  $\psi_{-}(\infty)\rangle = -|1\rangle$ . To minimize inhomogeneity of the interaction, laser beam size at interaction region was made about 2.3 times bigger than the MOT atomic cloud. The size of MOT atomic cloud was about  $250 \mu\text{m}$  in FWHM (full width at half maximum).

## 8.3 Results and Discussion

In figure 8.3 a) and b), calculated and experimentally measured probability of  $|\psi_{-}\rangle$  state after interacting with a chirped pulse with a hole are respectively plotted as a function of calibrated peak pulse area and initial state relative phase  $\varphi$ . The calibration of peak pulse area is same as section 7.4. For direct comparison between two plots in Fig. 8.3 a), spatial inhomogeneity of the interaction is included in calculation. As described in Fig. 8.2, only about 60% of the electric field was remove at  $t = 0$  due to the limited spectral resolution of pulse shaping apparatus. In this case,  $y$ -rotation angle  $\Theta$  induced by non-adiabatic coupling gradually increases to a certain peak value as electric field amplitude  $E_0$  becomes larger. And after the peak,  $\Theta$  decreases since remaining  $\omega(t = 0)$  makes the change of  $\vartheta$  slower at near



$t = 0$  and the evolution at central region gradually approaches to an adiabatic evolution. The change of  $\Theta$  as a function of electric field amplitude  $E_0$  is directly shown by the probability oscillation amplitude depending on initial state relative phase (while keeping  $E_0$  as a constant).  $\phi_1$  is a monotonic function on  $E_0$ :  $\phi_1$  is increased when  $E_0$  increases. Change of the minimum and maximum probability position in  $\varphi$  axis shows change of  $\phi_1$ . Since  $\phi_1$  is positively proportional to  $E_0$ , the position of the maximum and minimum moves to upper-right direction as  $E_0$  increases. Calculation and experimental results along three dashed lines in Fig. 8.3 a) and b) are simultaneously plotted in Fig. 8.3 c). The change of peak position shows dependence of  $\phi_1$  on  $E_0$  and the change of oscillation amplitude shows dependence of  $\Theta$  on  $E_0$ .

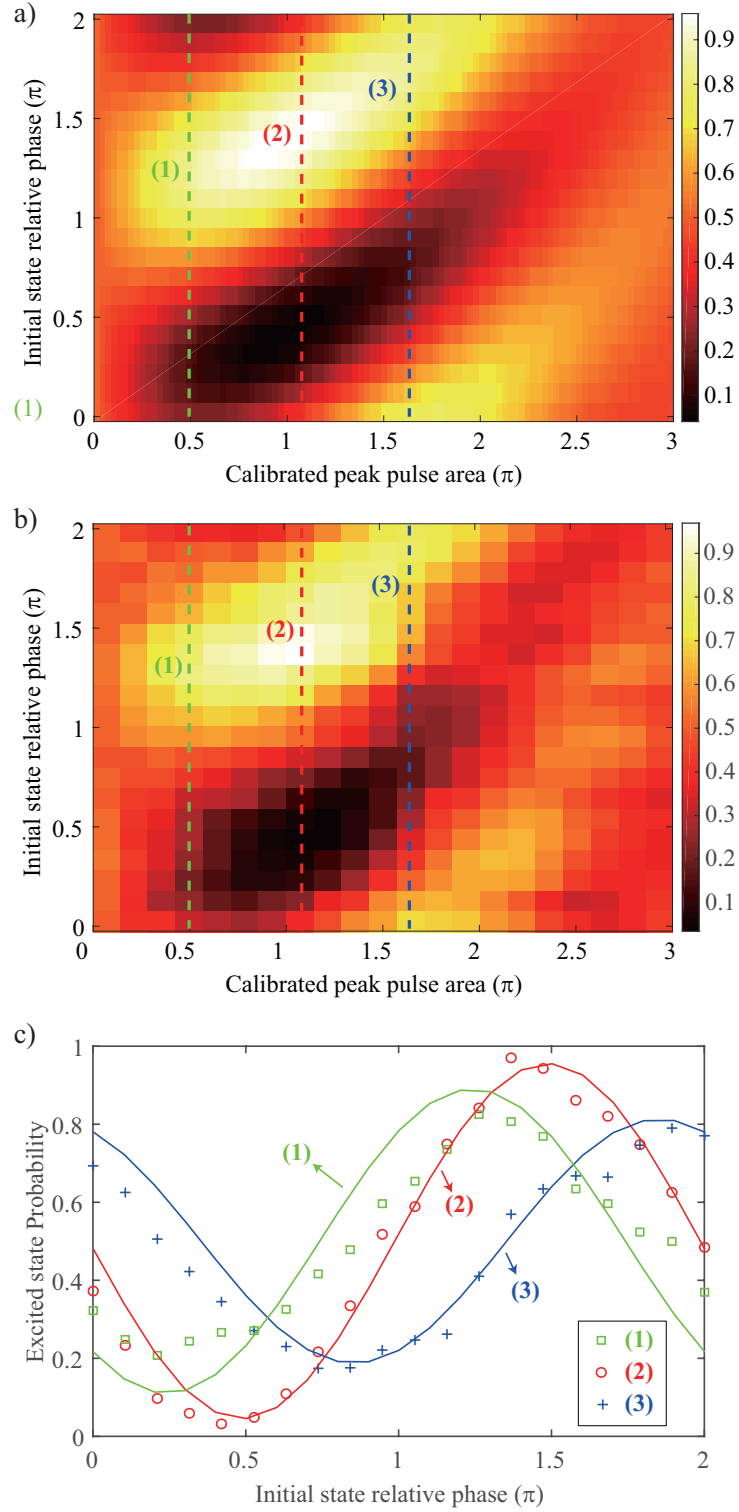


Figure 8.3: a) Starts from a initial state of  $(|\psi_{-}\rangle + |\psi_{+}\rangle e^{i\varphi})/\sqrt{2}$ , calculated probability of  $|\psi_{-}\rangle$  state after interacting with a chirped pulse with a hole is plotted as a function of calibrated peak pulse area and initial state relative phase  $\varphi$ . Spatial inhomogeneity of the interaction is also included in calculation. b) Measured probability of  $|\psi_{-}\rangle$  (or  $|1\rangle$ ) state after interacting with a chirped pulse with a hole is plotted as a function of calibrated peak pulse area and initial state relative phase  $\varphi$ . c) Calculation and experimental results along three dashed lines in a) and b) are simultaneously plotted.

## Chapter 9. Conclusion

In this dissertation, quantum control of alkali atoms in ensemble was widely studied from weak field regime to strong field regime, by using broadband pulse shaping scheme.

In the weak field regime, two photon transitions of a four-level system of the rubidium atom in a diamond configuration was considered. Since the dynamics can be expressed by perturbation, parameter for quantum control was spectral phase, rather than amplitude. The interference between two two-photon excitation passages was maximized by considering inherent phases of eight probability amplitude components and the experimental result showed good agreement with the theoretical prediction.

In the strong field regime, spatial inhomogeneity of interaction give large error in experiment, even a complete wipeout of the dynamics. Thus, quantitative analysis on ensemble averaged Rabi oscillation was conducted to develop a model for spatial inhomogeneity of interaction. The cold atomic rubidium vapor spatially confined in a magneto-optical trap was driven by the resonant ultrafast laser pulse, and the oscillation of excited population was probed as a function of the pulse energy. Theoretical model calculation based on assumption of a Gaussian atomic ensemble and a Gaussian laser pulse and the experimental result showed very good agreement. The most important result of this study was the development of the estimation method for inhomogeneous interaction, which can be applied to any strong field dynamics.

Dynamics of a two-level system induced by chirped pulses with spectral and temporal hole showed a new control method of two-level system, which utilizes interplay between adiabatic evolution and the Rabi rotation. The chirped pulses in these works induce adiabatic evolution, where this adiabatic evolution can be regarded as a background with interesting properties. And the holes were made on the chirped pulse to apply Rabi rotations as control parameters in the middle of adiabatic evolution. As a result, interplay between the background and the hole was successfully demonstrated and complete probability oscillation was observed in both cases. The most valuable application of this work is selective excitation in multi-level system. Narrow spectral holes made on a chirped pulse at the temporal or spectral positions corresponding to resonances of the system can act as switches of adiabatic evolution of multi-level system. By varying pulse intensity, these switches can be turned on and off. As a result, transition paths are altered and transition probability to a desired state of  $\simeq 1$  can be obtained [60].

## Bibliography

- [1] D. J. Tannor and S. A. Rice, “Control of selectivity of chemical reaction via control of wave packet evolution,” *J. Chem. Phys.* **83**, 5013 (1985).
- [2] P. Brumer and M. Shapiro, “Coherence Chemistry: Controlling Chemical Reactions with Lasers,” *Acc. Chem. Res.* **22** 407, (1989).
- [3] R. L. Fork, O. E. Martinez, and J. P. Gordon, “Negative dispersion using pairs of prisms,” *Opt. Lett.* **9**, 150-152 (1984).
- [4] A. M. Weiner, “Femtosecond pulse shaping using spatial light modulators,” *Rev. Sci. Instrum.* **71**, 1929 (2000).
- [5] D. Meshulach and Y. Silberberg, “Coherent quantum control of multiphoton transitions by shaped ultrashort optical pulses,” *Phys. Rev. A* **60** 1287 (1999).
- [6] N. Dudovich, B. Dayan, S. M. Gallagher-Faeder, and Y. Silberberg, “Transform-limited pulses are not optimal for resonant multiphoton transitions,” *Phys. Rev. Lett.* **86**, 47 (2001).
- [7] N. Dudovich, D. Oron, and Y. Silberberg, “Single-pulse coherently controlled nonlinear Raman spectroscopy and microscopy,” *Nature* **418**, 512 (2002)
- [8] D. Oron, N. Dudovich, and Y. Silberberg, “Femtosecond phase-and-polarization control for background-free coherent anti-Stokes Raman spectroscopy,” *Phys. Rev. Lett.* **90**, 213902 (2003)
- [9] B. W. Shore, *Manipulating quantum structures using laser pulses* (Cambridge University Press, New York, 2011).
- [10] Y.-X. Du, Z.-T. Liang, Y.-C. Li, X.-X. Yue, Q.-X. Lv, W. Huang, X. Chen, H. Yan, and S.-L. Zhu, “Experimental realization of stimulated Raman shortcut-to-adiabatic passage with cold atoms,” *Nat. Commun.* **7**, 12479 (2016)
- [11] P. Tournois, “Acousto-optic programmable dispersive filter for adaptive compensation of group delay time dispersion in laser systems,” *Opt. Comm.* **140**, 245 (1997).
- [12] F. Verluise, V. Laude, Z. Cheng, Ch. Spielmann, and P. Tournois, “Amplitude and phase control of ultrashort pulses by use of an acousto-optic programmable dispersive filter: pulse compression and shaping,” *Opt. Lett.* **25**, 575 (2000)
- [13] J. Lim, H. G. Lee, S. Lee, and J. Ahn, “Quantum control in two-dimensional Fourier transform spectroscopy,” *Phys. Rev. A* **84**, 013425 (2011).
- [14] I. I. Rabi, J. R. Zacharias, S. Millman, and P. Kusch, “A new method of measuring nuclear magnetic moment,” *Phys. Rev.* **53**, 318 (1938).
- [15] A. Abragam, *Principles of Nuclear Magnetism* (Oxford University Press, Hong Kong, 2002).
- [16] L. Allen and J. H. Eberly, *Optical Resonance and Two-Level Atoms* (Dover, New York, 1987).

- [17] M. O. Scully and M. S. Zubiary, *Quantum Optics* (Cambridge University Press, Cambridge, 1997).
- [18] G. Rempe, H. Walther, and N. Klein, “Observation of quantum collapse and revival in a one-atom maser,” *Phys. Rev. Lett.* **58**, 353 (1987).
- [19] M. Brune, F. Schmidt-Kaler, A. Maali, J. Dreyer, E. Hagley, J. M. Raimond, and S. Haroche, “Quantum Rabi oscillation: a direct test of field quantization in a cavity,” *Phys. Rev. Lett.* **76**, 1800 (1996).
- [20] G. Wrigge, I. Gerhardt, J. Hwang, G. Zumofen, and V. Sandoghdar, “Efficient coupling of photon to a single molecule and the observation of its resonance fluorescence,” *Nature Phys.* **4**, 60–66 (2008).
- [21] A. Schülzgen, R. Binder, M. E. Donovan, M. Lindberg, K. Wundke, H. M. Gibbs, G. Khitrova, and N. Peyghambarian, “Direct observation of excitonic Rabi oscillations in semiconductors,” *Phys. Rev. Lett.* **82**, 2346 (1999).
- [22] T. H. Stievater, X. Li, D. G. Steel, D. Gammon, D. S. Katzer, D. Park, C. Piermarocchi, and L. J. Sham, “Rabi oscillations of excitons in single quantum dots,” *Phys. Rev. Lett.* **87**, 133603 (2001).
- [23] J. M. Martinis, S. Nam, J. Aumentado, and C. Urbina “Rabi oscillations in a large Josephson-junction qubit,” *Phys. Rev. Lett.* **89**, 117901 (2002).
- [24] M. R. Matthews, B. P. Anderson, P. C. Haljan, D. S. Hall, M. J. Holland, J. E. Williams, C. E. Wieman, and E. A. Cornell, “Watching a superfluid untwist itself: recurrence of Rabi oscillations in a Bose-Einstein condensate,” *Phys. Rev. Lett.* **83**, 3358 (1999).
- [25] J. R. Kuklinski, U. Gaubatz, F. T. Hioe, and K. Bergmann, “Adiabatic population transfer in a three-level system driven by delayed laser pulses,” *Phys. Rev. A* **40**, 6741 (1989).
- [26] K.-K. Ni, S. Ospelkaus, M. H. G. de Miranda, A. Pe’er, B. Neyenhuis, J. J. Zirbel, S. Kotochigova, P. S. Julienne, D. S. Jin, and J. Ye, “A High Phase-Space-Density Gas of Polar Molecules,” *Science*, **322**, 231 (2008).
- [27] A. A. Rangelov, N. V. Vitanov, L. P. Yatsenko, B. W. Shore, T. Halfmann, and K. Bergmann, “Stark-shift-chirped rapid-adiabatic-passage technique among three states,” *Phys. Rev. A* **72**, 053403 (2005)
- [28] N. V. Vitanov, T. Halfmann, B. W. Shore, and K. Bergmann, “Laser-Induced Population Transfer by Adiabatic Passage Techniques,” *Annu. Rev. Phys. Chem.* **52**, 763 (2001).
- [29] C.-M. Simon, T. Belhadj, B. Chatel, T. Amand, P. Renucci, A. Lemaitre, O. Krebs, P. A. Dalgarno, R. J. Warburton, X. Marie, and B. Urbaszek, “Robust Quantum Dot Exciton Generation via Adiabatic Passage with Frequency-Swept Optical Pulses,” *Phys. Rev. Lett.* **106**, 166801 (2011)
- [30] Y. Wu, I. M. Piper, M. Ediger, P. Brereton, E. R. Schmidgall, P. R. Eastham, M. Hugues, M. Hopkinson, and R. T. Phillips, “Population Inversion in a Single InGaAs Quantum Dot Using the Method of Adiabatic Rapid Passage,” *Phys. Rev. Lett.* **106**, 067401 (2011)
- [31] S. Zhdanovich, E. A. Shapiro, M. Shapiro, J. W. Hepburn, and V. Milner, “Population transfer between two quantum states by piecewise chirping of femtosecond pulses: Theory and experiment,” *Phys. Rev. Lett.* **100**, 103004 (2008).

- [32] J. Lim, K. Lee, and J. Ahn, “Ultrafast Rabi flopping in a three-level energy ladder,” *Opt. Lett.* **37**, 3378 (2012).
- [33] M. Reetz-Lamour, T. Amthor, J. Deiglmayr, and M. Weidemüller, “Rabi Oscillations and Excitation Trapping in the Coherent Excitation of a Mesoscopic Frozen Rydberg Gas,” *Phys. Rev. Lett.* **100**, 253001 (2008).
- [34] J. Lim, H. Lee, S. Lee, C. Y. Park, and J. Ahn, “Ultrafast Ramsey interferometry to implement cold atomic qubit gates,” *Sci. Rep.* **4**, 5867 (2014).
- [35] J. J. Sakurai, *Modern Quantum Mechanics*, (Addison-Wesley, New York, 1994).
- [36] G. W. F. Drake, *Handbook of Atomic, Molecular, and Optical Physics*, (Springer, New York, 2006).
- [37] J. S. Melinger, S. R. Gandhi, A. Hariharan, D. Goswami, and W. S. Warren, “Adiabatic population transfer with frequency-swept laser pulses,” *J. Chem. Phys.* **101**, 6439 (1994)
- [38] H. Lee, H. Kim, and J. Ahn, “Ultrafast laser-driven Rabi oscillations of a Gaussian atom ensemble,” *Opt. Lett.* **40**, 510 (2015).
- [39] S. Lee, H. Lee, J. Lim, J. Cho, C. Y. Park, and J. Ahn, “Coherent control of multiphoton-ionization passage of excited-state rubidium atoms,” *Physical Review A* **86**, 045402 (2012).
- [40] S. Patel, “A Chirped, Pulsed Laser system and Magneto Optical Trap for Rubidium,” Ph.D. Thesis, University of Southampton, Southampton, United Kingdom (2008).
- [41] C. J. Foot, *Atomic Physics*, (Oxford University Press, New York, 2005).
- [42] J. D. Jackson, *Classical Electrodynamics*, (Wiley, New York, 1999)
- [43] H. Lee, H. Kim, J. Lim, and Jaewook Ahn, “Quantum interference control of four-level diamond-configuration quantum system,” *Phys. Rev. A* **88**, 053427 (2013)
- [44] J. E. Sansonetti, “Wavelengths, Transition Probabilities, and Energy Levels for the Spectra of Rubidium (RbI through RbXXXVII),” *J. Phys. Chem. Ref. Data*, **35**, 301, (2006).
- [45] D. A. Steck, Rubidium 85 D Line Data, <http://steck.us/alkalidata>.
- [46] D. M Brink and G. R. Satchler, *Angular Momentum*, Oxford, 1962.
- [47] H. Kim, Y. Song, H. G. Lee, and J. Ahn, “Rabi oscillations of Morris-Shore transformed N-state systems by elliptically polarized ultrafast laser pulses,” *Phys. Rev. A* **91**, 053421 (2015).
- [48] M. H. Leviti and R. Freeman, “NMR population inversion using a composite pulse,” *J. Magn. Reson.* **33**, 473 (1979).
- [49] W. Rakreungdet, J. H. Lee, K. F. Lee, B. E. Mischuck, E. Montano, and P. S. Jessen, “Accurate microwave control and real-time diagnostics of neutral-atom qubits,” *Phys. Rev. A* **79**, 022316 (2009).
- [50] R. Trebino, K. W. DeLong, D. N. Fittinghoff, J. N. Sweetser, M. A. Krumbügel, B. A. Richman, and D. J. Kane, “Measuring ultrashort laser pulses in the time-frequency domain using frequency-resolved optical gating” *Rev. Sci. Instrum.* **68**, 3277 (1997).

- [51] G. L. Gattobigio, T. Pohl, G. Labeyrie, and R. Kaiser, “Scaling laws for large magneto-optical traps,” *Phys. Scr.* **81**, 025301 (2010).
- [52] G. S. Vasilev and N. V. Vitanov, “Complete population transfer by a zero-area pulse,” *Phys. Rev. A* **73**, 023416 (2006).
- [53] N. V. Vitanov, “Complete population inversion by a phase jump: an exactly soluble model,” *New J. Phys.* **9**, 58 (2007).
- [54] H. Lee, Y. Song, H. Kim, H. Jo, and J. Ahn, “Quantum dynamics of a two-state system induced by a chirped zero-area pulse,” *Phys. Rev. A* **93**, 023423 (2016).
- [55] N. V. Vitanov, L. P. Yatsenko, and K. Bergmann, “Population transfer by an amplitude-modulated pulse,” *Phys. Rev. A* **68**, 043401 (2003).
- [56] M. Wollenhaupt, T. Bayer, N. V. Vitanov, and T. Baumert, “Three-state selective population of dressed states via generalized spectral phase-step modulation,” *Phys. Rev. A* **81**, 053422 (2010).
- [57] A. M. Weiner, “Ultrafast optical pulse shaping: a tutorial review,” *Opt. Comm.* **284**, 3669 (2011).
- [58] J. Beugnon, C. Tuchendler, H. Marion, A. Gaëten, Y. Miroshnychnko, T. R. P. Sortais, A. M. Lance, M. P. A. Jones, G. Messin, A. Browaeys, and P. Grangier, “Two-dimensional transport and transfer of a single atomic qubit in optical tweezers,” *Nat. Phys.* **3**, 696 (2007).
- [59] R. Blatt and D. J. Wineland, “Entangled states of trapped atomic ion,” *Nature* **453**, 7198 (2008).
- [60] Y. Song, H. Lee, H. Jo, and J. Ahn, “Selective excitation in a three-state system using a hybrid adiabatic-nonadiabatic interaction,” *Phys. Rev. A* **94**, 023412 (2016).

## Acknowledgments in Korean

우선 긴 시간동안 저를 이끌어주시고 도와주신 안재욱 교수님께 깊이 감사드립니다. 교수님께 논문에 대한 지도 뿐만이 아닌 연구를 위한 사고방식이나 학술적인 문제를 바라보는 태도에 대해 많은 것들을 배울 수 있었습니다. 바쁘신 일정 중에 학위 논문을 심사해주시고 많은 조언과 지적을 해주셨던 심홍선 교수님, 유대혁 박사님, 이상민 교수님, 이진형 교수님, 그리고 조용훈 교수님께도 감사의 말씀드립니다.

매일 밤늦게까지 같이 열심히 공부하고, 실험하는 우리 연구실 식구들, 효섭이, 우준이, 한래, 윤홍이, 민혁이, 경태, 애덤, 그리고 사무 봐주시는 은정씨 모두에게 감사합니다. 연구 관련 일도 잡다한일도 여러모로 많은 도움을 받았습니다. 처음 연구실에 들어 왔을 때부터 스스로 연구 할 수 있게 될 때까지 도와준 경진이형, 영찬이형, 민우형, 준우형, 상경이형, 종석이형, 강희형, 그리고 대훈이형에게도 감사의 말을 전합니다. 특히 수많은 밤을 실험실에서 함께 지낸 종석이형에게 다시 한번 고마운 마음 전합니다. 같이 공부하면서 고생한 윤진이, 강희, 종해, 상우, 진섭이, 만날 때마다 즐거웠던 민호, 순호, 위석이 그리고 연락하면 언제나 반겨주던 경민이에게도 고마움 전합니다.

마지막으로 항상 저를 믿어주시고 사랑을 주시는 부모님과 동생에게 깊은 감사의 마음을 전합니다.



## Curriculum Vitae in Korean

이 름: 이 한 결

생 년 월 일: 1985년 8월 27일

전 자 주 소: hgyeol@kaist.ac.kr

### 학 력

2001. 3. – 2003. 2. 인천과학고등학교 (2년 수료)  
2003. 3. – 2009. 2. 한국과학기술원 물리학과 (B.S.)  
2009. 2. – 현재 한국과학기술원 물리학과 석박사 통합과정

### 경 력

2011. 3. – 2011. 6. 한국과학기술원 물리학과 물리학실험III 조교  
2012. 3. – 2012. 6. 한국과학기술원 물리학과 물리학실험III 조교  
2012. 3. – 2012. 12. 한국과학기술원 물리학과 응용물리학실험 조교  
2013. 9. – 2013. 12. 한국과학기술원 물리학과 응용물리학실험 조교  
2014. 3. – 2014. 6. 한국과학기술원 물리학과 고급물리학I 조교

### 연구 업 적

1. Hyosub Kim, Woojun Lee, **Han-gyeol Lee**, Hanlae Jo, Yunheung Song, and Jaewook Ahn, “In situ single-atom array synthesis by dynamic holographic optical tweezers,” *Nature Communications* **7**, 13317 (2016).
2. Yunheung Song, **Han-gyeol Lee**, Hanlae Jo, and Jaewook Ahn, “Selective excitation in a three-state system using a hybrid adiabatic-nonadiabatic interaction,” *Physical Review A* **94**, 023412 (2016).
3. **Han-gyeol Lee**, Yunheung Song, Hyosub Kim, Hanlae Jo, and Jaewook Ahn, “Quantum dynamics of a two-state system induced by a chirped zero-area pulse,” *Physical Review A* **93**, 023423 (2016).
4. Hyosub Kim, Yunheung Song, **Han-gyeol Lee**, and Jaewook Ahn, “Rabi oscillations of Morris-Shore transformed N-state systems by elliptically polarized ultrafast laser pulses,” *Physical Review A* **91**, 053421 (2015).
5. Hyosub Kim, Woojun Lee, **Han-gyeol Lee**, and Jaewook Ahn, “Nonparaxial aberrations in the optical Talbot effect probed by quantum-dot fluorescence tomography,” *Physical Review A* **91**, 033817 (2015).

6. **Han-gyeol Lee**, Hyosub Kim, and Jaewook Ahn, “Ultrafast laser-driven Rabi oscillations of a Gaussian atom ensemble,” *Optics Letters* **40**, 510 (2015).
7. Jongseok Lim, **Han-gyeol Lee**, Sangkyung Lee, Chang Yong Park, and Jaewook Ahn, “Ultrafast Ramsey interferometry to implement cold atomic qubit gates,” *Scientific Reports* **4**, 5867 (2014).
8. **Han-gyeol Lee**, Hyosub Kim, Jongseok Lim, and Jaewook Ahn, “Quantum interference control of four-level diamond-configuration quantum system,” *Physical Review A* **88**, 053427 (2013).
9. Jongseok Lim, **Han-gyeol Lee**, and Jaewook Ahn, “Review of cold Rydberg atoms and their applications,” *Journal of Korean Physical Society* **63**, 867 (2013).
10. Kyunghnam Kim, **Han-gyeol Lee**, Jaewook Ahn, and Sohee Jeong, “Highly luminescing InP multishell semiconductor nanocrystals InP/ZnSe/ZnS,” *Applied Physics Letters* **101**, 073107 (2012).
11. Junwoo Cho, **Han-gyeol Lee**, Sangkyung Lee, Jaewook Ahn, Won-Kyu Lee, Dai-Hyuk Yu, Sun Kyung Lee, and Changyong Park, “Optical repumping of triplet P-states enhances magneto-optical trapping of ytterbium atoms,” *Physical Review A* **85**, 035451 (2012).
12. Jongseok Lim, **Han-gyeol Lee**, Sangkyung Lee, and Jaewook Ahn, “Quantum control in two-dimensional Fourier transform spectroscopy,” *Physical Review A* **84**, 013425 (2011).
13. Jongseok Lim, **Han-gyeol Lee**, Jae-uk Kim, Sangkyung Lee, and Jaewook Ahn, “Coherent transients mimicked by two-photon coherent control of three-level system,” *Physical Review A* **83**, 053429 (2011).
14. Kyeong-Jin Jang, **Han-gyeol Lee**, Sangkyung Lee, Jaewook Ahn, Jai Seok Ahn, Namjung Hur, and Sang-Wook Cheong, “Strong spin-lattice coupling in multiferroic hexagonal manganite YMnO<sub>3</sub> probed by ultrafast optical spectroscopy,” *Applied Physics Letters* **97**, 031914 (2010).